Title
Scale dependent spatial structuring of mountain river large bed elements maximizes flow resistance

Authors
Wiener, JS
Pasternack, GB

Publication Date
2022-11-01

DOI
10.1016/j.geomorph.2022.108431

Scale dependent spatial structuring of mountain river large bed elements maximizes flow resistance

J. S. Wiener (ORCHID: 0000-0002-1667-8225) and G. B. Pasternack (ORCHID: 0000-0002-1977-4175)

University of California, Davis, One Shields Avenue, Davis, CA 95616, USA.

Corresponding author: Jason Wiener (jswiener@ucdavis.edu)

Cite as: Wiener, J.S., Pasternack, G.B. 2021. Scale dependent spatial structuring of mountain river large bed elements maximizes flow resistance. Geomorphology. DOI: https://doi.org/10.1016/j.geomorph.2022.108431

This version of the article includes edits made during the galley proof stage,so it should have identical content as the publisher's version.

Abstract

Macro-roughness elements such as boulders and bedrock outcrops, collectively referred to as large bed elements (LBEs), are key features influencing hydrodynamics and morphodynamics in mountain rivers. Where LBEs are abundant and account for a substantial portion of total flow resistance, existing geomorphic theory, previous physical experiments, and limited field observations support the theory that LBE configurations adjust to maximize flow resistance. However, methods to explicitly map individual features along entire river segments are lacking, thus limiting analysis of LBE spatial structure in boulder-bedded rivers. In addressing these gaps, this study sought to develop a procedure for mapping LBEs from 3D point-clouds, explore LBE spatial structure in a real boulder-bedded river, and test the hypothesis that LBE configurations were organized to maximize flow resistance. The mapping procedure applied a ground classification algorithm to produce a roughness surface model, from which LBEs were extracted by a marker controlled watershed algorithm. Implementing the procedure, 42,176 LBEs were mapped in 13.2-km of the mountainous Yuba River (Northern California). Scale and discharge-dependent LBE concentration and spacing metrics were quantified for multiple laterally and/or hierarchically nested spatial domains and classified to differentiate three flow-resistance based hydrodynamic regimes: isolated roughness, wake interference, and skimming flow. Of these regimes, wake interference corresponds to a state of maximum resistance, so hypothesis testing involved determining if this regime was dominant. Results confirmed 25 of 28 segment- and reach-scale LBE concentrations were in the wake interference regime. However, spacing metrics classified 24 of these same spatial domains in the skimming flow regime. Concentration metrics, which quantify LBE density in a given spatial area, differ from spacing metrics, which represent LBE proximity to one another. While comparison of segment and reach-scale regime classifications by each metric concluded concentration was superior to spacing for regime classification purposes, these disparities leave open questions about this extremal model of geomorphic adjustment. Lastly, lateral variability of metrics across the river corridor had implications for discharge-dependent resistance.

Keywords:
Macroroughness, flow resistance, mountain rivers, lidar, boulders

Main text:

1. Introduction

Macroroughness riverbed elements such as boulders and bedrock outcrops differentiate mountain rivers from most lowland gravel-or-sand bedded rivers (Bathurst, 1978; Grant et al., 1990). Collectively referred to herein as large bed elements (LBEs), these features have a primary influence on hydraulic, hydrodynamic, and morphodynamic properties of mountain river channels as well as secondary effects on adjacent landscape processes (Table S1). In laterally confined coarse-bedded rivers where adjustment of channel planform and gradient are more restricted, extremal hypothesis, regime theory, physical experiments, and field observations support the theory that channels adjust bed roughness to maximize flow resistance, as this corresponds to a state of maximum stability (Davies and Sutherland, 1983; Abrahams et al., 1995; Church et al., 1998; Wohl and Merritt, 2008; Eaton and Church, 2009; Adams, 2020; Eaton et al., 2020).

Where LBEs are abundant, such as in bedrock or boulder-bedded rivers, the latter defined as those with $D_{50} \geq 64$ mm (Bathurst, 1982), LBEs account for a substantial portion of total flow resistance (Chen et al., 2019). Links between LBE spatial structure metrics, such as LBE concentration and spacing, and flow resistance mean that such metrics can serve as a proxy for bed roughness adjustment and address whether LBEs are configured to maximize flow resistance (Bathurst, 1978; Ferro, 1999; Canovaro et al., 2007; Papanicolaou and Tsakiris, 2017). However, study of this phenomenon, and the spatial structure of LBEs in natural river segments with abundant LBEs are still largely absent (Williams et al., 2019; Adams, 2020). This absence arises in part due to variability in how LBEs are defined and limited availability of continuous and comprehensive segment-scale LBE datasets (Benda, 1990; Grant and Swanson, 1995; Shobe et al., 2016).

Existing definitions of LBEs or macroroughness elements vary considerably in the peer-reviewed literature (Table S2), but typically reference fixed lengths or scaled measures of grain diameter including but not limited to D > 0.5 m, D ≈ bankfull flow depth, and D_{90} (D is grain size diameter and the subscript is the percent of grains finer). While arguably of equal import to the processes describe in the paragraph above (Gippel et al., 1996), the inclusion of large woody materials (LWM) in LBE definitions has been variable or unclear (Table S2). Inconsistent definitions complicate LBE mapping, and the interpretation and comparison of LBE related study findings between rivers. Alternate metrics, such as surface roughness that can account for LWM, coupled with algorithmic mapping procedures offer opportunity to provide more consistent, transferable LBE mapping approaches across rivers. However, automated methods to map these features in natural environments from remotely sensed data products remain limited (Carbonneau et al., 2004; Resop et al., 2012).

To address these gaps, we developed a semi-automated procedure for mapping LBEs from three-dimensional (3D) point clouds obtained via an airborne laser system. We then used results to explore the spatial structure of LBEs in a real boulder-bedded mountain river and address three specific scientific questions including whether LBEs were configured to maximize flow resistance. In the following sections, we first present background on LBE mapping (1.1), discuss factors influencing LBE spatial structure (1.2), review hydrodynamic influences of LBEs (1.3), and finally present the questions of this study (1.4). Through objectively and systematically mapping LBEs, this study generated a large LBE dataset to test hypotheses providing insight into the spatial structure of LBEs in a real mountain river at multiple scales.

1.1. Mapping LBEs in river corridors

In-situ LBE mapping has been done manually with global positioning system (GPS) or total station survey equipment (Vallé and Pasternack, 2006). Unfortunately, it may not be possible to map LBEs at all where access is limited or dangerous, which is a common situation in mountain rivers. Further, mapping all LBEs would be time consuming if hundreds-to-thousands of LBEs exist within a survey area, which may be the case at reach (~10^2-10^3 channel widths) and segment scales (~10^3-10^4 widths). Field survey methods for LBEs are also subject to the same problem of surveyor bias that occurs with mapping morphological units.

Remote sensing techniques for studying river sedimentology have a history spanning over four decades (Piégay et al., 2020). Broadly, we divide remote sensing approaches into those based on imagery and those based on topographic data. Many image-based techniques have proven capable of predicting grain-size information from images (e.g., Butler et al., 2001; Warrick et al., 2009; Purinton and Bookhagen, 2019). However, methods often focus on predicting representative grain size metrics (D_{50} or D_{84}), and do not facilitate mapping individual grains like LBEs. Software, such as Detert and Weitbrecht's (2012) '*BaseGrain*' and Purinton and Bookhagen's (2019) '*PebbleCounts*', that include this capability have limited testing in mountain rivers with heterogeneous surface roughness's that complicate grain mapping (Pearson et al., 2017), and appear difficult to apply beyond the reach scale due to computational and input data requirements. Alternately, LBEs are commonly manually digitized from aerial images (Chen et al., 2019; Finnegan et al., 2019). All image-based methods have limited ability to map submerged LBEs, require high-resolution imagery (<<1 m pixels) to ensure mapping accuracy (Carbonneau et al., 2004), and do not explicitly measure particle heights (i.e. planimetric two-dimensional [2D] mapping only).

Remote sensing of river topography likewise offers opportunities for studying river sedimentology and potential to overcome the 2D limitations of image-based methods (Hodge et al., 2009; Brasington et al., 2012). Generically, these approaches involve developing statistical models between measured sedimentological characteristics and topographic metrics, such as roughness height (Gomez, 1993) or the standard deviation, semi-variance, skewness, or kurtosis of detrended bed elevations within a submeter convolution kernel (Aberle and Smart, 2003; Schneider et al., 2015). Common topographic data sources include airborne or terrestrial laser systems (ALS and TLS, respectively) or photogrammetric techniques such as structure-from-motion (SfM). Factors relevant to LBE mapping such as resolution (point density), spatial coverage, accuracy, post-processing requirements, and cost vary widely between methods (Tomsett and Leyland, 2019). For example, while TLS and SfM produce greater point densities than ALS, (~10,000 pts/m^2 compared to ~10's pts/m^2 [Brasington et al., 2012]), they have greater time and labor requirement and may not be feasible in inaccessible mountain regions or for segment-scale applications (Tomsett and Leyland, 2019; Piégay et al., 2020). A caveat of nearly all image- and topographic-based grain-size prediction approaches is reliance on statistical models calibrated with site-specific field measurements. When models are applied outside the systems in which they're developed it is common for predictions to perform poorly on novel data (Pearson et al., 2017).

To our knowledge, Resop et al. (2012) provide the best example of semi-automated mapping of LBEs in a natural setting. Using TLS, they applied a series of image-processing algorithms to a 2-cm digital terrain model (DTM) to segment and map individual boulders (>256 mm) along 100 m of a boulder-bedded river. Their approach, derived from methods for mapping tree canopies, performed well at mapping the location and shape of boulders compared to field measurements. A multi-step un-validated GIS approach to map boulders in the mountainous South Yuba River from a combination of terrestrial ALS, bathymetric sonar, and GPS survey data is also presented by Pasternack and Senter (2011). Overall, remote sensing offers potential for new and continued research in river sedimentology including mapping LBEs.

1.2. Organization of LBEs in river corridors

In natural channels, LBE spatial structure, defined as the number, size, and arrangement of LBEs, evolves as landscapes are acted upon by hillslope, glacial, volcanic, tectonic, fluvial, and biogeomorphic forces that together produce three key processes: supplying LBEs to the channel or exhuming them; weathering and attrition of LBEs; and LBE transport, deposition, and storage (Table S1). Hillslopes and low-order tributaries (1^{st}-3^{rd} order) are the main source delivering new LBEs to the channel network through landslide related processes (Benda, 1990; Hungr et al., 2001; Hewitt, 2002). Once in the river corridor, LBEs can remain immobile or only intermittently mobile for periods lasting 10^2-10^6 years (e.g. Williams et al., 2019). On the other hand, observations support that LBEs up-to several meters in size may still be transported downstream more frequently (<10^2 year recurrence intervals) (Grant et al., 1990; Molnar et al., 2010). In-channel LBEs also provide feedback on landscape evolution due to their ability to mediate incision, shape channel morphology, and influence sediment storage and transport (Hassan and Reid, 1990; Madej, 2001; Shobe et al., 2016; Golly et al., 2019). In-turn, these feedbacks, and associated changes to LBE spatial structure and channel boundaries, modify flow resistance. Applying the simplifying assumption that channel adjustments are such that when resistance is low relative to hydraulic forces the channel boundary will adjust to increase hydraulic resistance and visa-versa, these feedbacks enable trajectories of LBE mediated channel adjustment toward conditions of maximum resistance while leaving room for more complex oscillations and non-equilibrium behavior (Chin and Phillips, 2007; Wohl and Merritt, 2008; Eaton and Church, 2009; Ferguson et al., 2019).

1.3. LBE influence on hydraulics and hydrodynamics

Protrusion of LBEs into a flow-field exert resistance on the fluid via frictional shear (Bathurst, 1978) and pressure fluctuations (Einstein and Barbarossa, 1952), colloquially termed skin friction and form drag, respectively. In boulder-bedded rivers, form resistance from LBEs can account for a substantial portion (>90 %) of total flow resistance (Chen et al., 2019). When an array of LBEs is present, as is the case in natural channels, the superpositioning of vortices further affects resistance, wake and turbulent flow structures, and flow-field recovery (Canovaro et al., 2007; Fang et al., 2017).

Morris (1959) classified these combined effects into three basic hydrodynamic regimes: isolated roughness, wake interference, and skimming flow. Isolated roughness occurs when macroroughness feature spacing is large enough that wakes do not interact and the flow recovers before engaging the next downstream feature. Wake interference occurs when the wake from one feature extends to the next downstream feature and the flow never recovers. Lastly, skimming flows occur when features are close enough to form pockets of trapped highly irregular flow patterns with a relatively smooth flow structure above.

Morris's hydrodynamic regimes may be interpreted in terms of flow resistance (Fang et al., 2017; Papanicolaou and Tsakiris, 2017). When LBEs are widely spaced, such as in the isolated regime, total form resistance due to LBEs can be estimated as the sum of drag on individual LBEs (Gippel et al., 1996). As more LBEs occupy the flow-field, the resistance relationship becomes non-linear typically reaching a peak in resistance followed by a decrease that eventually plateaus regardless of the presence of additional LBEs. The initial transition from linear to non-linear behavior is hypothesized to indicate a regime shift from isolated roughness to wake interference, wherein resistance reaches its peak. The subsequent decrease in resistance and plateau region are associated with conditions of skimming flow where resistance is proportionally high but not at a maximum (Ferro, 1999; Canovaro et al., 2007). Thus, the wake interference regime has been assumed to broadly correspond with conditions of maximum flow resistance.

Morris's hydrodynamic regimes have served as a basis in many physical experiments describing how LBEs influence the flow-field and flow resistance (e.g., Ferro, 1999; Canovaro et al., 2007; Papanicolaou and Tsakiris, 2017). In these studies, Morris's regimes have been represented using LBE concentration (Γ), which varies in how it is calculated but is defined here as the ratio of planform LBE area to wetted channel area; and/or non-dimensional spacing (λ_*), typically calculated as the distance (λ) between LBEs divided by the diameter of the upstream LBE (D_c). Strong correspondence in the above referenced studies between these LBE spatial structure metrics and flow resistance measurements allows a direct link connecting metrics with Morris's regimes and conditions associated with maximum resistance. Conceptually, provided availability of a census of LBEs, these same LBE spatial structure metrics may be extended to classify Morris's regimes in natural settings and test the degree that conditions associated with maximum resistance are present at multiple spatial scales.

1.4. Scientific questions

The sections above highlight three scientific questions concerning the mapping and spatial structure of LBEs in natural channels. First, can ALS data be used to accurately map sub-meter resolution LBEs along entire river segments? Second, are LBEs configured to maximize flow resistance, and if so at what typical spatial scales (segment, reach, and cross-section) does this occur? Third, does LBE spatial structure vary laterally to provide differential discharge-dependent roughness?

2. Study river segment

The field site was a confined 13.2-km segment of the mountainous Yuba River (Northern California) draining 1853 km^2 of the western Sierra Nevada range (Figure 1). It is comprised of a low sinuosity, boulder-bedded, 5th order mountain river confined within a steep-walled bedrock and forested hillside canyon, which is common among rivers draining the western slope of the northern Sierra Nevada range (Guillon et al., 2020). The river has a mean bed slope of 1.96 % but exhibits localized variability, with many 10–100 m long (10^0–10^1 widths) stretches having slopes exceeding 10 %. Like many bedrock-confined rivers, the study site lacks a contiguous floodplain having only localized areas supporting accumulation of alluvium at major tributary junctions, meander bends, or other areas of local valley widening (Fryirs et al., 2016). Despite this ambiguity, a previously reported morphologically determined bankfull discharge (Q_{bf}) of 10.7 m^3/s (YCWA, 2013) was used to enable comparison of metrics across sites respective of scale. For analytical purposes, the study site was delineated into six geomorphic reaches on the sole basis of channel-bed slope breaks (Figure 2).

Based on limited sedimentological data, bed substrates alternate between bedrock and alluvial sections (YCWA, 2013). Alluvial substrate, where present, is a heterogeneous mixture of materials dominated by coarse fractions (medium gravel/cobbles and larger). Contemporary sources of coarse clastic materials result from hillslope process, exhumation of boulders or bedrock, historic hydraulic mining activities, and in-channel stores. Uniformly steep hillslopes are present along the study site with large areas exceeding 0.8 m/m, a regional slope threshold identified by Hurst et al. (2012) for producing landslides and scree cones. Curtis et al. (2005) also found mass wasting processes to dominate over other erosional processes (e.g. surface erosion), thus providing a relatively abundant supply of LBEs for delivery to the valley-bottom. Review of aerial imagery (Google Earth®) from 1957 to present shows landslides, debris flows, and rock falls throughout the study site. Quaternary glaciation present in the easternmost portions of the Yuba basin did not extend to the study site, however it is plausible that outwash deposits remain.

The region's alluvial-sediment processes are also affected by anthropogenic influences. New Bullards Bar (NBB) Dam is a 196.6 m high concrete arch dam on the North Yuba River near Dobbins, CA. Closed in 1969, the dam is a complete barrier to bedload transport into the study site passing only wash load. Two additional dams, Log Cabin Dam and Our House Dam, situated upstream of the study site in the Middle Yuba watershed, also act as partial barriers to downstream sediment transport.

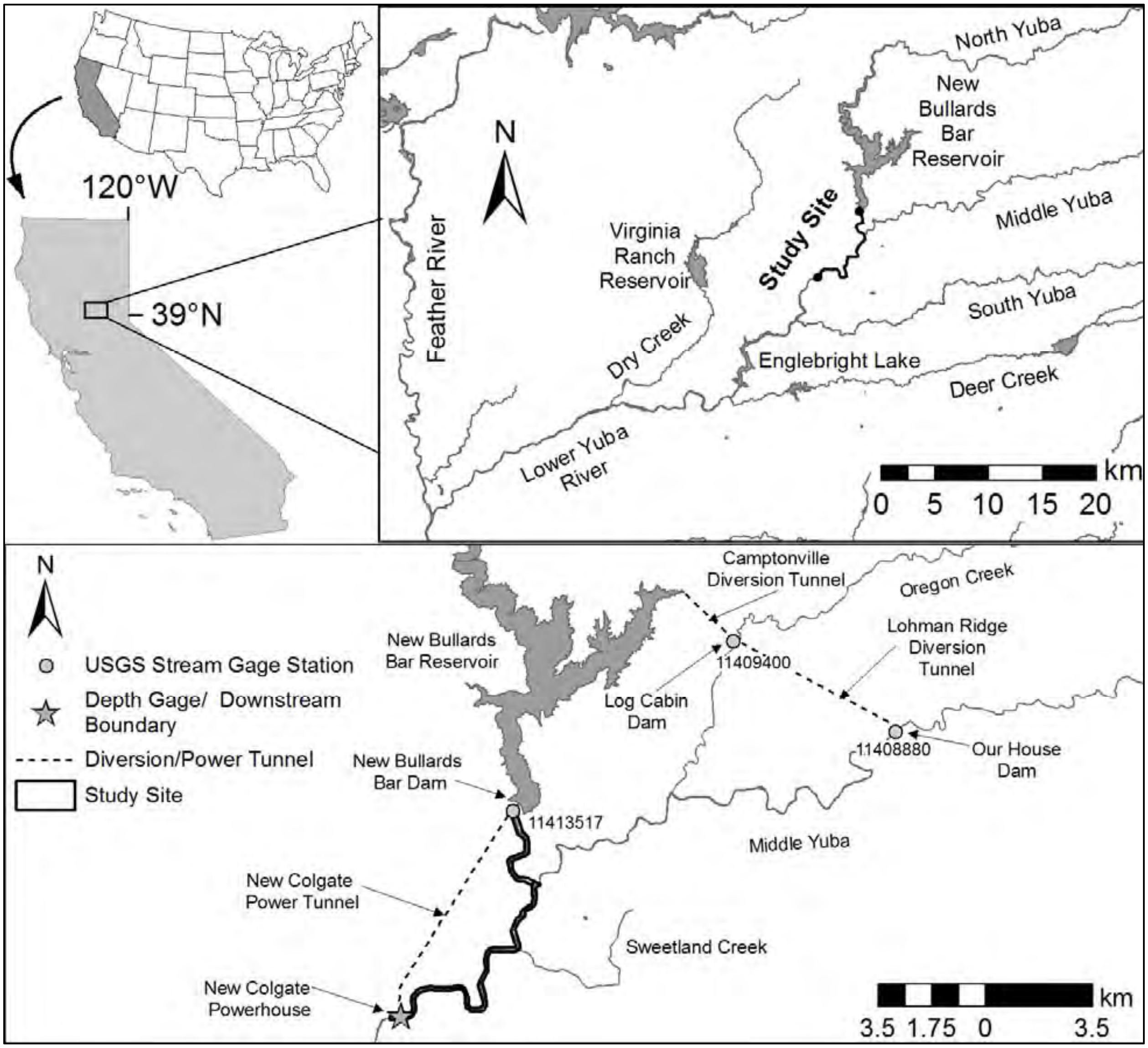

Figure 1. Map of study site, tributaries, gages, and infrastructure facilities, Yuba River, CA.

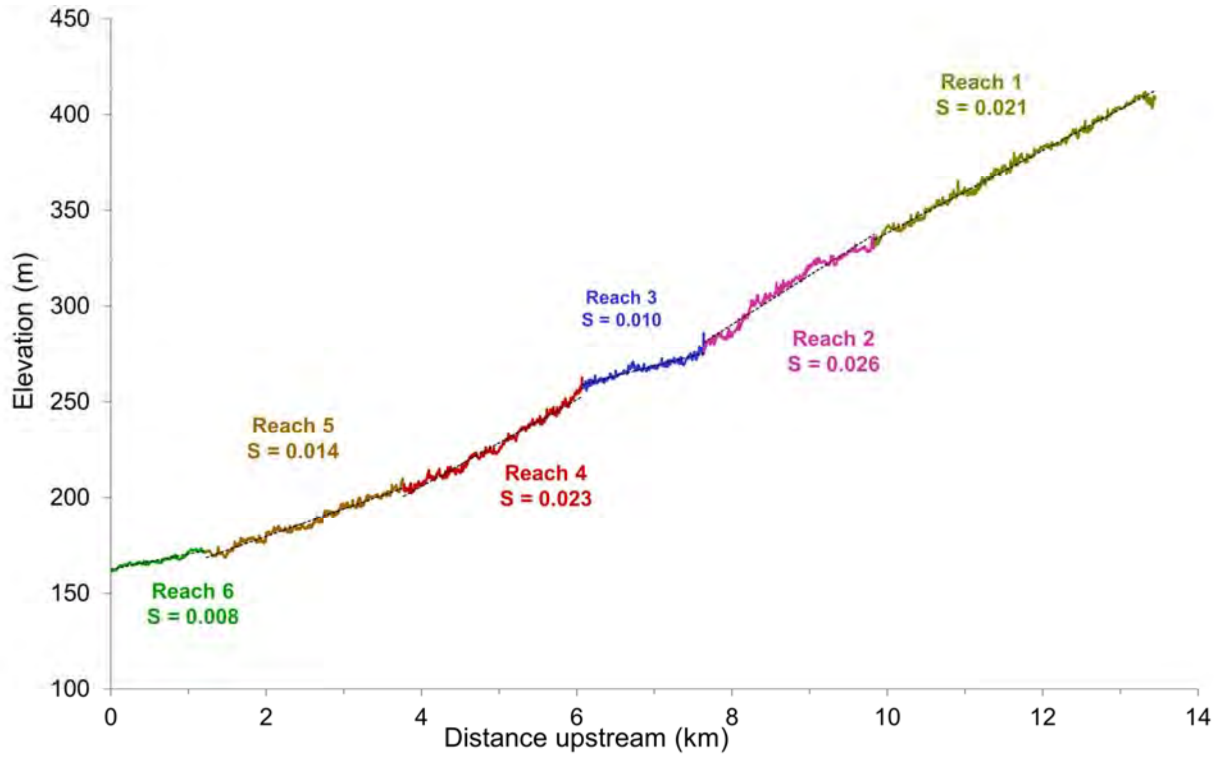

Figure 2. Longitudinal profile showing the extent and slope (m/m) of geomorphic reaches.

3. Methods

The three scientific questions were answered in order, as they build on each other. To address the first study question, a field campaign and remote sensing survey were carried out to collect topo-bathymetric point clouds and locate real LBEs in the study river segment (sections 3.1-3.2). A procedure for mapping LBEs along river channels from ALS 3D point-cloud data was developed, tested, and applied to map LBEs in a real boulder-bedded mountain river (section 3.3). Question 1 was answered using performance metrics comparing predicted LBEs to observed LBEs, using two different analyses (section 3.3). Next, to address the second question, LBE data were coupled with results from a 2D hydrodynamic model (section 3.4) to define LBE spatial structure metrics within multiple discharge-dependent portions of the river corridor (section 3.5). Specifically, Γ and λ_* values were calculated at segment, reach, and cross-sectional

(0.1 width) scales. These were then compared to thresholds associated with Morris's wake interference regime from the literature to test the hypothesis that LBEs were organized to maximize flow resistance at these three spatial scales, as indicated by LBE spatial structure metrics corresponding with the wake interference regime. Finally, the third question regarding lateral distribution of LBE structure and flow resistance was answered by quantifying differences in LBE spatial structure metrics for different incremental inundation corridors, as defined in section 3.5.1.

3.1. Topo-bathymetric mapping

Between September 27-29, 2014 ALS data were collected within the study site by a professional surveying firm (Quantum Spatial, https://www.quantumspatial.com/) using a Riegl VQ-820-G bathymetric sensor system and a Leica ALS50 Phase II system (near infrared) mounted in a Cessna Grand Caravan. The initial ground classified point density was 2.3 pts/m^2. Following a process to address misclassification errors, this density was increased to 13.9 pts/m^2 (Supplementary Text S3.1). ALS collection was conducted during a period of low discharge estimated at 1.19 m^3/s at the downstream study site boundary. This discharge is exceeded 89.4 % of the time based on the period October 1968–February 2016 (Wiener and Pasternack, 2016a).

ALS data were supplemented with boat-based bathymetric observations, imagery-derived bathymetric estimates (e.g. Legleiter et al., 2004), and systematically placed augmented points (Vallé and Pasternack, 2006). Single beam echo sounding data was collected by kayak between July 8 and 9^{th} 2015 during low-flow conditions (0.89 m^3/s) using an Ohmex Sonarmite. The boat's 3D position was tracked using a Trimble 5800 Real Time Kinematic (RTK) GPS tied to a local base station. Average boat-based point density was 0.53 pts/m^2.

Through verification and merging of individual datasets, an extremely detailed and accurate topographic map was created (Text S3.1; Wiener and Pasternack, 2016b). The final bare earth mapping included >21 million points at an average point-spacing of 0.25 m (~16 pts/m^2). Points were used to create a 0.46 m x 0.46 m resolution raster (bare earth DTM), the final map product used in the study.

3.2. Observed LBE dataset

For the purpose of parameterizing and assessing the study's LBE mapping approach an observed LBE dataset consisting of independently mapped LBEs was generated within a portion of the study segment from high-resolution aerial imagery. Imagery was collected for the downstream 1.2 km of the study site on September 20, 2016 using a DJI Phantom 3 Professional quadcopter uncrewed aerial vehicle equipped with on-board GPS, camera, and camera gimbal. The discharge on this day was estimated at 1.02 m^3/s (a low flow) at the downstream boundary. Images were processed and a 2.6 cm resolution composite orthomosaic photograph was generated using Agisoft Photoscan Professional version 1.3 (Photoscan) following methods described by Carey et al. (2019). No terrain products were produced from the captured images.

The composite orthomosaic photograph, which contained numerous visible LBEs, was georeferenced to align with the study's ALS data. Next, LBEs visible in the orthomosaic photograph were manually digitized. Selecting which LBEs to digitize was done by randomly panning to different portions of the orthomosaic and digitizing all LBE that were clearly visible and differentiable from the bare earth and water. Digitizing was capped at a single 8-hour day effort. A total of 1194 digitized LBEs overlapping the region of topographic data collection (section 3.1) served as the LBE dataset (LBE_o) (Figure 3).

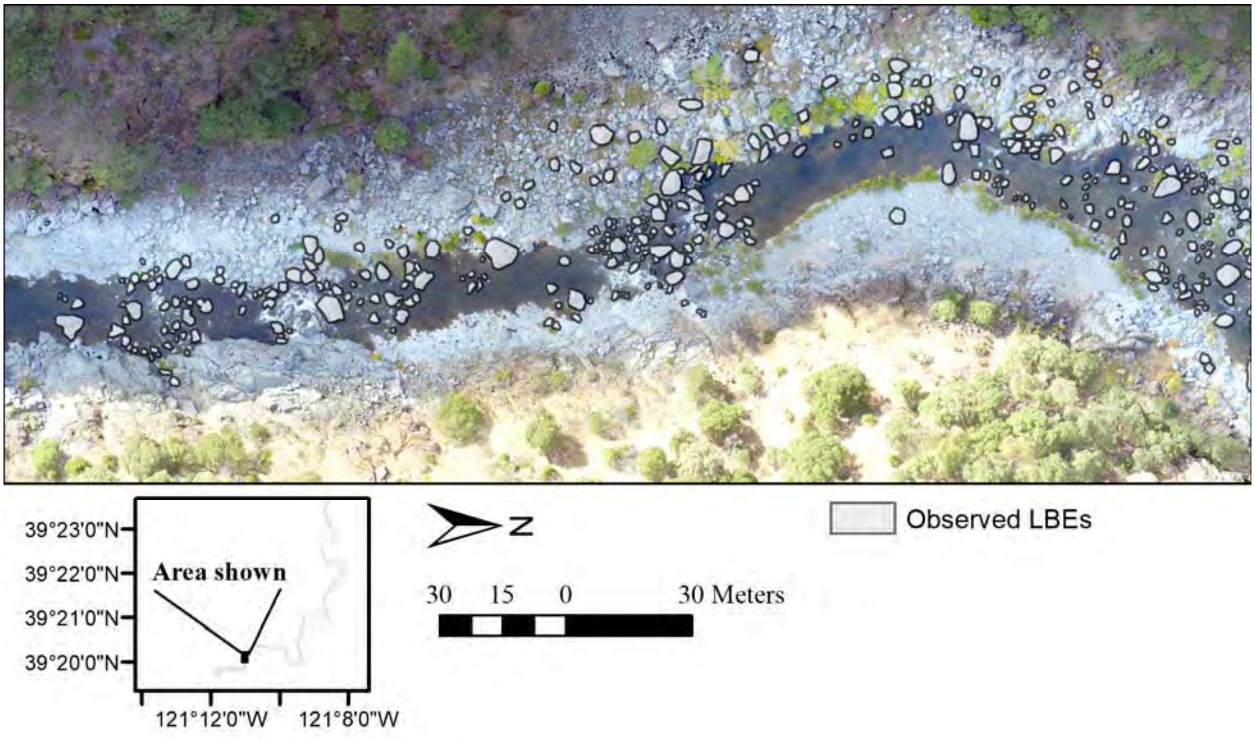

Figure 3. Portion of orthomosaic with manually digitized large bed elements (LBE$_o$) outlined by black lines. Only a portion of visible LBEs were digitized.

3.3. LBE mapping

For this study, we do not propose a universal definition for LBEs. Instead we developed and applied a novel procedure (Figure 4) for mapping terrain features, in this case sub-meter scale LBEs, from 3D topographic point clouds. The procedure takes into consideration existing LBE definitions, site-specific sedimentology, and establishing consistent methods for parameter specification to aid transferability of the mapping procedure. The procedure comprised two main steps, generating a roughness surface model (RSM) and extracting LBEs from the RSM. To answer the first scientific question the accuracy of both steps required independent and step-wise assessment. Therefore, multiple RSMs were generated, and then multiple approaches were used to extract LBEs from the best performing RSM. In each step, test metrics were used to compare RSM and extraction results and LBE observations and identify the best outcomes. The best performing outcomes were vetted against benchmark values reported by Kaartinen et al. (2012) and Marconi et al. (2019) to determine if they met scientific norms to be considered accurate representations.

3.3.1 Roughness surface model generation and testing question 1

A RSM is the vertical difference between 'complete' and 'smoothed' DTMs. The RSM concept is similar to that of a canopy height model, a common product for mapping tree-crowns (Popescu and Wynne, 2004; Chen et al., 2006). Here, the complete DTM is the bare earth DTM described in section 3.1 and the smoothed DTM is essentially the bare earth DTM stripped of large roughness features, which methodologically differs from detrending the bare earth DTM. When these surfaces are differenced, the intent is for LBEs to 'stick-out' of the resulting RSM, as this allows them to be extracted in the second step of the mapping procedure.

Absent a unanimously accepted method for creating smoothed DTMs, a series of smoothed DTM point clouds and associated rasters were generated using the open source 'lasground_new.exe' ground classification algorithm (Isenburg, 2016), which applies an adaptive TIN approach to iteratively classify ground points from an unclassified point cloud based on six user defined parameters. This approach was selected as it proven to be effective at correctly classifying ground points in areas of variable terrain (Zhang and Whitman, 2005), is parametrically flexible, and its parameters (Table 1; Text S3.3) can be related to measurements meaningful to mapping terrain features. The algorithm was run using the bare earth 3D point cloud and a range of parameter values informed by physically based metrics (Table 1), such as site specific representative grain sizes, as inputs, to produce 14 unique smoothed DTM rasters (Table S3). Smoothed DTM rasters were then assessed heuristically based on visual observations of: (i) removal of clearly discernable LBEs; and (ii) retaining topographic characteristics of the original ground surface such as slope breaks, small-scale terrain undulations, and meso-scale terrain features. Based on this qualitative assessment, six smoothed DTMs were selected for further processing and evaluation (Table S3).

The first of these processing steps involved subtracting each smoothed DTM raster from the complete DTM raster to produce six unique RSM rasters. Next, a binary threshold approach was used to map discrete sets of preliminary LBEs from each RSM. This was done by assigning a random selection of 70 % of the LBE_o data to a 'training' dataset and then calculating the average RSM value of all raster cells located along the exterior boundary of each LBE_o polygon in the training set for each RSM, independently. Threshold values above which a RSM pixel was considered LBE were determined by taking the average of these sets of values for each RSM, respectively (Text S3.3).

Sets of preliminary LBEs were evaluated by comparing predicted LBE polygons with the remaining 30 % of the LBE_o data ('test data') using four performance metrics: producers accuracy (PA), producers overlap (PO), a modified Jaccard similarity index (MJI) and missed-to-excess ratio (MER). The four metrics were chosen to balance sensitivity to omission (i.e. missing a real LBE) and commission (i.e. mapping an erroneous LBE) errors, whereby PA and PO were considered to penalize omission and be less sensitive to commission compared to MJI and MER, which penalize commission while allowing omission (Shao et al., 2019). Jaccard index (JI) and PA are common metrics in classification exercises whereas PO and MER were devised for this study. PA, PO, and MJI all range from 0 to 1 and MER ranges from 0 to ∞. Higher values of all metrics indicate better mapping accuracy but not necessary better precision. Metrics were also formulated to control for the situation where an LBE was predicted but missed in the observed dataset. Details, including numerical formulations, are provided in the supplementary materials file (Text S3.3).

Metrics were calculated for each preliminary LBE dataset and then independently rescaled from 0 to 1 using standard normalization techniques. The arithmetic mean of normalized values was used as a global performance metric to select the best ground classification algorithm parameter set and associated RSM (‘preferred RSM’). Once identified, performance metrics of the preferred RSM were evaluated to determine if it could support accurate LBE extraction.

3.3.2 LBE extraction and accuracy testing for question 1

The procedure’s second step involved extracting LBEs from the preferred RSM and testing the accuracy of the extraction, as the second and more important test to answer question 1. The threshold technique described in section 3.3.1 offered one option for LBE extraction. However, while this simple and efficient method was considered reasonable for evaluating ground classification algorithm parameters to select the preferred RSM, both preliminary LBE mapping assessment and extensive research on tree-canopy mapping indicated alternative LBE extraction methods could improve mapping accuracy (Kaartinen et al., 2012). Drawing from forestry research, five LBE extraction approaches were identified for testing: (i) RSM with vertical threshold; (ii) Gaussian filtered RSM with vertical threshold; (iii) RSM with marker-controlled watershed segmentation (MCWS) algorithm and constant window size; (iv) RSM with MCWS and variable window size; and (v) Gaussian filtered RSM with MCWS and constant window size. Comparing tree-crown mapping algorithms, Kaartinen et al. (2012) demonstrated that MCWS performed equally well or outperformed more computationally expensive and parametrically complex approaches not tested in this study.

Approaches differed in regard to computational expense, number of parameters, and implementation. To evaluate mapping performance, multiple parameter sets were tested for each approach. Each parameter set was used to generate a set of predicted LBEs for the area covering the LBE_o dataset. Parameter values for each approach were either data-driven (i.e., derived from the LBE_o data) or selected from a range of reasonable physically meaningful values (i.e., LBE heights). To constrain parameter spaces only data-driven calculations were used for approaches (ii-v). Ultimately, 12, 6, 10, 2, and 14 parameter sets were specified for approaches (i-v), respectively, resulting in a total of 44 LBE datasets (LBE_p), each a distinct mapping of LBEs (Table S4). Details of each approach and rationale for parameter selection are provided in the supplementary materials file (Text S3.3).

Once mapped, LBE_p datasets were assessed for accuracy using the same performance metrics as in step one, but compared to the entire LBE_o dataset. In addition to this internal comparison, PA and MJI scores were also evaluated against benchmark values from forestry research. Kaartinen et al. (2012) report PA values from past studies between 0.40 and 0.93 and found matching rates, a metric similar to PA, between 0.28and 0.66 (median of 0.56) when benchmarking 32 tree-extraction algorithms. For MJI, JI scores from Marconi et al. (2019) were used for comparison. Their values ranged between 0.056 and 0.340 (median of 0.167).

The suite of performance metrics and summary global performance metric were informative, but had limitations in identifying a best approach and single parameter set. For one thing, the LBE_o data did not constitute a complete set of all LBEs, therefore the ability to optimize parameters was unrealistic. Further, the metrics did not address all mapping issues or errors such as over- or under-segmentation. Thus, metrics were coupled with visually based qualitative assessment of mapping performance covering the entire study segment to select one approach and parameter set used to generate LBEs for whole study segment (‘preferred dataset’).

Mapping performance of the preferred dataset was considered accurate if PA and MJI scores exceeded the median benchmark values provided above. However, LBEs from the preferred dataset were still not without uncertainty, which could influence answering study questions 2 and 3. Therefore, two additional steps were taken to filter out uncertain LBEs (Text S3.3). First, LBEs were removed where the majority of topographic data was from imagery-derived bathymetric estimates or augmented points (section 3.1; Text S3.1). Second, LBE polygons were removed where topographic data resolution and/or topographic variability were relatively low, presuming these would result in poor LBE predictions. This was accomplished by comparing lidar point densities and mean standard deviation in elevations ($\overline{\sigma_z}$) within LBE_o and LBE_p polygons from the preferred dataset to set thresholds for these metrics below which LBE_p polygons were removed. The final set of LBE polygons was used for all further analysis in this study. The minimum LBE polygon size was a single raster cell (0.46 m x 0.46 m). D_c values for each LBE were set as the max RSM value within each polygon.

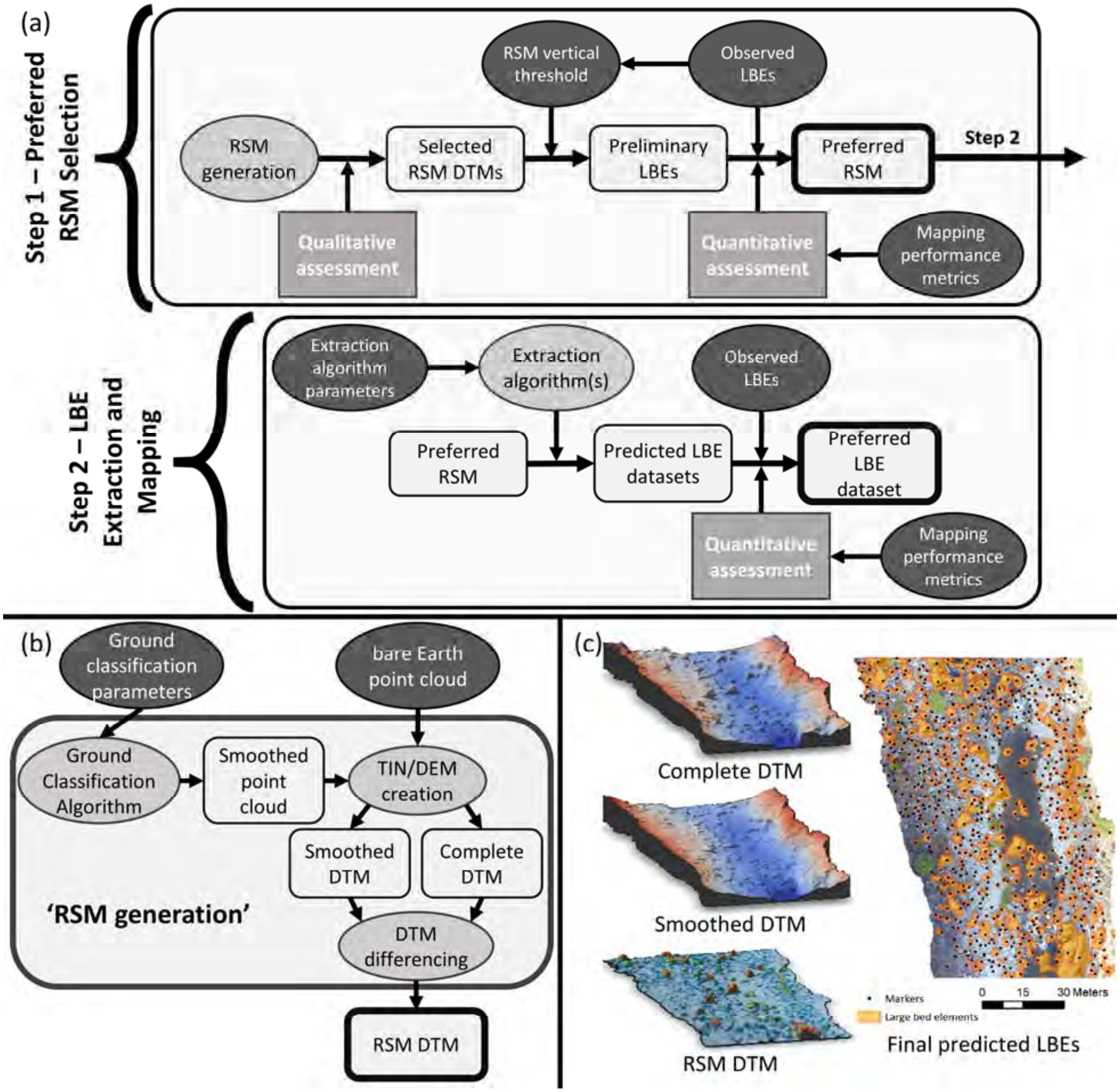

Figure 4. (a) Flowchart depicting simplified large bed element (LBE) mapping procedure with (b) detail of 'RSM generation' process and (c) oblique views of example complete, smoothed, and roughness surface model (RSM) digital terrain models (DTMs) from a small portion of the study site with resultant final predicted LBEs. In (a) and (b) light-gray rounded rectangles with dark text are output data, gray ovals with dark text are processing steps, dark-gray ovals with white text are input parameters or input data, and gray rectangles with white text are assessment steps. Arrows indicate directionality and interactions that generate new outputs or inform process steps/inputs. Key outputs from step 1 (preferred RSM) and step 2 (preferred LBE dataset) are outlined in bold.

Table 1. Ground classification algorithm parameter descriptions, range used in study, and details for large bed element (LBE) mapping†.

Parameter	Description‡	Range used in study (m)	Information used to select range	LBE mapping details‡
Step	Window size used to select points to be iteratively classified.	1.52-4.57	DTM/RSM raster cell size	Controls removal of cohesive terrain features such that features larger than the window-size are preserved in ground classification (Zhang and Whitman, 2005). Recommend setting larger than planform diameter of average LBEs but less than maximum LBE diameter and/or scale of dominate terrain features. Length of ~3-9 raster cells used to set range in this study.
Bulge	Specifies how much the TIN is allowed to bulge up when including points as it is getting refined.	0.03-0.30	Preliminary testing and user manual	Typically 1/5-1/10 step size, smaller values recommended for creating a smoothed DTM.
Spike	Threshold at which points forming spikes above the coarsest TIN get removed.	0.03-0.50	Representative grain sizes and minimum LBE heights from previous studies	Length scale(s) collectively control if points are classified as ground or removed based on how much points extend below or protrude above an otherwise smooth but variable bed surface. Estimated D_{50} (0.128-0.256 m) and D_{16} (0.032-0.064 m) values (YCWA, 2013), and two representative LBE sizes for boulders from the Udden-Wentworth scale (Wentworth, 1922), 0.256 m and 0.5 m, used to set range in this study.
Down-spike	Threshold at which points forming spikes below the coarsest TIN get removed.	0-0.50		
Offset	The maximal offset up to which points above the current ground estimate get included.	0.03-0.50		
Intensity	Specifies the search level for initial ground point classification.	extra-hyper	Preliminary testing and user manual	Use intense search setting (hyper, ultra, extra) for steep, hilly terrains and simplified search settings (fine, coarse) for flat terrains.

†Acronyms in table are as follows: digital terrain model (DTM), roughness surface model (RSM), triangular irregular network (TIN), and D is grain size diameter and subscript is percent of grains finer.
‡See http://lastools.org/ for more details

3.4. Two-dimensional hydrodynamic modeling

Wetted areas were required to assess the discharge-dependent LBE spatial structure in different portions of the channel. Wetted areas were generated from steady-state hydrodynamic simulations performed at ~1-m resolution using the free, public, 2D model, Sedimentation and River Hydraulics—Two-Dimensional model (SRH-2D) v. 2.2 (Lai, 2008). This is a proven code capable of simulating hydraulic conditions in mountain rivers with abundant LBEs (Brown and Pasternack, 2014; Strom et al., 2016). Simulations were run for four discharges (1.54, 10.73, 82.12, and 343.6 m^3/s) from an approximate baseflow to a ~3.5-yr flood. Model development, parameterization, and performance assessment are thoroughly documented in the supplementary materials file (Text S3.4). The 2D model performed comparably to similar published models (e.g. Lisle et al., 2000; Pasternack et al., 2006).

3.5. LBE spatial analysis

Having extracted a set of accurate LBE polygons from ALS point clouds, four subsets of the data were made comprising the set of final LBE polygons that intersected with the wetted area polygon of each simulated discharge. In this manner, discharge served to hierarchically nest spatial domains, since lower discharge wetted areas were always located within higher discharge wetted areas. These data are referred to herein as 'discharge-dependent LBE datasets'. From these data, LBE spatial structure was characterized in terms of concentration (Γ) and spacing (λ) metrics to answer questions 2 and 3. Specifically, metrics were used to classify segment, reach and cross-sectional spatial domains according to Morris' hydrodynamic regimes to assess if LBEs were configured to maximize flow resistance, per question 2. Concentrations were also analyzed by lateral distribution per question 3.

3.5.1 Spatially stratified LBE concentrations

Each LBE is a polygon with a plan view (2D) area. To geospatially quantify Γ, it is defined as the areal proportion of LBE polygons within any larger domain. In this study, the larger domain varied depending on the analysis.

For question 2, the larger domain was the river's wetted area at a given discharge clipped to different portions of the study segment depending on the analysis scale. First, Γ was computed at the segment scale four times, once per discharge investigated (section 3.4) by clipping the LBE polygons with a wetted area polygon. This yielded four segment-scale wetted area Γ values. In addition, 24 more reach-scale wetted area Γ values were computed by clipping each discharge's segment-scale wetted area and the LBE polygons with the individual polygon for each of the six geomorphic reaches. The final segment- and reach-scale spatially stratified dataset consisted of 28 Γ values. Lastly, longitudinal Γ profiles were generated for the full extent of each wetted area at abutting 3-m wide, cross-sectional polygons stationed along the river corridor (Text S3.5). Cross-sectional Γ values were calculated by dividing the area of LBE within each cross-sectional polygon by the polygon's area. This cross-sectional analysis provides the resolution of LBE patterns needed to evaluate local topographic, hydraulic, and morphodynamic factors compared to what is possible with averages at segment and reach scales.

To answer question 3, the four segment-scale wetted areas were used to create three incremental inundation corridor polygons. Incremental inundation corridor is defined as the river's terrain that is dry at a lower discharge and wet at a higher discharge (Figure 5). LBE polygons were clipped by each incremental inundation corridor polygon and Γ was computed for each of these three domains. These domains isolate analysis to the series of adjacent, non-overlapping regions of the river corridor that become successively inundated and geomorphically active with increasing discharge. In addition, each segment-scale incremental inundation corridor was clipped by the geomorphic reach polygons, once again yielding 28 domains (4 flows times six reaches plus 4 whole-segment flow areas) for testing.

3.5.2 LBE spacing calculations

Next, LBE-to-LBE spacings were used to further evaluate LBE spatial structure and as a second test of whether LBEs were organized to maximize flow resistance. First, longitudinal (streamwise) distances between upstream and downstream LBEs (λ^l) were estimated using a channel-oriented, path-based approach (Figure 6; Text S3.5). Distances were non-dimensionalized (λ^l_*) by dividing each λ^l by the D_c value of the upstream LBE. Because multiple paths could emanate from each upstream LBE, LBEs could have multiple λ^l_* values. Thus, a single spacing value ($\widehat{\lambda^l_*}$) was calculated for each LBE as the median of all λ^l_* values. Next, each LBE was assigned to the discharge-dependent cross-section containing the LBE polygon's centroid. Finally, $\widehat{\lambda^l_*}$ values for all LBEs originating in each cross-section were averaged yielding one spacing value per cross-section per discharge ($\overline{\lambda^l_*}$).

3.5.3 Hydrodynamic regime and flow resistance inferences

All Γ and $\overline{\lambda^l_*}$ values were framed according to Morris's (1959) hydrodynamic regimes to evaluate spatial patterns and the dynamic percentage of channel in each regime, and test for conditions that maximize flow resistance at the designated spatial scales. Synthesizing multiple studies, bounds for Γ regime classification were set such that $\Gamma < 0.08$ (e.g. 8 % percent of spatial domain) corresponded to the isolated roughness regime, Γ values between 0.08 and 0.30 to the wake interference regime, and $\Gamma > 0.30$ were classified as skimming flow (Nowell and Church, 1979; Ferro, 1999; Papanicolaou et al., 2001; Canovaro et al., 2007; Fang et al., 2017). Regime classification for $\overline{\lambda}_*^l$ used spacing thresholds reported by Papanicolaou and Tsakiris (2017), where $\overline{\lambda}_*^l > 6 \cdot D_c$ corresponded to the isolated roughness regime, $\overline{\lambda}_*^l$ values between 2 and $6 \cdot D_c$ to wake interference, and $\overline{\lambda}_*^l < 2 \cdot D_c$ to skimming flow (also see Gippel et al., 1996; Tan and Curran, 2012). Since $\overline{\lambda}_*^l$ calculations were done at the cross-sectional scale and it was desirable to have segment- and reach-scale spacing based regime classifications, individual $\widehat{\lambda}_*^l$ values in each discharge-dependent segment and reach domain were classified using the same $\overline{\lambda}_*^l$ regime thresholds as above. Domains were then classified as the single regime having the highest percentage of classified $\widehat{\lambda}_*^l$. In this manner each spatial domain was assigned a regime classification using both Γ and a spacing metric ($\overline{\lambda}_*^l$ or $\widehat{\lambda}_*^l$). Conditions of maximum flow resistance were assumed to correspond to the wake interference regime (Section 1.3). Thus, this criterion was used to test if LBEs were configured to maximize flow resistance for each metric for each spatial domain as appropriate to answer question 2. Cross-section regime classifications were further used to characterize local spatial variability, or lack thereof, in tendencies to maximize flow resistance.

Lastly, regime predictions from segment- and reach-scale Γ and $\widehat{\lambda}_*^l$, and cross-sectional Γ and $\overline{\lambda}_*^l$ values were compared for consistency in the form of confusion matrices showing the number of regimes classified similarly and how regime classifications differed between metrics, if this occurred. To interrogate metric appropriateness, LBE counts and median LBE areas were calculated at each channel cross-section. These metrics are also linked to local flow resistance (e.g. Gippel et al., 1996; Canovaro et al., 2007) and serve as an independent check on the ability of Γ and $\overline{\lambda}_*^l$ to characterize LBE spatial structure. These data were stratified by classification regime for each metric, Γ and $\overline{\lambda}_*^l$, independently, and statistical distributions were heuristically compared. Interpretation was that less overlap in distributions between regimes for the same metric was an indicator of better classification accuracy, since regimes correspond to different levels of flow resistance (Fang et al., 2017). Cross-sectional LBE counts and median LBE area data were also compared between sections classified the same and differently by each metric to help explain potential discrepancies in cross-section classifications (Text S3.5).

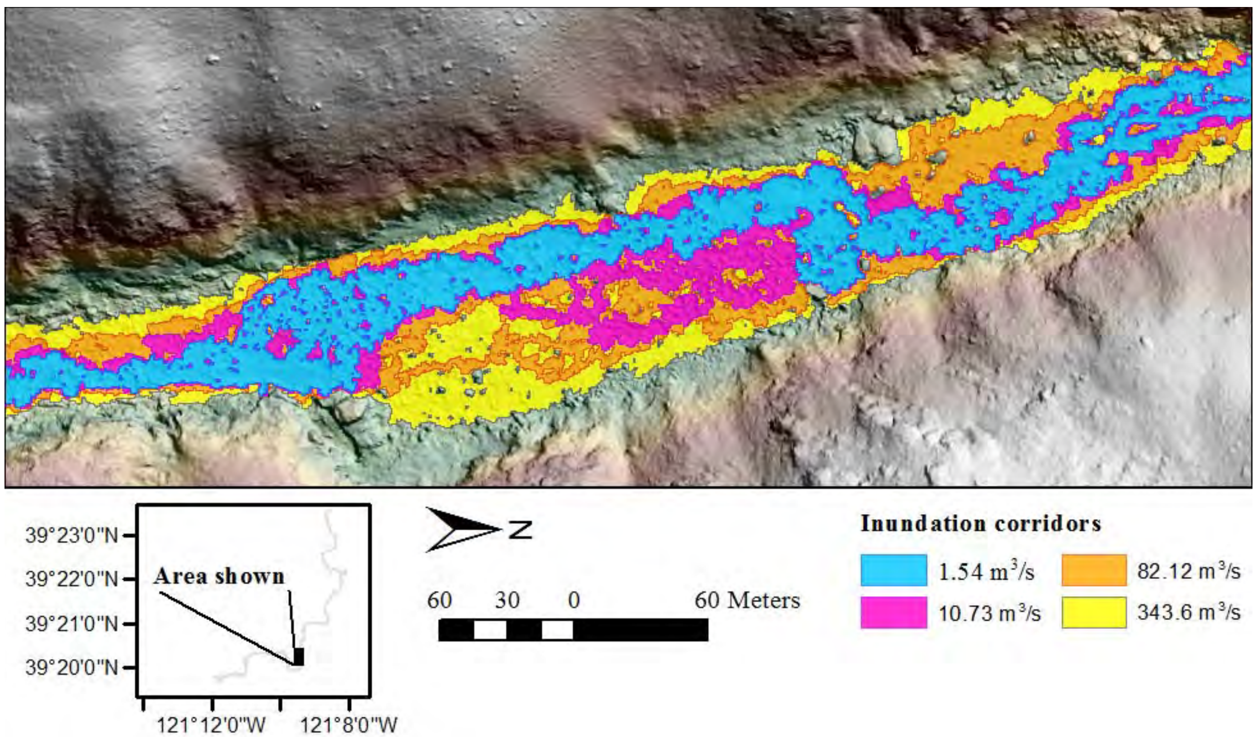

Figure 5. Typical output from 2D model simulations showing the baseflow wetted area (blue) and the subsequent incremental inundation corridors occurring as strips between successive higher discharges. For example, pink is the incremental inundation corridor between 1.54 and 10.73 m^3/s. Flow is from right to left.

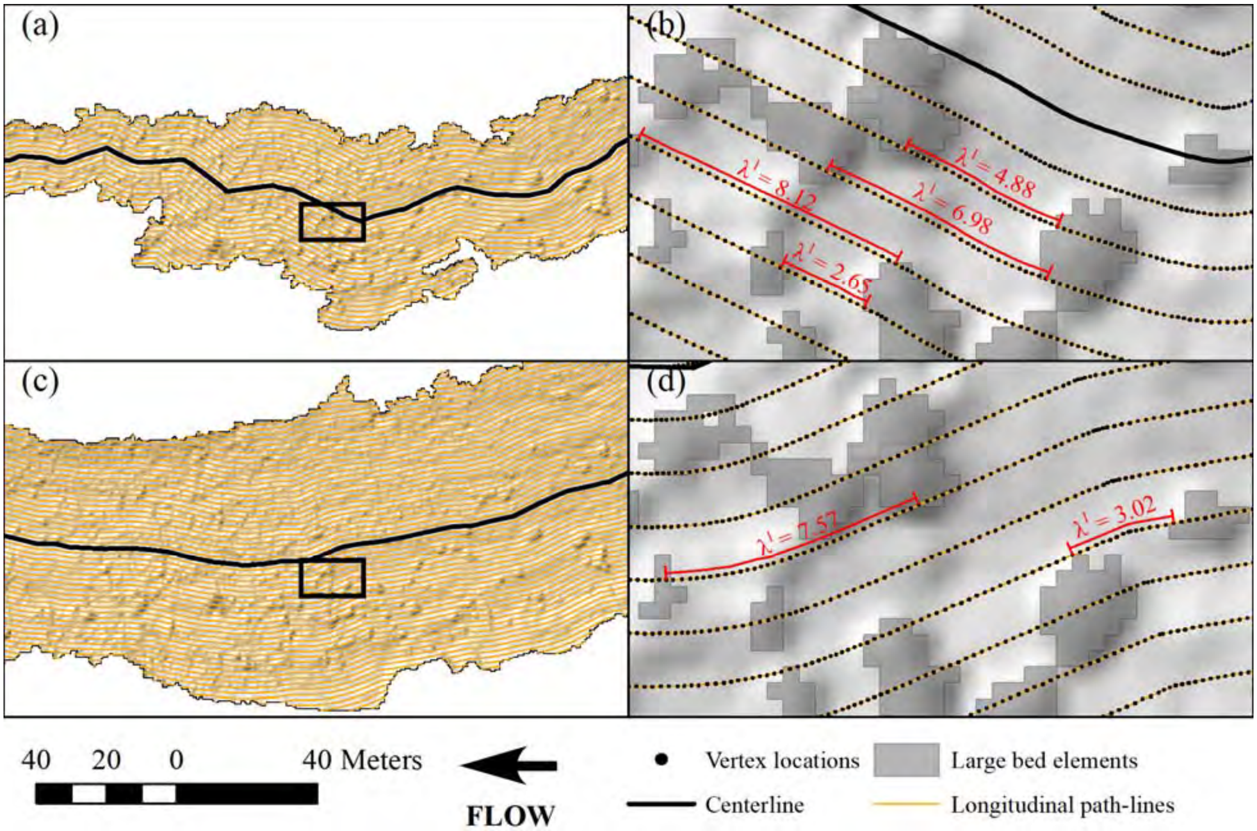

Figure 6. Arbitrary portion of the study segment illustrating path approach for large bed element-to-large bed element (LBE-to-LBE) spacing analysis depicting set of offset longitudinal path-lines for (a) 1.54 m^3/s and (c) 343.6 m^3/s discharge simulations. (b) and (d) depict zoomed in views of the inset boxes shown in panels (a) and (c) showing path-lines, LBEs, and densified vertices used in calculating non-dimensional LBE spacing ($\boldsymbol{\lambda}_*^{\boldsymbol{l}}$) values. Example longitudinal LBE spacing (λ^l) measurements along path-lines between upstream and downstream LBEs are depicted in red in panel (b) and (d). (For interpretation of the references to colour in this figure legend, the reader is referred to the web version of this article.)

4. Results

4.1. Question 1 results (LBE mapping)

Qualitative assessment of the 14 smoothed DTMs determined certain ground classification parameter sets performed better than others (Table S3). Generally, larger step sizes (~3 and 4.5 m), smaller spike and offset values (0.128 m [D_{50}] and 0.064 m [D_{16}] versus 0.5 m), and intermediate down-spike values (0.128 m, 0.256 m, and 0.15 m) were best at filtering-out LBEs while maintaining character of the overall terrain. Ultimately, the study site’s estimated

D_{50} (0.128 m) was identified as the best measure for the spike and offset parameters, together with a slightly larger value of ~2·D_{50} (0.256 m) for the down spike parameter.

Quantitative assessment of preliminary LBEs mapped from the best six smoothed DTMs found P-LBE-10 to perform best, making the associated RSM the preferred RSM (Table S11). Preliminary LBEs from this RSM had the best global performance metric and second best MJI (0.183), MER (0.014), and PA (0.836) scores. PA scores for all six preliminary LBE datasets were between 0.794 and 0.864 and MJI scores were between 0.107 and 0.212. These values are near the high end of the benchmark values reported by Kaartinen et al. (2012) and Marconi et al. (2019), indicating an accurate representation of observations.

Comparing performance metrics between extraction approaches, there were within-approach and between-approach differences, with no one approach being best for all metrics. Correlations between performance metrics were also weak ($r < |0.57|$), thus supporting the use of multiple performance metrics. Selective results from the five LBE extraction approaches are presented in Table 2 with complete results for all 44 LBE_p datasets in Table S12. Between approaches, Gaussian filtered RSMs generally resulted in lower PA scores but higher PO scores, suggesting filtering produced fewer predicted LBEs but those that were mapped had good correspondence with coincident observed LBEs. One issue encountered with Gaussian filtering was rescaling of RSM values, as this complicated attempts to use physically-based metrics for parameter selection. With regard to PO, MJI, and global performance metrics, MCWS approaches (iii–v) performed better than vertical threshold approaches (i and ii). Trends for MER scores were not consistent, but vertical threshold approaches appeared to outperform MCWS approaches. No distinction was present between MCWS and vertical threshold approaches for PA performance as variation was more strongly controlled by within-approach parameters.

Within approaches, larger parameter values for marker detection and feature extraction in the MCWS algorithm (Text S3.3) and larger vertical thresholds acted to reduce the spatial extent of LBE mapping. All else being equal, this had the effect of decreasing PA and PO scores and increasing MJI and MER scores. The interpretation here is that more constrained LBE mapping reduced commission errors at the expense of creating omission errors. Overall, tested approaches performed comparatively well as all datasets exceeded the selected MJI benchmark of 0.164, and 40 of 44 datasets exceeded the PA benchmark of 0.56. However, since MCWS approaches consistently performed best, they are recommended over vertical threshold approaches when mapping LBEs or similar landscape features.

Based on performance metrics and visualizing predicted LBE polygons, the MCWS-V-2 dataset from approach (iv), RSM with MCWS and variable window size, was selected as the preferred LBE dataset. Values for the main MCWS parameters controlling the minimum RSM value for a pixel to be considered a marker (minimum marker RSM height) and the minimum RSM value for a pixel to be included in the segmentation (minimum crown RSM height) for the MCWS-V-2 dataset were scaled to ~$2.4 \cdot D_{50}$ (0.312 m) and ~$2.1 \cdot D_{50}$ (0.272 m), respectively (Text S3.3.2; Table S12). This dataset had the 27th best PA score (0.756), 33rd best PO score (0.720), 7th best MJI score (0.45), and 3rd best MER score (0.086) but had the 3rd best global performance metric score, thus representing a balance between accuracy and precision that favored avoidance of commission errors over excess prediction. PA and MJI scores also exceeded the specified benchmark thresholds, thus this dataset's LBE mapping was considered satisfactory. Qualitatively this dataset also performed well with regard to LBE segmentation. For instance, while datasets MCWS-C-6 and MCWS-C-8 from approach (iii), RSM with MCWS and constant window size, had better global performance metric scores, visualization found resulting

LBEs were over-segmented (Figure 7). Notably, no approach was able to discern boulders from bedrock outcrops or fully decouple individual boulders from boulder clusters, meaning, at times, clusters were aggregated into individual polygons.

Like many predictive sedimentological models there is potential for overfitting parameter values of the MCWS-V-2 dataset to the LBE_o data used for calibration and validation that could result in poor mapping performance when applied to the study segment as a whole. However, since the main MWCS parameters only define minimum RSM threshold values for what constitutes an LBE, mapping performance was consistent across the RSM and would only be impacted if the definition of an LBE substantially changed between reaches. Based on expert opinion, the set of observed LBEs was assumed representative of LBEs in the study site, and thus presumed suitable for specifying parameters to be applied to all study reaches. The fact that LBEs were mapped in varying abundances throughout the study site with only small areas lacking any LBEs is taken as reasonable support of this assumption. Qualitative assessment of mapped LBEs over the whole of the study segment and the fact that MCWS parameters were not set to optimize performance metrics also reduced potential overfitting.

Prior to filtering, MCWS-V-2 mapped a total of 46,471 individual LBEs in the study site. Of these, 302 LBEs (0.6 %) were completely removed and an additional 497 LBEs (1.0 %) were partially removed due to uncertainty in topographic source data. After this initial filtering, an additional 2722 LBEs (5.9 %) did not meet the identified lidar point density criteria (>2.9 pts/m2) and 3081 LBEs (6.7 %) did not meet the $\overline{\sigma_z}$ criteria (>0.03 m) resulting in 3993 more LBEs (8.6 %) being removed, leaving 42,176 polygons in the final LBE dataset (Text S3.3.2). Geometrically the final set of LBE polygons had D_c values (i.e., heights) ranging from the minimum of 0.312 m to 19.7 m and areas ranging from 0.2 to 234.4 m^2 (Figure 8). Filtering and the tendency to favor low commission over omission errors meant the final mapping underestimated the total number of LBEs. Lastly, while focus was on mapping boulders and bedrock outcrops, LWM would be included in the final dataset if features met parametric mapping criteria, though previous surveys suggest low densities of LWM in the study site (YCWA, 2013).

Table 2. Selected performance metrics of predicted large bed element datasets with best and worst global performance score for each mapping approach. Maximum values for each metric are highlighted in light-gray and minimum values are italicized. Preferred dataset in bold and underlined†.

ID	PA	PO	MJI	MER	Global Performance (Normalized mean)
(i) RSM with vertical threshold					
V-1	0.894	0.774	0.269	0.030	0.445
V-11	0.669	*0.659*	0.371	0.086	0.521
(ii) Gaussian filtered RSM with vertical threshold					
GV-1	0.760	0.705	0.333	0.054	0.458
GV-3	*0.611*	0.779	*0.246*	0.051	*0.352*
(iii) RSM with MCWS and constant window size					
MCWS-C-8	0.798	0.715	0.464	0.083	0.738
MCWS-C-10	0.809	0.828	0.392	0.025	0.581
(iv) RSM with MCWS and variable window size					
MCWS-V-1	0.760	0.715	0.460	0.083	0.714
MCWS-V-2	**0.756**	**0.720**	**0.450**	**0.086**	**0.718**
(v) Gaussian filtered RSM with MCWS and constant window size					
GV-MCWS-C-3	0.712	0.810	0.436	0.057	0.674
GV-MCWS-C-14	0.780	0.874	0.339	*0.020*	0.535

†Acronyms in table are as follows: producers accuracy (PA), producers overlap (PO), modified Jaccard similarity index (MJI), missed-to-excess ratio (MER), roughness surface model (RSM), and marker controlled watershed segmentation (MCWS).

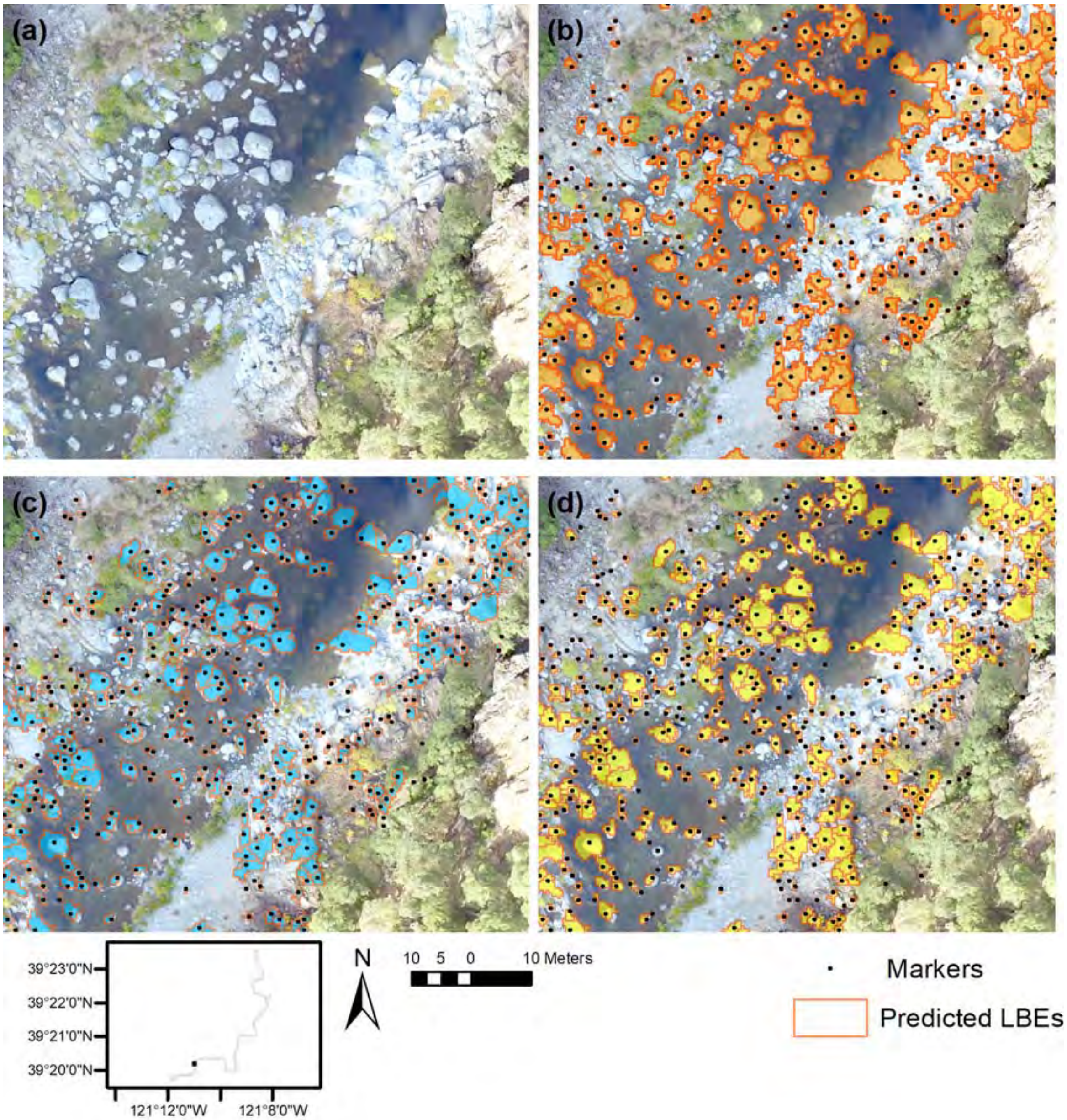

Figure 7. Comparison of large bed element (LBE) segmentation performance among algorithms. (a) uncrewed aerial system image, (b) MCWS-V-2, (c) MCWS-C-6, and (d) MCWS-C-8. Note tendency for greater polygon segmentation in panels (c) and (d). MCWS-V-2 (b) was selected as the preferred LBE dataset.

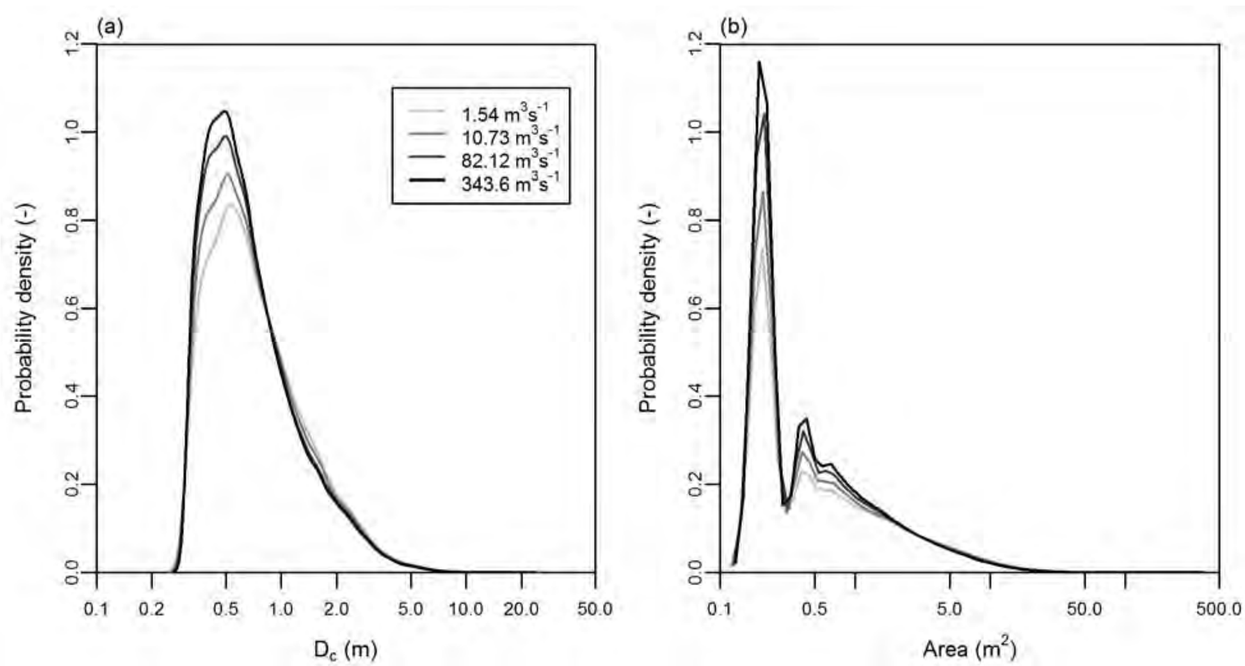

Figure 8. Overlain kernel densities of large bed element (LBE) (a) diameter (D_c), and (b) area probability densities for the four discharge-dependent LBE datasets. Note, x-axis is plotted on a log-scale.

4.2. LBE concentrations

LBEs were present individually and in clusters throughout the river corridor. Visually speaking, LBEs conformed to a variety of morphological configurations. Clustered LBEs appeared in seemingly random as well as organized arrangements often forming transverse orientations and step-like structures. Reticulate configurations were discernable but more difficult to identify (Figure 9).

At the segment scale, Γ of each wetted area monotonically increased from 18.2 % at baseflow to 26.5 % at flood-flow (Table 3). The trend indicates that as discharge increased the rate at which new LBE area was inundated (e.g. within the wetted area) exceeded the rate that new portions of the river corridor became inundated. This was facilitated by increasingly higher

Γ values in each incremental inundation corridor (Table 3) and meant that, on a per-wetted-area basis, increasingly higher Γ existed along channel margins.

Reach-scale results also found wetted area Γ to increase with discharge, although Reach 6 had nearly uniform values across discharges (Table 3). Changes in reach-scale wetted area Γ were also strongly influenced by inundation corridor Γ values, such that higher inundation corridor Γ generally resulted in greater increases in wetted area Γ between discharges (Figure S9). A Pearson bivariate correlation of 0.86 between the differences in reach-scale wetted area Γ between subsequent discharges and inundation corridor Γ values supports this interpretation. Across discharges, reaches showed consistent trends in relative Γ magnitude. For instance, while each reach's wetted area Γ values varied with discharge, ranking values at any given discharge resulted in the same ordering across all discharges. As such, Reach 2 always had the highest wetted area Γ, whereas Reach 6 was always lowest. This consistent ordering suggests possible reach-scale wetted area Γ dependencies on hillslope and fluvial geomorphic, topographic, and geometric factors influencing LBE supply, storage, and/or transport.

Cross-sectional Γ trends for each wetted area varied spatially and with discharge (Figure 10). Mainly, the increased granularity of these results highlight Γ spatial variability and tendencies for semi-oscillatory and more irregular LBE patterns. Longitudinally, Γ profiles were characterized by constant high-frequency oscillations of varying amplitude and non-constant low-frequency fluctuations (Figure 10). The non-parametric Mann-Kendall test indicated slight, but non-trivial ($p < 0.05$), decreasing downstream trends in all profiles. Comparison of all possible profile combinations found relatively high correlations ($r > 0.8$). Key features recurring throughout the profiles were sequences of LBE clustering as indicated by rising limbs in the profiles, which peaked or temporarily plateaued, and subsequently declined along diffusive style decay pathways. These patterns were emphasized after processing profiles with a 130 m (5 widths) centered moving-window mean filter.

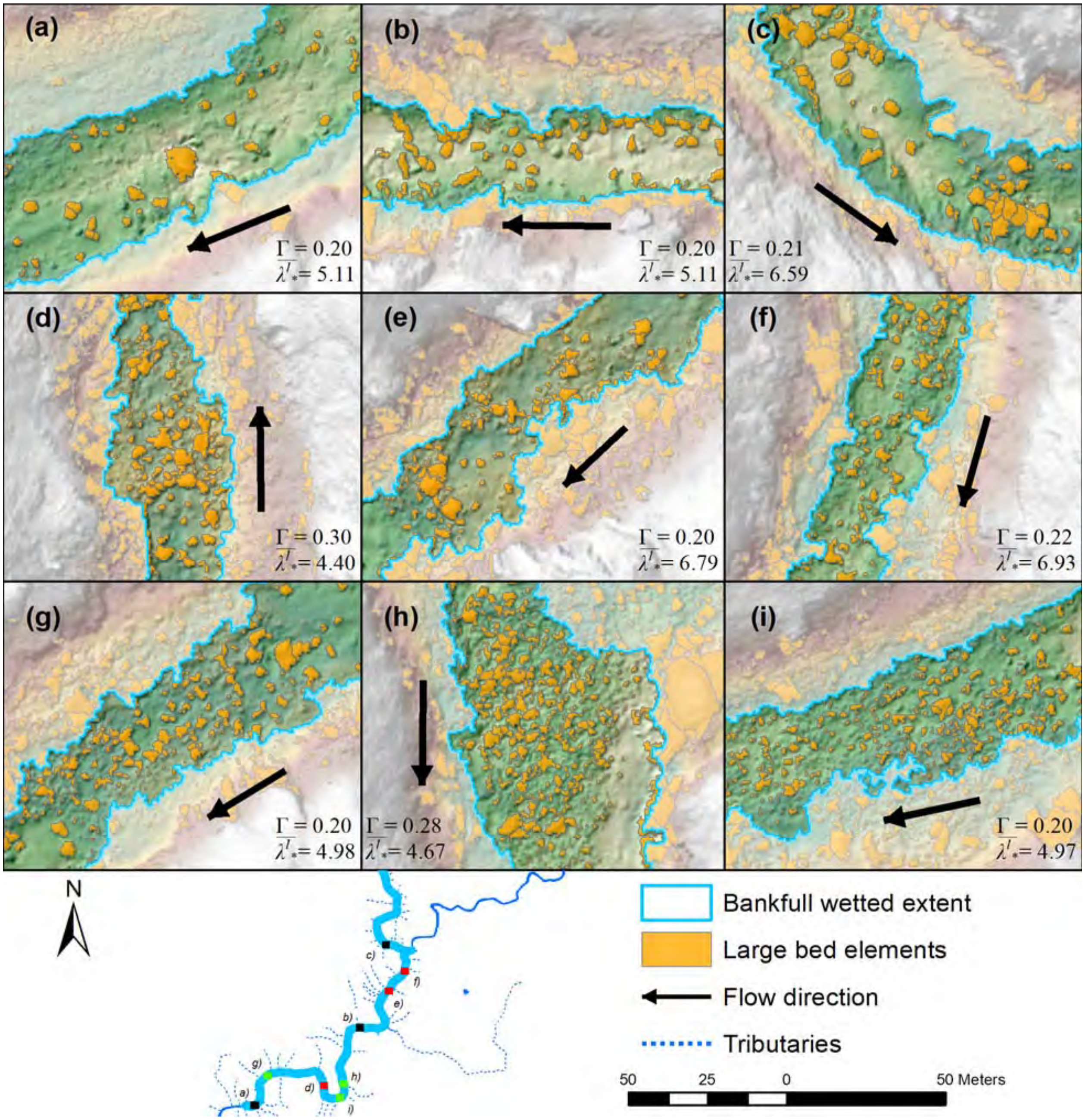

Figure 9. Typical configurations of clustered and individual large bed elements (LBEs) within the study site's bankfull channel overlain on shaded detrended relief that include (a-c) low concentration, isolated and clustered LBEs; (d-f) moderate concentration, transverse and step structures; and (g-i) high-concentration mixtures of steps, transverse structures and possible reticulate formations. LBEs outside the bankfull channel are partially transparent. Representative LBE concentration (Γ) and cross-sectionally averaged non-dimensional LBE spacing ($\overline{\boldsymbol{\lambda}^{\boldsymbol{l}}_*}$) values for each panel are shown. These values were calculated by averaging bankfull cross-sectional Γ and $\overline{\boldsymbol{\lambda}^{\boldsymbol{l}}_*}$ values for all cross-sections present in each panel.

Table 3. Discharge-dependent large bed element concentration (Γ) within each simulated wetted area and inundation corridor for study segment and reaches. Values between 0.08 and 0.30 are within the wake interference regime and are highlighted in gray.

Reach	Wetted area Γ				Incremental inundation corridor Γ		
	Simulated discharge (m^3/s)				Discharges bounding inundation corridor (m^3/s)		
	1.54	10.73	82.12	343.6	1.54 - 10.73	10.73-82.12	82.12-343.6
Segment	0.182	0.211	0.242	0.265	0.321	0.329	0.348
1	0.161	0.181	0.212	0.236	0.257	0.301	0.340
2	0.230	0.269	0.310	0.332	0.411	0.428	0.414
3	0.191	0.218	0.255	0.286	0.346	0.368	0.386
4	0.225	0.261	0.288	0.304	0.372	0.369	0.364
5	0.150	0.178	0.207	0.235	0.295	0.300	0.328
6	0.089	0.098	0.099	0.102	0.167	0.102	0.114

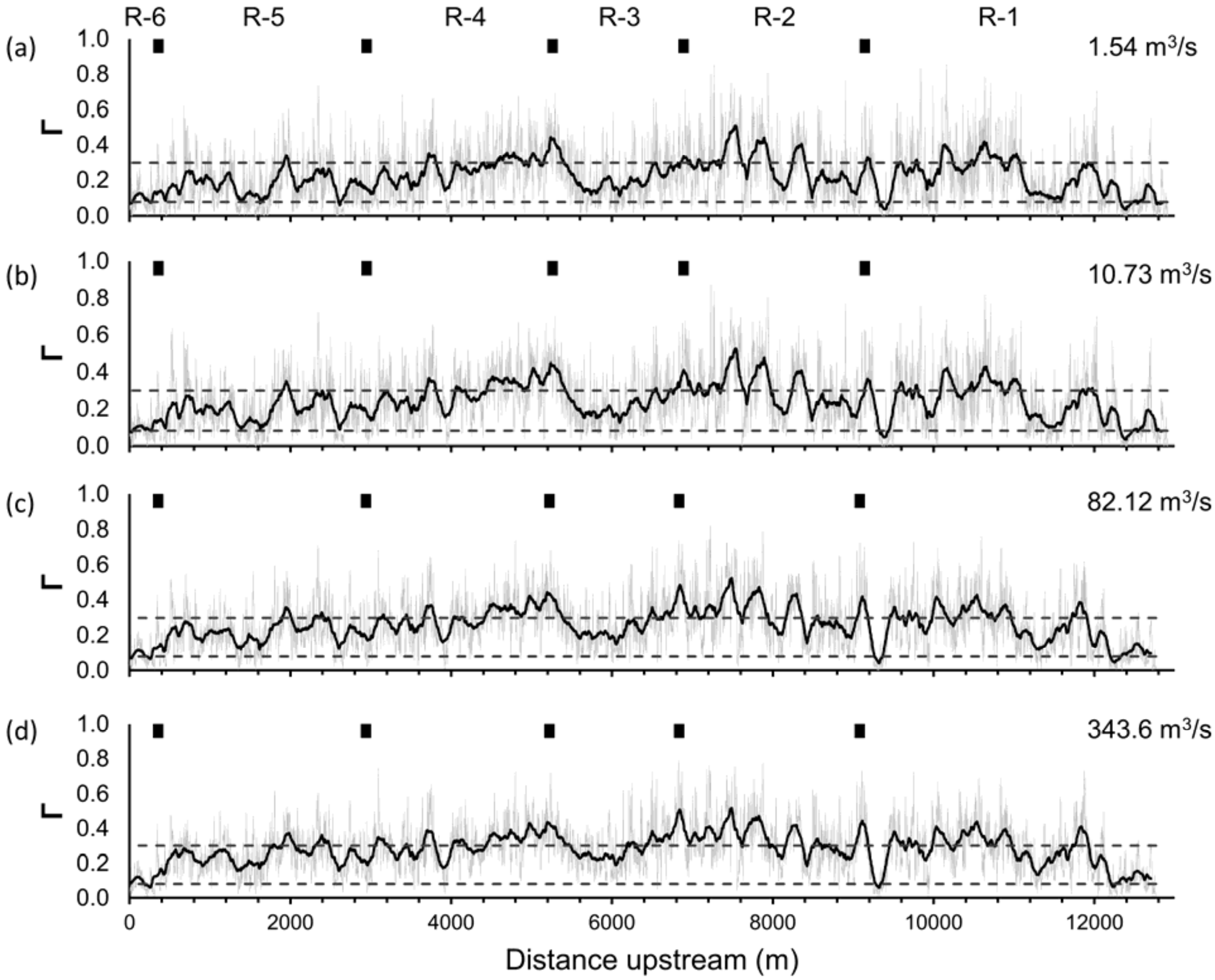

Figure 10. Longitudinal profiles of cross-sectional large bed element (LBE) concentration (Γ) values for each discharge-dependent LBE dataset. Light-gray lines are values at each cross-section. Black lines are moving average within a 130 m centered moving window. Dashed horizontal lines are thresholds for Morris's (1959) hydrodynamic regimes at 0.08 and 0.30, respectively. Black vertical markers at top show reach breaks.

4.3. LBE spacings

Discharge-dependent streamwise spacing metrics (λ^l, λ_*^l, and $\widehat{\lambda_*^l}$) spanned a wide range but always had positively skewed distributions showing a strong tendency for closely spaced LBEs (Figure S10). The $\widehat{\lambda_*^l}$ results, which were for individual LBEs, depict clear clustering trends (Figure S10), whereas $\overline{\lambda_*^l}$ longitudinal profiles, which depict spacing averaged at the cross-sectional scale, illustrate greater variability in spacing behavior (Figure 11). For instance, $\overline{\lambda_*^l}$

profiles were quite erratic, and like Γ profiles, exhibited high-and-low frequency oscillations of varying amplitudes and consistencies.

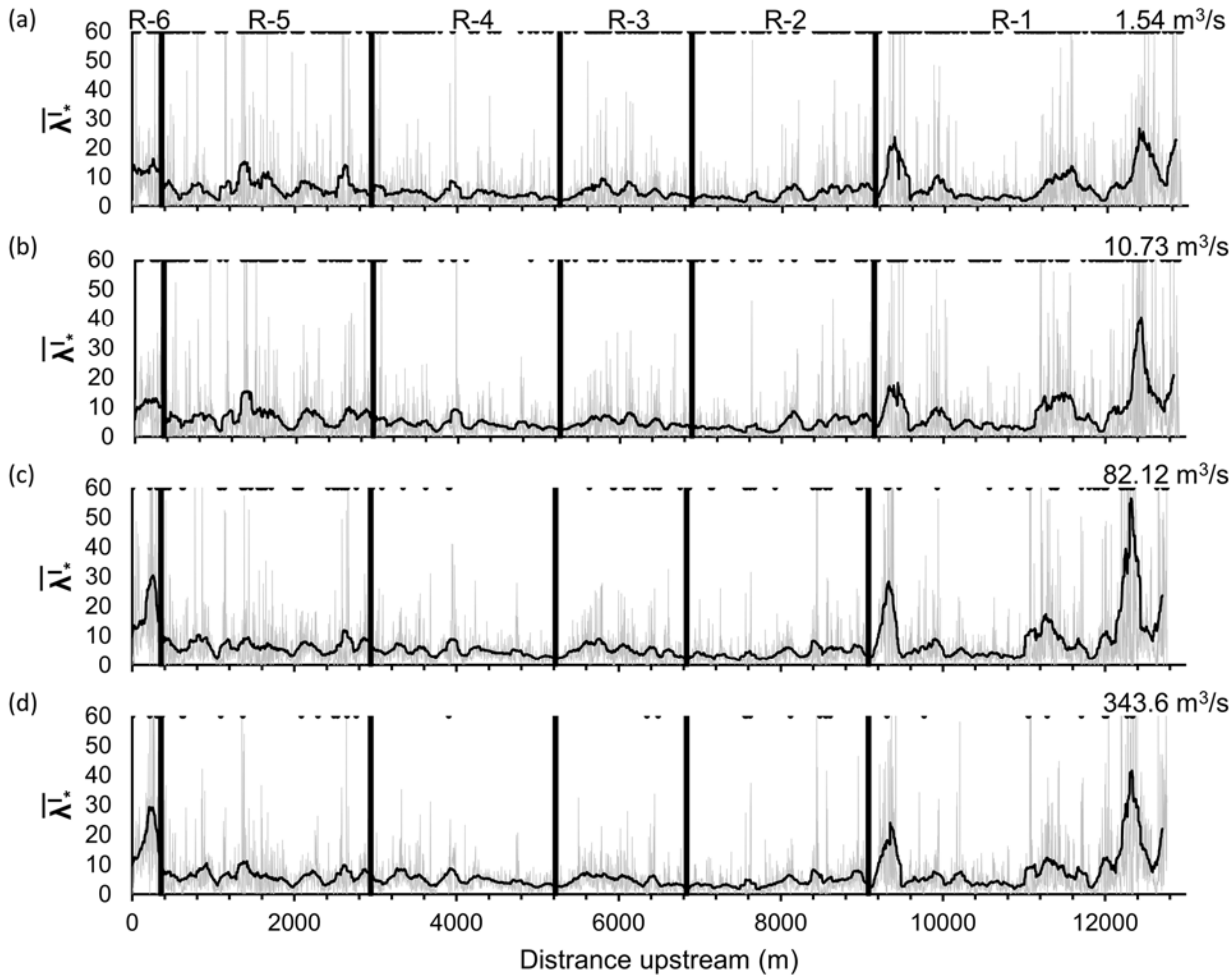

Figure 11. Longitudinal profiles of discharge-dependent cross-sectionally averaged non-dimensional large bed element spacing ($\overline{\boldsymbol{\lambda}_{*}^{l}}$) values. Light-gray lines are values at each cross-section. Black lines are moving average within a 130 m centered moving window. Dark dots along top of plot are cross-sections with zero values. Vertical black bars show reach breaks. Note the y-axis range is limited to 0-60 for visual purposes despite higher values occurring.

4.4. Question 2 results (maximum resistance)

Segment scale wetted area Γ values were all in the range of values associated with Morris's (1959) wake interference regime (Table 3). At the reach scale, 21 of 24 wetted area Γ results were also within the wake interference regime, signifying LBEs in these spatial domains were predominantly configured to maximize flow resistance. Similarly, cross-sectional Γ values found wake interference to be the most common regime in all segment scale wetted areas and in 18 of 24 reach-scale wetted areas (Figure 12). Across discharges and spatial domains between 42 and 66 % of cross-sections were classified in either isolated roughness or skimming flow regimes, thus demonstrating localized divergences from the wake interference regime. At higher discharges the proportion of cross-sections classified as wake interference and/or skimming flow increased as the proportion classified as isolated roughness decreased. Longitudinal profiles of cross-sectional Γ show oscillations were commonly around the thresholds of the wake interference regime (Figure 10).

Classifying segment- and reach-scale domains based on percentages of classified $\widehat{\lambda_*^l}$ values found that with the exception of Reach 6, which was always in the isolated flow regime, all domains were in the skimming flow regime (Table 4). On the other hand, percentages of classified cross-sectional $\overline{\lambda_*^l}$ values found that while skimming flow was the most prevalent regime in the segment-scale baseflow wetted area, wake interference was most prevalent in the wetted areas of the three higher discharges (Figure 13). In the study reaches, 8 of 24 wetted areas had the highest percentages of cross-sectional $\overline{\lambda_*^l}$ values in wake interference regime, 10 had the most in the skimming flow, and six had the most in the isolated flow regime (Figure 13). At higher discharges the proportion of cross-sections classified as wake interference and isolated roughness generally increased.

Trends in $\widehat{\lambda_*^l}$ and $\overline{\lambda_*^l}$ values contrast with results using Γ, which found LBE density to increase in these same domains. The differences are not mutually exclusive and could result from presence of high-density clusters of LBEs being relative widely spaced along channel margins as larger portions of the river-valley were included in the calculations, compared to more closely spaced, lower density LBE clusters in the baseflow channel. Sensitivity to the spacing thresholds used to characterize the regimes certainly exists, however these results support that LBEs were closely spaced and structured to maximize resistance at certain scales and in certain portions of the river corridor. Further, like cross-sectional Γ values, oscillations in $\overline{\lambda_*^l}$ longitudinal profiles were commonly around the thresholds of the wake interference regime (Figure 11). In this sense the wake interference regime may represent an attractor state toward which conditions, on aggregate, converge.

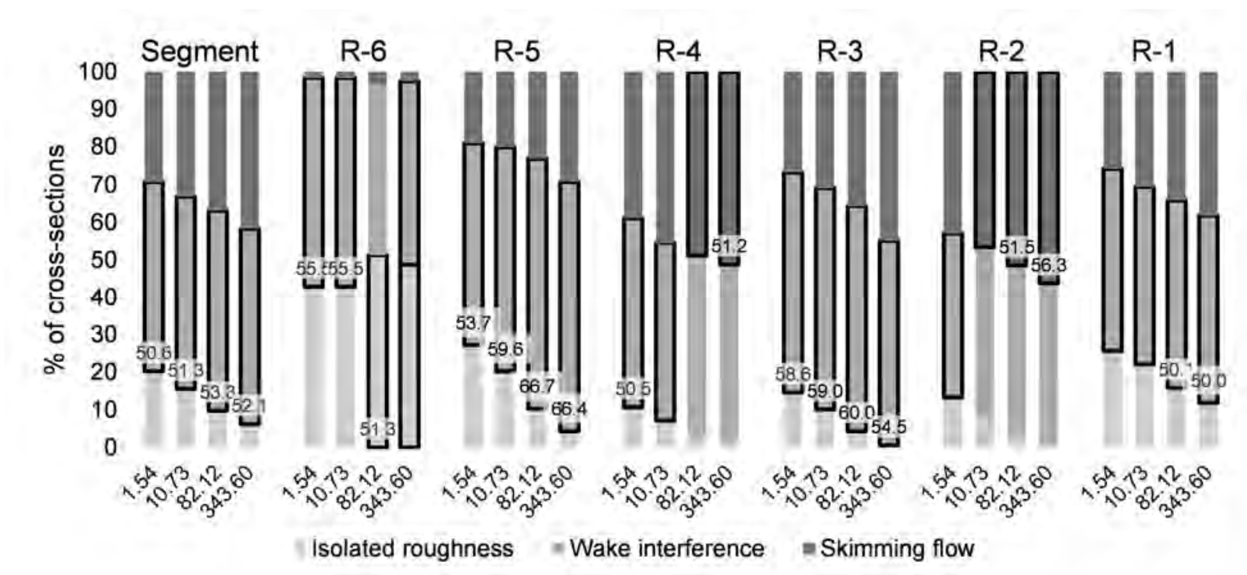

Figure 12. Percentages of cross-sectional large bed element (LBE) concentration (Γ) values by spatial domain classified according to Morris's (1959) hydrodynamic regimes for each discharge-dependent LBE dataset. Bars highlighted bold are the dominate regime for each flow. Labeled bars had majority (>50 %) of cross-sections in one regime. Reaches are ordered from left to right moving upstream consistent with Figure 10.

Table 4. Percentage of individual non-dimensional large bed element (LBE) spacing ($\widehat{\boldsymbol{\lambda}_*^l}$) values classified according to Morris's (1959) hydrodynamic regimes for each discharge-dependent LBE dataset. For each domain and flow the regime with the highest percentage of classified $\widehat{\boldsymbol{\lambda}_*^l}$ is highlighted in gray and bolded. Abbreviations are such that: IF – isolated roughness; WI – wake interference; and SF – skimming flow.

Reach	Simulated discharge (m^3/s)											
	1.54			10.73			82.12			343.6		
	IF	WI	SF	IF	WI	SF	IF	WI	SF	IF	WI	SF
Segment	23.68	28.39	**47.93**	24.25	28.94	**46.81**	25.47	28.81	**45.72**	26.25	28.35	**45.40**
1	29.14	26.91	**43.94**	29.07	27.60	**43.33**	28.50	27.78	**43.72**	28.98	26.20	**44.81**
2	17.33	24.96	**57.71**	16.95	26.79	**56.26**	17.13	26.34	**56.53**	18.01	26.51	**55.48**
3	21.75	29.83	**48.42**	22.80	29.77	**47.44**	23.91	30.74	**45.36**	23.64	29.41	**46.95**
4	17.54	30.73	**51.72**	19.19	31.14	**49.67**	22.41	30.77	**46.82**	24.16	31.44	**44.40**
5	26.42	29.85	**43.73**	28.14	30.36	**41.50**	29.53	29.68	**40.80**	29.61	29.27	**41.12**
6	**52.81**	29.21	17.98	**55.97**	23.63	20.40	**57.89**	24.26	17.85	**60.95**	22.59	16.46

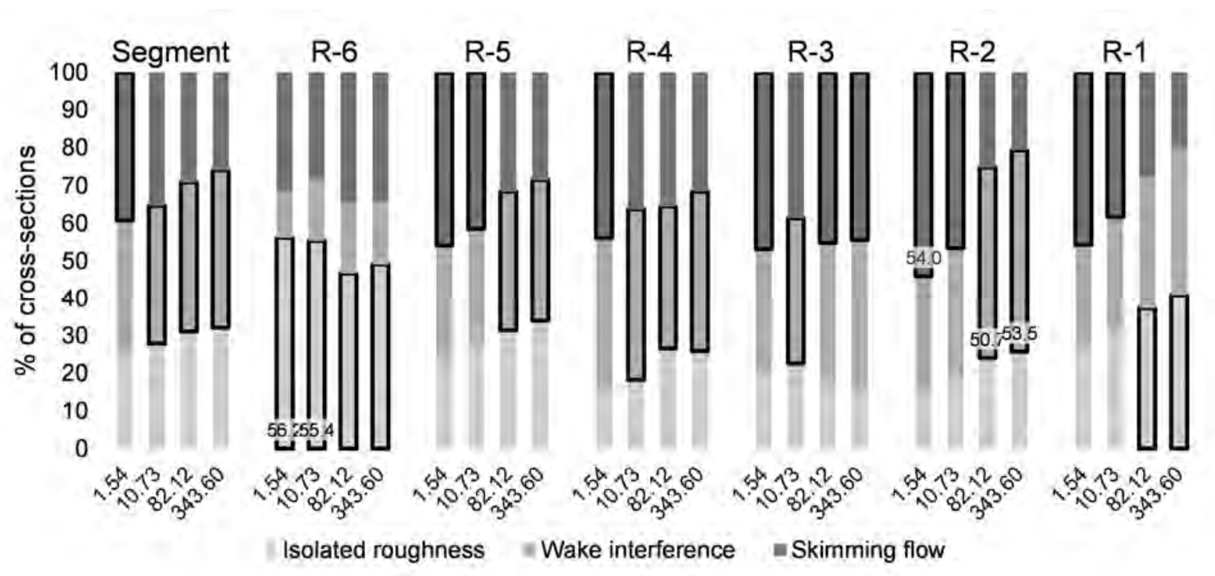

Figure 13. Percentages of cross-sectionally averaged non-dimensional large bed element (LBE) spacing ($\overline{\boldsymbol{\lambda}_*^l}$) values within the study segment and each reach classified according to Morris's (1959) hydrodynamic regimes for each discharge-dependent LBE dataset. Bars highlighted bold are the dominate regime for each flow and study domain. Labeled bars had majority (>50 %) of cross-sections in one regime. Reaches are ordered from left to right moving upstream consistent with Figure 11.

4.5. Comparing hydrodynamic regimes from concentration and spacing metrics

Numerous tests performed for question 2 using Γ and spacing metric results require reconciliation. Comparison of segment and reach-scale regime classifications by Γ and $\widehat{\lambda}^{l}_{*}$ found only 3 domains were classified the same by each metric. The two most common classification discrepancies were Γ-based wake interference sections classified as isolated and skimming flow regimes according to $\widehat{\lambda}^{l}_{*}$ values (Table 5). Comparison of all cross-sections found only 44 % were classified the same by each metric. The three most common classification discrepancies were Γ-based wake interference sections classified as isolated and skimming flow regimes according to $\overline{\lambda}^{l}_{*}$ values, and Γ-based skimming flow sections classified as wake interference by $\overline{\lambda}^{l}_{*}$ (Table 5). This resulted in greater portions of the study site classified as skimming flow according to $\overline{\lambda}^{l}_{*}$ and $\widehat{\lambda}^{l}_{*}$ compared to Γ. As mentioned in Section 4.4, uncertainty in regime thresholds could explain some of the disparity between methods. Adjusting $\overline{\lambda}^{l}_{*}$ thresholds to maximize the percent of cross-sections classified the same, with the constraint that wake interference was within the range of $1 \leq \overline{\lambda}^{l}_{*} \leq 10$, improved the percent predicted the same by both metrics to 51% and resulted in the following thresholds: isolated roughness for $\overline{\lambda}^{l}_{*} > 10$, wake interference for $3 \leq \overline{\lambda}^{l}_{*} \leq 10$, and skimming for $\overline{\lambda}^{l}_{*} < 3$. Higher $\overline{\lambda}^{l}_{*}$ values for the upper bound of the wake interference regime continued to improve consistency between metrics, but values > 10 for this threshold are not supported by the literature (Canovaro et al., 2007; Tan and Curran, 2012).

One issue that emerged when using $\overline{\lambda}^{l}_{*}$ values to classify cross-sections was if only one or a few LBEs were present per section, and all $\widehat{\lambda}^{l}_{*}$ values were small (i.e., <2), the section would be classified as skimming flow despite few LBEs being present. At the other extreme, a lack of downstream LBEs would identify a section with potentially high LBE concentrations in the isolated roughness regime. This issue was highlighted by results of comparing distributions of cross-sectional LBE counts and median LBE areas classified by Γ and $\overline{\lambda_*^l}$, which found distributions of these metrics were more distinct and generally increased when progressing from isolated flow to skimming flow for Γ classified regimes, whereas distributions were more uniform between $\overline{\lambda_*^l}$ classified regimes (Text S4.4; Figures S11 and S12). Several patterns also emerged when comparing LBE count and median LBE area distributions of similarly classified cross-sections with those having classification discrepancies (Figures S13 and S14). For instance, LBE counts of sections classified as wake interference by Γ but as isolated roughness or skimming flow by $\overline{\lambda_*^l}$ were lower than for similarly classified sections (i.e. both in wake interference regime). This is reasonable for isolated roughness regime classification discrepancies, but unexpected for sections classified in the skimming flow regime. Since median LBE areas were lower for $\overline{\lambda_*^l}$-based isolated roughness sections and higher for $\overline{\lambda_*^l}$-based skimming flow sections compared to similarly classified sections, this suggests $\overline{\lambda_*^l}$-based isolated roughness classification discrepancies might have been driven by lower numbers of smaller LBEs with longer downstream spacings compared to similarly classified sections, and that $\overline{\lambda_*^l}$-based skimming flow classification discrepancies might have been driven by lower numbers of larger LBEs with shorter downstream spacings (Text S4.4). In light of these issues and the established relationship between Γ and flow resistance (e.g. Canovaro et al., 2007; Nitsche et al., 2011), Γ is taken as a more reliable metric for the resistance based regime classification of natural channel cross-sections employed in this study.

Table 5. Confusion matrix of the number of domains classified into each of Morris's (1959) hydrodynamic regimes using (a) segment- and reach-scale large bed element (LBE) concentration (Γ) (rows) and individual non-dimensional large bed element (LBE) spacing ($\widehat{\boldsymbol{\lambda}_*^{\boldsymbol{l}}}$) (columns) values, and (b) cross-sectional Γ (rows) and cross-sectionally averaged non-dimensional LBE spacing ($\overline{\boldsymbol{\lambda}_*^{\boldsymbol{l}}}$) (columns) values. Numbers along diagonals were classified the same by both metrics. Abbreviations are such that: IF – isolated roughness; WI – wake interference; and SF – skimming flow.

(a) Segment and reach scale (n = 28)		$\widehat{\lambda_*^l}$ IR	WI	SF
	IR	0	0	0
Γ	WI	4	0	21
	SF	0	0	3

(b) Cross-section scale (n = 16,832)		$\overline{\lambda_*^l}$ IR	WI	SF
	IR	1346	435	387
Γ	WI	3411	3320	1997
	SF	866	2344	2726

4.6. Question 3 results (lateral LBE structure)

Wetted area and incremental inundation corridor Γ values served as indicators for how LBE spatial structure varied laterally in the study segment. In contrast with the results for question 2, the vast majority, 23 of 28, incremental inundation corridor Γ values were classified in the skimming flow regime, and only 5 were in the wake interference regime. Incremental inundation corridor Γ values always exceeded wetted area Γ values for the same domain. As described in section 4.2 this meant that on a per-area basis more LBEs were located along channel margins than in the baseflow and representative bankfull channels (Table 3). Within the same domain, changes in incremental inundation corridor Γ values were variable, at times increasing (Segment and Reaches 1, 3, and 5), decreasing (Reach 4), or fluctuating (Reaches 2 and 6) as discharge increased. Together, these results indicate LBE spatial structure varied laterally, thus providing differential discharge-dependent roughness in the study segment.

5. Discussion

5.1. Mapping LBEs in a mountain river

The study's semi-automated mapping procedure facilitated a systematic census of LBEs within a 13.2-km mountain river. Using open-source software and operations that could be implemented in any GIS, the procedure is transferable across rivers with the caveat that parameterization will likely be site-dependent. Accurate mapping of LBEs from ALS data is valuable as these systems are capable of covering broader spatial ranges than other topographic-based remote sensing methods (Tomsett and Leyland, 2019). Compared to imagery-based methods, mapping LBEs from 3D point cloud data also had the benefit of retaining heights that LBEs protruded above a smoothed bed, which could be useful for ecological, hydraulic, and hazard analysis (Brasington et al., 2012). The mapping procedure also allows for mapping of LWM or other sources of macroroughness, as inclusion of such features is only constrained by topographic data resolution and algorithm parameters. The study's 0.46 m DTM resolution and the site's lack of LWM likely precluded extensive mapping of LWM as LBEs. However, given adequate data resolution, parameters could be tuned to map a ranged of desired roughness features captured by the unique RSM generation process.

The finding that all tested LBE extraction approaches performed well, based on most LBE_p datasets exceeding PA and MJI benchmarks for matching tree-crowns, is motivating given all approaches were parametrically simple and computationally efficient at the segment scale. Still, some approaches outperformed others as demonstrated by the range of PA scores (0.416-0.901). Importantly, high PA values alone may be misleading, as simply mapping more LBEs results in higher PA scores. For example, several LBE_p datasets with high PA scores had relatively low MJI and MER scores, justifying the need for multiple performance metrics (Table

S12). Further cross-comparison of findings was constrained by absence of studies reporting performance metrics for LBE mapping. However, aspects of mapping performance were still interrogated and found the primary factors controlling mapping performance were: (i) parameter selection for smoothed DTM creation; (ii) approach for LBE extraction; and (iii) extraction algorithm parameterization.

Establishing physical and/or consistent data-driven methods for setting ground classification parameters as part of RSM generation is relevant for transferability of the LBE mapping procedure. As described in section 3.3.1, four physically based length scales informed the range of several key parameters tested and found D_{50} was best for parameterizing the algorithm's spike and offset parameters, and $\sim 2 \cdot D_{50}$ was best for the down spike parameter. These parameters can roughly be thought of in terms of controlling which grains should be included in the RSM and which should be removed. The outcome of this study was that grains $\sim D_{50}$ in height were retained in the RSM, and those larger were removed. This common sedimentological length scale provides a physical basis for parameter selection but further applications are required to evaluate its transferability or universality for smoothed DTM creation in other systems.

Approaches for LBE extraction varied in terms of mapping accuracy and ease of implementation. Performance metrics and heuristic assessment found approach (iv), MCWS with a variable window size, produced the best set of predicted LBEs. Generally, MCWS approaches (iii-v) outperformed vertical threshold approaches (i-ii) for mapping LBEs or similar landscape features, however, mapping performance typically varied more within-approaches having different parameters than between approaches having similar parameters (sections 3.3.2 and 4.1; Text S3.3.2).

Similar to the smoothed DTM creation process, consistent methods for parametrizing feature extraction algorithms aid transferability of the LBE mapping procedure. Data-driven parameter calculations in this study were simple to implement in any GIS, only requiring a RSM and a small set (10^2-10^3) of observed LBEs. Observed LBEs could be digitized from imagery sources or field surveyed if necessary. Since MCWS approaches performed best, discussion is limited to methods for scaling the approach's minimum marker and minimum crown RSM height input parameter values (see section 4.1 and Text S3.3 for details). Calculated minimum RSM values for a pixel to be considered a marker for the top five performing MCWS approaches scaled between ~2.4-3.3·D_{50} (0.312-0.423 m). Holding other parameters constant, there was little difference in global performance metric scores for this range of values, suggesting, sensitivity to this parameter was low. In the sense this parameter controls the minimum height defining roughness elements it bears resemblance to Nikuradse's (1933) equivalent sand-grain roughness, k_s, which is typically related to characteristic grain sizes through various scaling relationships. The k_s parameter is ubiquitous in hydraulic resistance equations and is often scaled by multiplying D_{50} by a factor greater than unity based on understanding that the largest particles present dominate flow resistance (e.g. Powell, 2014). Marker RSM values in this study fall within the broad range of k_s scaling relationships, but are lower than what has been recommended for coarse-bedded rivers (e.g., 5-7·D_{50}) (Weichert, 2006; Powell, 2014). RSM values do not have a 1:1 correspondence with grain sizes as the former represents topographic offsets from a variable but smooth bed surface, which could account for why the minimum RSM value range was smaller than typical D_{50} scaling of k_s values. The smaller D_{50} scaling for minimum RSM values may simply serve to retain a range of smaller LBEs in the mapping procedure than what is considered in resistance equations with larger k_s values. Estimates of the minimum RSM for pixels to be included in the segmentation process, essentially a control on the lateral extent of LBE mapping, for the top five performing MCWS approaches scaled between ~1.5-2.1·D_{50} (0.192-0.272 m). These values were between ~0.61-0.87·minimum RSM values. Mapping performance was more sensitive to this parameter, and higher values had better global performance metric scores. These improvements diminished when values were above ~1.3·D_{50} (0.169 m) (Tables S4 Table S12). Further applications are required to evaluate the robustness of these scaling ranges for MCWS based LBE mapping in other systems.

Beyond performance metrics, visualization noted differences in each approach's ability to distinguish individual LBEs versus aggregate features (i.e., over- and under-segmentation). Vertical threshold approaches appeared less capable of segmenting abutting LBEs, whereas MCWS methods performed better in this regard, as segmentation was an implicit part of the extraction algorithm. Depending on one's goals, some amount of LBE under-segmentation may be acceptable. For instance, mapping particle clusters and/or coarse bedforms such as channel steps are of interest in many studies (Hassan and Reid, 1990; Wittenberg and Newson, 2005). Alternately, over-segmentation can serve to differentiate complex LBE forms into discrete sections, provided each section has a peak identifiable by the marker algorithm. This could be applied toward the study of LBE granular structures, the differential sculpting of complex bedrock features, and/or allow classification of different cluster types, as a few examples.

5.2. LBE lateral spatial structure and resistance

Analyzing LBE spatial structure metrics made it possible to gain insight into LBE organization in the study site at multiple spatial scales. A notable pattern that emerged from quantifying Γ within wetted areas and incremental inundation corridors of discharges ranging from baseflow (1.54 m^3/s) to a 3.5-yr flood event (343.6 m^3/s) was that on a per-area basis more

LBEs were located along channel margins than in the baseflow and representative bankfull channels (Table 3). This was true for the segment as a whole and within each reach, confirming it was neither scale-dependent nor only a localized phenomenon.

One explanation for higher Γ along channel margins is preferential deposition of hillslope derived LBEs in these areas rather than in the bankfull channel portion of the valley bottom. Benda (1990) made this observation in the Oregon Coast Range where boulders from debris flows were deposited before the flow front, thus leaving various disconnected fans, levees, and/or terraces above channel bottoms. Depositional patterns (e.g. size, shape, and location) of wasting events are influenced by sedimentological and morphological hillslope properties and often differentiate by movement type (Hungr et al., 2001). For instance, pre-frontal boulder deposition is common among debris floods and rock avalanches, whereas coarse materials tend to be present at the front of landslides and debris flow deposits (Hungr et al., 2001; Hewitt, 2002). The site's high potential for mass wasting processes (Curtis et al., 2005), provide abundant possibilities to supply LBEs to the study site's valley-bottom. However, the degree to which various modes of wasting and associated depositional mechanics are responsible for observed lateral Γ patterns remain unclear, and theory suggests fluvial transport among other factors play a role. For example, mass movements are often conceptualized as being randomly located along rivers (e.g. Ouimet et al., 2007), which contrasts with the distinct sequences of high- and low-density LBE clusters in the baseflow and bankfull channels (Figure 10) and more diffuse and uniformly distributed LBEs along high flow channel margins (Table 3). Redistribution of channel margin LBEs to more uniformly paved configurations during historic high magnitude discharges offers one plausible explanation. The fact that LBEs were comprised of boulders, boulder clusters, and bedrock outcrops could mean Γ differences were simply due to the presence of exposed bedrock surfaces along channel margins. Weathering and attrition leading to more rapid breakdown of baseflow and bankfull channel LBEs could also account for a portion of lateral Γ differences (Attal, 2017).

While Γ values were highest along margins it is relevant to reiterate that baseflow and bankfull channel Γ values were still relatively high, often at levels conceptualized to maximize flow resistance, thus necessitating supply of LBEs to these portions of the valley bottom as well. Tight hillslope-channel coupling theoretically supports deposition of hillslope derived materials in the bankfull channel (Whiting and Bradley, 1993). Conceptually, channel margins could act as interim storage locations for LBEs to enter the channel through destabilization processes occurring during infrequent high magnitude discharges (Golly et al., 2019). This is one of many fluvial-hillslope feedbacks known to modulate LBE delivery and depositional processes (Shobe et al., 2016). In addition to destabilizing channel margins, infrequent high magnitude discharges also promote disturbance and transport of bankfull channel LBEs and coarse-bedforms, which are thought to re-organize during smaller more frequent flood events, often achieving oscillatory or semi-oscillatory patterns similar to those observed in the study sites baseflow and bankfull channels (Grant et al., 1990). The study site's largest recorded flood occurred in 1997 at a magnitude of 2165.6 m^3/s. It is assumed this ~34-yr flood was capable of mobilizing LBEs several meters in size but the geomorphic work performed relative to the above processes and detangling relative roles of hillslope and fluvial processes driving lateral Γ differences require additional study.

Regardless of explanatory factors, the nested Γ sequence along the study site's river corridor confirmed LBE spatial structure did vary laterally and provides the means for differential roughness as an increasing density of macroroughness features are encountered as discharges increase. This structuring has potential implications toward the commonly held convention that average resistance decreases as discharge increases, as is the case in lower gradient channels with well-defined banks and less abundant LBEs (Powell, 2014). In confined river canyons with abundant LBEs that lack a clear bankfull channel, the discharge-resistance relation response may differ from convention depending on relative contributions of resistance from LBEs versus changing hydraulic conditions (Bathurst, 1978; Pagliara et al., 2008). Hypothetically, if resistance borne by LBEs in incremental inundation corridors increases faster than the amount lost from increasing width-to-depth ratios and mid-channel LBEs becoming highly submerged (i.e. flow depth to D_c ratio ~10 [e.g. Weichert, 2006]) and no longer contributing much resistance it is possible for spatially averaged resistance to increase, remain constant, or only minimally decrease up to a point these relationships no longer hold (Abu-Aly et al., 2014; Cassan et al., 2017). In the study site, the latter condition would certainly occur when the river canyon is inundated and LBEs submerge faster than new LBEs are encountered. Ferguson et al. (2019) found a similar scenario in a relatively smooth, trapezoidal, bedrock channel where resistance initially increased with discharge due to increased sidewall roughness, before subsequently decreasing. Notably, increased LBE submergence in the study site's baseflow and bankfull channels at higher discharges would result in substantial resistance heterogeneity along channel cross-sections, potentially necessitating variable roughness length scales along different portions of the channel margins such as proposed by Ferguson et al. (2019).

5.3. Segment and reach resistance maximization

The question of whether LBEs were configured to maximize flow resistance was answered using LBE concentrations (Γ) and LBE-to-LBE spacing (λ_*^l) metrics at multiple spatial scales. At segment and reach scales, 25 of 28 wetted area Γ values corresponded to Morris's (1959) wake interference regime which served as a hydrodynamic process-based mechanism for maximizing resistance. On the other hand, based on percentages of classified $\widehat{\lambda_*^l}$ values no discharge-dependent segment or reach scale domains corresponded to the wake interference regime (Table 4). Between metrics, there is reason to accept Γ is more reliable for this analysis (section 4.5), therefore the remainder of this section focuses on that metric with the understanding that $\widehat{\lambda_*^l}$ results contribute uncertainty to the supposition that LBEs were configured to maximize resistance. Interestingly, segment- and reach-scale Γ results did not document any cases of isolated roughness.

The three Γ values not classified in the wake interference regime had concentrations of 0.31, 0.33, and 0.304, respectively (Table 3). These are just outside the regime's specified range (0.08-0.30) but are within a broader range of values reported in the literature that may still serve to maximize resistance. For example, in 394 runs in a flume with three macroroughness element configurations (random, transverse stripe, and longitudinal strip), Canovaro et al. (2007) found flow resistance was maximized at macroroughness concentration of ~30 %. Similarly, Pagliara et al. (2008) found friction factor increased for macroroughness concentrations up to ~30 %, the maximum concentration of their 197 experimental runs in a fixed-bed flume with randomly patterned elements. Powell (2014) reviewed multiple studies, including those above, and reported resistance was maximized at macroroughness concentrations between 20 and 40 %. Other experiments, such as those by Nowell and Church (1979) who found resistance maximized at a macroroughness density of 8.3 %, support the possibility of resistance maximizing at lower concentrations. The range of Γ corresponding to maximum resistance in these studies contributes uncertainty to the study's simplifying assumption that the wake interference regime always corresponds to maximum resistance. However, in the absence of unifying Γ-resistance relations, the interpretation remains that discharge-dependent LBEs in the study segment and most reaches were configured to maximize or nearly maximize resistance.

Notably, omission and commission errors and over- and under-segmentation in the final LBE dataset would affect Γ and $\widehat{\lambda_*^l}$ values and associated regime classifications. Regarding Γ, omissions would result in underestimation effects that could be partly balanced by commission errors, whereas over- and under-segmentation wouldn't effect this metric. Assuming a 25 % maximum omission rate (i.e. 25 % increase in Γ), which is reasonable according to PA performance (Table 2), 5 of the 25 segment- and reach-scale Γ values in the wake interference regime would switch to the skimming flow regime. However, all baseflow domains would remain in the wake interference regime and most Γ values would remain below 0.4. For $\widehat{\lambda_*^l}$, omissions would also generate underestimation effects, while commission and over- and under segmentation could have opposite effects due to creating more closely abutting LBEs.

Comparative Γ measurements from other mountain rivers are somewhat lacking, but a few are available in the scientific literature. Resop et al. (2012) mapped 31.8 % areal cover of boulders (>0.256 mm diameter) within a 2nd order, cobble-boulder forested Appalachian mountain stream. Boulder (>0.5 m) concentrations reported by Nitsche et al. (2011) for 14 steep mountainous reaches in the European Alps were between 0 and 40 %. Other reporting posits that large particles generally occupy 2-50 % of the bed area in coarse-bedded rivers (Wittenberg and Newson, 2005). Outside natural rivers, the mobile-bed flume experiments of Church et al. (1998) and Hassan and Church (2000) found reticulate structures of "stone cells" to occupy 10-25 % of final stable bed configurations. These experiments were conducted both with and with-out sediment feed under various flow conditions, typically in the range producing partial transport.

Eaton et al. (2020) proposed a morphologic stability criteria for laterally confined gravel-bed streams of immobile grains occupying 20 % of the areal proportion of the bed. Together, these findings provide some support that macroroughness features in mountain rivers occur within the wake interference regime. Still, inconsistencies in how LBE/macroroughness features are classified and quantified, the complexity of processes involved in how LBEs are supplied to and stored in channels, potential Γ dependencies with other morphometric properties, the need to potentially account for other sources of roughness (e.g. spill and vegetative roughness), and the continuously evolving nature of LBE distributions mean more study is needed to understand the wake interference regime as an attractor state for maximizing resistance toward which natural channels evolve (Molnar et al., 2010). Further, the idea that LBEs organize to maximize resistance fundamentally requires both an active supply of LBEs in the landscape, which itself depends on several factors including but not limited to regional lithology, climate, vegetation, tectonics, and age of the landscape (Attal, 2017; Neely and Dibase, 2020); and a river style where roughness is the primary mode of channel adjustment, which is only true for certain river styles (Brierley and Fryirs, 2005; Fryirs et al., 2016). Notably, both these limiting conditions are present in the study site.

Previous findings documenting positive relationships between channel slope and Γ are a good example of the dependency that Γ may have on other morphometric properties described above (Grant and Swanson, 1995; Nitsche et al., 2012). Recent study on this topic posits a negative autogenic feedback exists between Γ, channel slope, and hillslope processes such that following a change in base level, river incision acts to steepen adjacent hillslopes, thereby increasing LBE delivery to channels (Shobe et al., 2016). The physical protection and resistance provided by LBEs mediate further channel incision, ultimately allowing for occurrence of overly steep channel slopes compared to equilibrium profiles expected by landscape evolution modeling theory. Like the works cited above, results from this study also found positive relationships between reach-averaged slope and Γ (Figure 14). More detailed analysis of the relationship between LBEs and morphometric properties, such as slope, is enticing but beyond the scope of this effort.

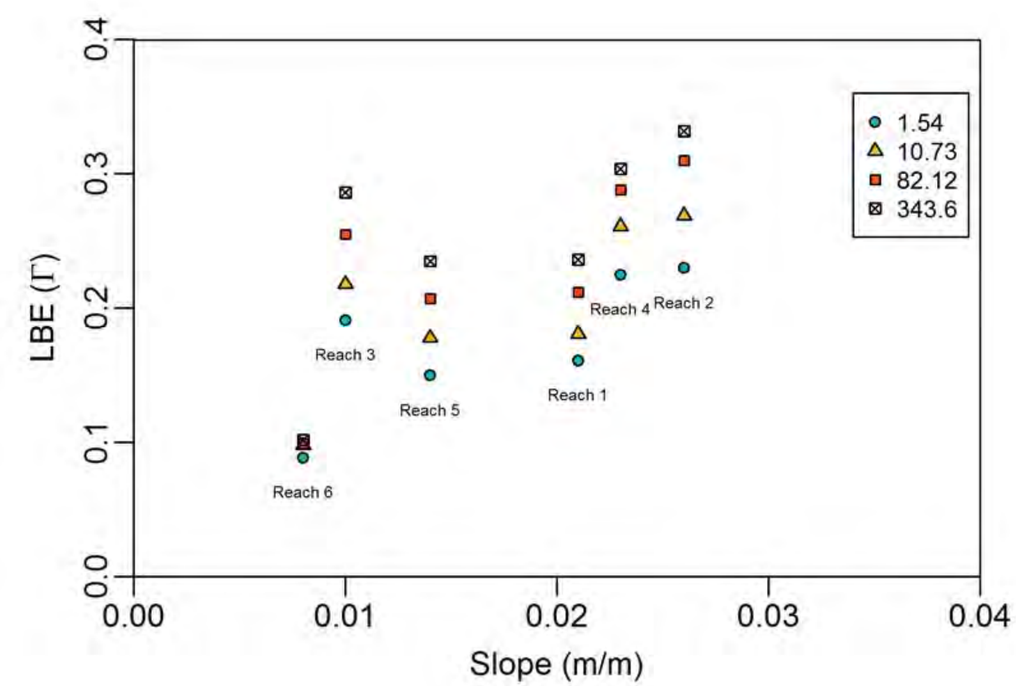

Figure 14. Reach scale large bed element (LBE) concentration (Γ) versus reach averaged slope for each discharge-dependent LBE dataset. Discharges in legend are in m^3/s.

5.4. Cross-section resistance maximization

Unlike previous efforts aggregating Γ at larger spatial scales (Nitsche et al., 2011), this study included both Γ and $\overline{\lambda_*^l}$ calculations at river cross-sections (10^{-1} width). This granularity highlighted spatial variability of Γ and $\overline{\lambda_*^l}$, and associated Morris regimes, in the study site. For $\overline{\lambda_*^l}$, this is also the first time we aware of this type of LBE spacing metric being calculated in a natural setting at any scale. In many mountain rivers the expectation that all cross-sections would conform to a single hydrodynamic regime such as the wake interference regime is unrealistic. This type of uniform, plane-bed channel morphology contrasts with both the diversity of river styles present in mountainous regions as well as the tendency for bedform development (Grant et al., 1990; Brierley and Fryirs, 2005). This divergence was exemplified by the oscillatory nature of the study site's Γ and $\overline{\lambda}_*^l$ profiles (Figure 10; Figure 11), which includes definitive bedforms (Wiener and Pasternack, 2019). Nevertheless, the tendency for oscillations to be centered about the wake interference regime supports the notion that portions of the channel must be attracted to this state, which is compatible with theory for regular to semi-regular coarse bedforms patterns to maximize resistance and promote channel stability (Abrahams et al., 1995; Madej, 2001). In this regard there may be interest to use Γ and/or $\overline{\lambda}_*^l$ as more basic units of geomorphic analysis in addition to or in lieu of more traditional metrics involving channel unit classification (Grant et al., 1990; Adams, 2020).

Discrepancies in cross-sectional Γ and $\overline{\lambda}_*^l$ based regime classifications highlighted potential uncertainties in thresholds used to classify regimes and potential issues using $\overline{\lambda}_*^l$ for classifying Morris's hydrodynamic regimes in natural rivers. While Γ was taken as a more reliable metric for the purposes of this study, spacing metrics like $\overline{\lambda}_*^l$ and $\widehat{\lambda}_*^l$ still have utility in describing hydraulic properties in natural channels as they correspond with flow disruption and recovery length scales (Bathurst, 1978; Tan and Curran, 2012). Spacing metrics can also be used to address open questions of whether clustering mechanisms dominate over dispersive mechanisms in the longitudinal spacing of LBEs in mountain rivers (Madej, 2001). Taken together, the study's concentration and spacing metrics form scale-dependent phase-spaces providing more complete representations of a river channel's LBE spatial structure (Figure S15).

For instance, if a river has Γ in the wake-interference regime and $\overline{\lambda_*^l}$ in the skimming regime, as was often the case for baseflow conditions in the study site, this suggests individual LBEs are present in closely spaced clusters (i.e., low $\overline{\lambda_*^l}$), but that the clusters are widely spaced (i.e., relatively low Γ). Visualizing discharge-dependent metric trajectories on phase-spaces can aid in describing how LBE spatial structure and resistance change as different portions of the river corridor become inundated. Lastly, it is reasonable to posit that data plotting in discrete regions of a Γ-λ phase-space could discriminate different channel morphologies and/or where different modes of channel adjustment such as planform, gradient, or bed roughness would likely dominate (Eaton and Church, 2009).

5.5. Resistance maximization as an attractor state

Results of the study found LBEs in the study segment and several other mountain rivers were often present in spatial configurations associated with maximizing flow resistance. However, findings do not address the question of how and why channels might adjust toward a state of maximum flow resistance. The why of this question remains part of a set of open questions on landscape evolution and fluvial morphodynamics that are outside the scope of the effort. However, acceptance of the extremal/regime theory hypothesis that channels adjust their boundaries to maximize flow resistance provides a limited answer, even if the validity of this hypothesis remains open (Eaton and Church, 2009).

How LBE configurations might evolve to maximize flow resistance can be explored through conceptual trajectories of landscape adjustment under the assumption that channels adjustment their boundary conditions to increase hydraulic resistance when resistance is low relative to hydraulic forces and visa-versa. Firstly, if LBEs are present in configurations above those associated with maximum flow resistance high LBE densities covering the channel bed would reduce incision (Sklar and Dietrich, 2004; Shobe et al., 2016). This would be expected to reduce hillslope LBE supply through reduced upslope propagation of hillslope steepening and increased hillslope stability (Attal et al., 2015; Shobe et al., 2016). During periods of reduced supply, other factors such as attrition, weathering, and transport could serve to reduce LBE configurations. Where LBE supply remains high, a cyclical feedback of resistance induced deposition creating more planar beds and thus more transportable LBEs could develop LBE configurations that oscillate between maximize resistance and those exceeding this condition (i.e., skimming flow) (Wohl and Merritt, 2008; Eaton et al., 2020).

Alternately, LBE configurations lower than those that maximize flow resistance can drive feedbacks increasing LBE supply, deposition, or other adjustments that increase resistance. For instance, with less LBE cover incision processes would increase leading to greater hillslope LBE supply (Shobe et al., 2016). Lower resistance also means channels are less stable during floods, which can lead to hillslope destabilization that increases LBE supply, and increased LBE transport (Wohl and Merritt, 2008; Ferguson et al., 2019; Golly et al., 2019). The latter may be counterintuitive, but can promote bedform development through jamming type interactions and/or armor development that can then increase resistance through exhumation, increased deposition, and/or reduced transport of LBEs supplied by hillslopes (Wohl and Merritt, 2008). Though simplified, these feedbacks provide reasonable trajectories of LBE mediated channel adjustment toward conditions of maximum resistance while leaving room for more complex oscillations and non-equilibrium behavior.

6. Conclusions

In a recent commentary on the importance of larger-than-average particles, Williams et al. (2019) stated the need to, “appraise the presence, sources, distribution and role of large grain deposits in contemporary riverscapes.” In this study we present and use a semi-automated procedure to systematically map LBEs at the segment scale within a mountain river from 3D point-cloud data. The suite of performance metrics employed found application of a MCWS algorithm to return the best LBE prediction results among tested methods, with performance comparable to efforts from the field of forestry for mapping tree-crowns. To allow transferability of the procedure, effort was taken to rely on physical or data-driven techniques for parameter selection. The study site’s D_{50} served as a reference scale for mapping algorithm parameters, but further application is required to understand the universality or range of appropriate scaling factors. Ultimately, given the availability of a 3D point cloud, reasonable LBE mapping was proven to be easily implementable across a variety of spatial scales. This could prove valuable toward improving sediment transport predictions (Yager et al., 2007) and habitat characterizations (Gippel et al., 1996) in mountain rivers where accurate accounting of LBEs is critical (Piégay et al., 2020).

Following mapping, novel exploration of LBE spatial structure was conducted using LBE concentrations and streamwise LBE-to-LBE spacing metrics for multiple laterally and/or hierarchically nested spatial domains at multiple spatial scales. Greater LBEs concentrations along channel margins compared to baseflow and representative bankfull channels provided the foundation for an untested conceptualization for spatially averaged resistance to increase, remain constant, or only minimally decrease with discharge, which differs from current conventional understanding. Segment- and reach-scale LBE configurations supported the hypothesis that

LBEs were often organized to maximize flow resistance on the basis of the hydrodynamic flow regimes originally proposed by Morris (1959), however conflicting results, uncertainty in regime thresholds and the assumption that the wake interference regime always corresponds to maximum resistance, and uncertainty regarding the relative role of fluvial versus other geomorphic mechanisms driving LBE organization leave open questions about this extremal model of geomorphic adjustment. Analysis of river cross-sections demonstrated the spatial variability of LBE configurations, but findings also served to reinforce that the wake interference regime may act as an attractor state toward which conditions converge but from which there is freedom to deviate in response to dynamic forces shaping the LBE landscape (Phillips, 1999). Further study of LBEs in other mountain rivers at multiple spatial scales is required to better understand the regularity and mechanisms by which LBEs are structured to maximize resistance and variability around the wake interference regime. Nevertheless, the fact that LBEs were often configured to maximize resistance as well as documenting differential patterns in the lateral spatial structure of LBEs in the river corridor may have practical applications for synthetic river design and guiding river management or restoration actions such as designing LBE configurations or having reach scale LBE concentrations in the wake interference regime as a process-based goal.

Acknowledgments

This work is funded by the Yuba Water Agency (Marysville, California, USA; (Award #201503808). This project was also supported by the USDA National Institute of Food and Agriculture, Hatch project number CA-D-LAW-7034-H. We thank Dr. Douglas Thompson, Dr.

Rebecca Hodge and an anonymous reviewer for constructive feedback that greatly improved the quality of this manuscript.

Data availability

Datasets and R code related to this publication are available for download at the following open data repository (https://zenodo.org/record/6506102). Restrictions apply to the availability of the 2014 DTM and 2D model results, which were used under contractual agreement from the project sponsor. These are available from the senior author with the permission of Yuba Water Agency.

Appendix A. Supplementary data

Supplementary data to this article can be found online at https://doi.org/10.1016/j.geomorph.2022.108431.

References

Aberle, J., Smart, G.M., 2003. The influence of roughness structure on flow resistance on steep slopes. Journal of Hydraulic Research, 41(3), 259-269. doi:10.1080/00221680309499971

Abrahams, A.D., Li, G., Atkinson, J.F., 1995. Step-Pool Streams: Adjustment to Maximum Flow Resistance. Water Resources Research, 31(10), 2593-2602. doi:10.1029/95wr01957

Abu-Aly, T.R., Pasternack, G.B., Wyrick, J.R., Barker, R., Massa, D., Johnson, T., 2014. Effects of LiDAR-derived, spatially distributed vegetation roughness on two-dimensional hydraulics in a gravel-cobble river at flows of 0.2 to 20 times bankfull. Geomorphology, 206(Supplement C), 468-482. https://doi.org/10.1016/j.geomorph.2013.10.017

Adams, D. L., 2020. Toward bed state morphodynamics in gravel-bed rivers. Progress in Physical Geography: Earth and Environment, 44(5), 700-726. doi:10.1177/0309133320900924

Attal, M., 2017. Linkage Between Sediment Transport and Supply in Mountain Rivers, in: Tsutumi, D., Laronne, J.B., (Eds.), Gravel-Bed Rivers: Processes and Disasters, Wiley, Chichester, pp. 329–353.

Attal, M., Mudd, S.M., Hurst, M.D., Weinman, B., Yoo, K., Naylor, M., 2015. Impact of change in erosion rate and landscape steepness on hillslope and fluvial sediments grain size in the Feather River basin (Sierra Nevada, California). Earth Surf. Dynam., 3(1), 201-222. doi:10.5194/esurf-3-201-2015

Bathurst, J.C., 1978. Flow resistance of large-scale roughness. J. Hydraul. Div. ASCE 104 (12), 1587–1603. https://doi.org/10.1061/JYCEAJ.0005114

Bathurst, J.C., 1982. Flow resistance in boulder-bed streams, in: Hey, R.D., Bathurst, J.C., Thorne, C.R. (Eds.), Gravel-bed Rivers, Wiley, Chichester, pp. 443–462.

Benda, L., 1990. The influence of debris flows on channels and valley floors in the Oregon Coast Range, U.S.A. Earth Surface Processes and Landforms, 15(5), 457-466. doi:10.1002/esp.3290150508

Brasington, J., Vericat, D., Rychkov, I., 2012. Modeling river bed morphology, roughness, and surface sedimentology using high resolution terrestrial laser scanning. Water Resources Research, 48(11). doi:10.1029/2012wr012223

Brierley, G.J., Fryirs, K.A., 2005. The River Styles Framework. Geomorphology and River Management: Applications of the River Styles Framework. Malden, MA: Blackwell Publishing.

Brown, R.A., Pasternack, G.B., 2014. Hydrologic and topographic variability modulate channel change in mountain rivers. Journal of Hydrology, 510(Supplement C), 551-564. https://doi.org/10.1016/j.jhydrol.2013.12.048

Butler, J.B., Lane, S.N., Chandler, J.H., 2001. Automated extraction of grain-size data from gravel surfaces using digital image processing. Journal of Hydraulic Research, 39(5), 519-529. doi:10.1080/00221686.2001.9628276

Canovaro, F., Paris, E., Solari, L., 2007. Effects of macro-scale bed roughness geometry on flow resistance. Water Resources Research, 43(10). doi:10.1029/2006wr005727

Carbonneau, P.E., Lane, S.N., Bergeron, N.E., 2004. Catchment-scale mapping of surface grain size in gravel bed rivers using airborne digital imagery. Water Resources Research, 40(7). doi:10.1029/2003WR002759

Carey, J.A., Pinter, N., Pickering, A.J., Prentice, C.S., Delong, S.B., 2019. Analysis of Landslide Kinematics Using Multi-temporal Unmanned Aerial Vehicle Imagery, La Honda, California. Environmental and Engineering Geoscience, 25(4), 301-317. doi:10.2113/eeg-2228

Cassan, L., Roux, H., Garambois, P.A., 2017. A Semi-Analytical Model for the Hydraulic Resistance Due to Macro-Roughnesses of Varying Shapes and Densities. Water, 9(9), 637. https://doi.org/10.3390/w9090637

Chen, Q., Baldocchi, D., Gong, P., Kelly, M., 2006. Isolating individual trees in a savanna woodland using small footprint lidar data. Photogrammetric Engineering and Remote Sensing, 72, 923-932. https://doi.org/10.14358/PERS.72.8.923

Chen, Y., DiBiase, R.A., McCarroll, N., Liu, X., 2019. Quantifying flow resistance in mountain streams using computational fluid dynamics modeling over structure-from-motion photogrammetry-derived microtopography. Earth Surface Processes and Landforms, 44(10), 1973-1987. doi:10.1002/esp.4624

Chin, A., Phillips, J.D., 2007. The self-organization of step-pools in mountain streams. Geomorphology, 83(3), 346-358. https://doi.org/10.1016/j.geomorph.2006.02.021

Church, M., Hassan, M.A., Wolcott, J.F., 1998. Stabilizing self-organized structures in gravel-bed stream channels: Field and experimental observations. Water Resources Research, 34(11), 3169-3179. 10.1029/98wr00484

Curtis, J.A., Flint, L.E., Alpers, C.N., Yarnell, S.M., 2005. Conceptual model of sediment processes in the upper Yuba River watershed, Sierra Nevada, CA. Geomorphology, 68(3-4), 149-166. 10.1016/j.geomorph.2004.11.019

Davies, T.R.H., Sutherland, A.J., 1983. Extremal hypotheses for river behavior. Water Resources Research, 19(1), 141-148. 10.1029/WR019i001p00141

Detert, M., Weitbrecht, V., 2012. Automatic object detection to analyze the geometry of gravel grains – a free stand-alone tool. River Flow 2012, Muños, R.M., (Ed.), Taylor and Francis Group, London, ISBN 978-0-415-62129-8, pp. 595-600.

Eaton, B.C., Church, M., 2009. Channel stability in bed load–dominated streams with nonerodible banks: Inferences from experiments in a sinuous flume, J. Geophys. Res., 114, F01024, doi:10.1029/2007JF000902.

Eaton, B.C., MacKenzie, L.G., Booker, W.H., 2020. Channel stability in steep gravel–cobble streams is controlled by the coarse tail of the bed material distribution. Earth Surf. Process. Landforms, 45, 3639– 3652. https://doi.org/10.1002/esp.4994.

Einstein, H.A., Barbarossa, N., 1952. River channel roughness. Trans ASCE 117(1):1121–1132. https://doi.org/10.1061/TACEAT.0006666

Fang, H.W., Liu, Y., Stoesser, T., 2017. Influence of Boulder Concentration on Turbulence and Sediment Transport in Open-Channel Flow Over Submerged Boulders. Journal of Geophysical Research: Earth Surface, 122(12), 2392-2410. doi:10.1002/2017jf004221

Ferguson, R.I., Hardy, R.J., Hodge, R.A., 2019. Flow resistance and hydraulic geometry in bedrock rivers with multiple roughness length scales. Earth Surface Processes and Landforms, 44(12), 2437-2449. doi:10.1002/esp.4673

Ferro, V., 1999. Friction Factor for Gravel-Bed Channel with High Boulder Concentration. Journal of Hydraulic Engineering, 125(7), 771-778. doi:10.1061/(ASCE)0733-9429(1999)125:7(771)

Finnegan, N.J., Broudy, K.N., Nereson, A.L., Roering, J.J., Handwerger, A.L., Bennett, G., 2019. River channel width controls blocking by slow-moving landslides in California's Franciscan mélange. Earth Surf. Dynam., 7(3), 879-894. doi:10.5194/esurf-7-879-2019

Fryirs, K.A., Wheaton, J.M., Brierley, G.J., 2016. An approach for measuring confinement and assessing the influence of valley setting on river forms and processes. Earth Surface Processes and Landforms, 41(5), 701-710. doi:10.1002/esp.3893

Gippel, C.J., O'neill, I.C., Finlayson, B.L., Schnatz, I., 1996. Hydraulic guidelines for the re-inroduction and management of large woody debris in lowland rivers. Regulated Rivers: Research and Management, 12(2-3), 223-236. doi:10.1002/(sici)1099-1646(199603)12:2/3<223::aid-rrr391>3.0.co;2-#

Golly, A., Turowski, J.M., Badoux, A., Hovius, N., 2019. Testing models of step formation against observations of channel steps in a steep mountain stream. Earth Surface Processes and Landforms, 44(7), 1390-1406. doi:10.1002/esp.4582

Gomez, B., 1993. Roughness of stable, armored gravel beds. Water Resources Research, 29(11), 3631-3642. doi:10.1029/93wr01490

Grant, G.E., Swanson, F.J., 1995. Morphology and Processes of Valley Floors in Mountain Streams, Western Cascades, Oregon, in: Costa, E., Miller, A.J., Potter, K.W., Wilcock, P.R. (Eds.), Natural and Anthropogenic Influences in Fluvial Geomorphology, Volume 89, American Geophysical Union, pp. 83–101. https://doi.org/10.1029/GM089p0083

Grant, G.E., Swanson, F.J., Wolman, M.G., 1990. Pattern and origin of stepped-bed morphology in high-gradient streams, Western Cascades, Oregon. GSA Bulletin, 102(3), 340-352. doi:10.1130/0016-7606(1990)102<0340:PAOOSB>2.3.CO;2

Guillon, H., Byrne, C.F., Lane, B.A., Sandoval Solis, S., Pasternack, G.B., 2020. Machine Learning Predicts Reach-Scale Channel Types From Coarse-Scale Geospatial Data in a Large River Basin. Water Resources Research, 56(3), e2019WR026691. doi:10.1029/2019wr026691

Hassan, M.A., Church, M., 2000. Experiments on surface structure and partial sediment transport on a gravel bed. Water Resources Research, 36(7), 1885-1895. doi:10.1029/2000wr900055

Hassan, M.A., Reid, I., 1990. The influence of microform bed roughness elements on flow and sediment transport in gravel bed rivers. Earth Surface Processes and Landforms, 15(8), 739-750. doi:10.1002/esp.3290150807

Hewitt, K., 2002. Styles of rock-avalanche depositional complexes conditioned by very rugged terrain, Karakoram Himalaya, Pakistan, in: Evans, S.G., DeGraff, J.V. (Eds.), Catastrophic landslides: Effects, occurrence, and mechanisms, Geological Society of America Reviews in Engineering Geology, Colorado, v. XV, pp. 345-377.

Hodge, R., Brasington, J., Richards, K., 2009. In situ characterization of grain-scale fluvial morphology using Terrestrial Laser Scanning. Earth Surface Processes and Landforms, 34(7), 954-968. doi:10.1002/esp.1780

Hungr, O., Evans, S.G., Bovis, M.J., Hutchinson, J.N., 2001. A review of the classification of landslides of the flow type. Environmental and Engineering Geoscience; 7 (3), 221–238. https://doi.org/10.2113/gseegeosci.7.3.221

Hurst, M.D., Mudd, S.M., Walcott, R., Attal, M., Yoo, K., 2012. Using hilltop curvature to derive the spatial distribution of erosion rates. Journal of Geophysical Research: Earth Surface, 117(F2). doi:10.1029/2011jf002057

Isenburg, M., 2016. LAStools - efficient LiDAR processing software (version 160730, unlicensed). http://rapidlasso.com/LAStools.

Kaartinen, H., Hyyppä, J., Yu, X., Vastaranta, M., Hyyppä, H., Kukko, A., . . . Wu, J.C., 2012. An International Comparison of Individual Tree Detection and Extraction Using Airborne Laser Scanning. Remote Sensing, 4(4), 950-974. https://doi.org/10.3390/rs4040950

Lai, Y. G., 2008. SRH-2D version 2: Theory and User's Manual Sedimentation and River Hydraulics – Two-Dimensional River Flow Modeling. U.S. Department of the Interior, Bureau of Reclamation, Technical Service Center, Sedimentation and River Hydraulics Group, Colorado. https://www.usbr.gov/tsc/techreferences/computer%20software/models/srh2d/index.html

Legleiter, C.J., Roberts, D.A., Marcus, W.A., Fonstad, M.A., 2004. Passive optical remote sensing of river channel morphology and in-stream habitat; physical basis and feasibility. Remote Sensing of Environment, 93(4), 493-510. http://dx.doi.org/10.1016/j.rse.2004.07.019

Lisle, T.E., Nelson, J.M., Pitlick, J., Madej, M.A., Barkett, B.L., 2000. Variability of bed mobility in natural, gravel-bed channels and adjustments to sediment load at local and reach scales. Water Resources Research, 36(12), 3743-3755. doi:10.1029/2000wr900238

Madej, M.A., 2001. Development of channel organization and roughness following sediment pulses in single-thread, gravel bed rivers. Water Resources Research, 37(8), 2259-2272. doi:10.1029/2001wr000229

Marconi, S., Graves, S.J., Gong, D., Nia, M.S., Le Bras, M., Dorr, B.J., . . . Wang, D.Z., 2019. A data science challenge for converting airborne remote sensing data into ecological information. PeerJ, 6, e5843-e5843. doi:10.7717/peerj.5843

Molnar, P., Densmore, A.L., McArdell, B.W., Turowski, J.M., Burlando, P., 2010. Analysis of changes in the step-pool morphology and channel profile of a steep mountain stream following a large flood. Geomorphology, 124(1), 85-94. https://doi.org/10.1016/j.geomorph.2010.08.014

Morris, H., 1959. Design methods for flow in rough channels. Proc. ASCE, Journal of Hydraulics Division, 85(HY7), 43-62. https://doi.org/10.1061/JYCEAJ.0000324

Neely, A.B., DiBiase, R.A., 2020. Drainage area, bedrock fracture spacing, and weathering controls on landscape-scale patterns in surface sediment grain size. Journal of Geophysical Research: Earth Surface, n/a(n/a), e2020JF005560. doi:10.1029/2020jf005560

Nikuradse, J., 1933. Stromungsgesetz in rauhren rohren, vDI Forschungshefte 361 (English translation: Laws of flow in rough pipes), NACA Technical Memorandum 1292. National Advisory Commission for Aeronautics, Washington, DC, USA. 1950. https://ntrs.nasa.gov/citations/19930093938

Nitsche, M., Rickenmann, D., Kirchner, J.W., Turowski, J.M., Badoux, A., 2012. Macroroughness and variations in reach-averaged flow resistance in steep mountain streams. Water Resources Research, 48(12). doi:10.1029/2012WR012091

Nitsche, M., Rickenmann, D., Turowski, J.M., Badoux, A., Kirchner, J.W., 2011. Evaluation of bedload transport predictions using flow resistance equations to account for macro-roughness in steep mountain streams. Water Resources Research, 47(8). doi:10.1029/2011wr010645

Nowell, A.R.M., Church, M., 1979. Turbulent flow in a depth-limited boundary layer. Journal of Geophysical Research: Oceans, 84(C8), 4816-4824. doi:10.1029/JC084iC08p04816

Ouimet, W.B., Whipple, K.X., Royden, L.H., Sun, Z., Chen, Z., 2007. The influence of large landslides on river incision in a transient landscape: Eastern margin of the Tibetan Plateau (Sichuan, China). GSA Bulletin; 119 (11-12), 1462–1476. https://doi.org/10.1130/B26136.1

Pagliara, S., Das, R., Carnacina, I., 2008. Flow resistance in large-scale roughness condition. Canadian Journal of Civil Engineering, 35(11), 1285-1293. doi:10.1139/L08-068

Papanicolaou, A.N., Diplas, P., Dancey, C.L., Balakrishnan, M., 2001. Surface Roughness Effects in Near-Bed Turbulence: Implications to Sediment Entrainment. Journal of Engineering Mechanics, 127(3), 211-218. doi:10.1061/(ASCE)0733-9399(2001)127:3(211)

Papanicolaou, A.N., Tsakiris, A.G., 2017. Boulder Effects on Turbulence and Bedload Transport in: Tsutumi, D., Laronne, J.B., (Eds.), Gravel-Bed Rivers: Processes and Disasters, Wiley, Chichester, pp. 33–72.

Pasternack, G.B., Senter, A.E., 2011. 21st Century instream flow assessment framework for mountain streams. California Energy Commission, PIER. CEC-500-2013-059. https://www.energy.ca.gov/2013publications/CEC-500-2013-059/CEC-500-2013-059.pdf

Pasternack, G.B., Ellis, C.R., Leier, K.A., Vallé, B.L., Marr, J.D., 2006. Convergent hydraulics at horseshoe steps in bedrock rivers. Geomorphology, 82(1), 126-145. https://doi.org/10.1016/j.geomorph.2005.08.022

Pearson, E., Smith, M.W., Klaar, M.J., Brown, L.E., 2017. Can high resolution 3D topographic surveys provide reliable grain size estimates in gravel bed rivers? Geomorphology, 293, 143-155. https://doi.org/10.1016/j.geomorph.2017.05.015

Phillips, J.D., 1999. Divergence, Convergence, and Self-Organization in Landscapes. Annals of the Association of American Geographers, 89(3), 466-488. doi:10.1111/0004-5608.00158

Piégay, H., Arnaud, F., Belletti, B., Bertrand, M., Bizzi, S., Carbonneau, P., . . . Slater, L., 2020. Remotely sensed rivers in the Anthropocene: state of the art and prospects. Earth Surface Processes and Landforms, 45(1), 157-188. doi:10.1002/esp.4787

Popescu, S.C., Wynne, R.H., 2004. Seeing the Trees in the Forest. Photogrammetric Engineering and Remote Sensing, 70(5), 589-604. doi:10.14358/PERS.70.5.589

Powell, D.M., 2014. Flow resistance in gravel-bed rivers: Progress in research. Earth-Science Reviews, 136, 301-338. https://doi.org/10.1016/j.earscirev.2014.06.001

Purinton, B., Bookhagen, B., 2019. Introducing PebbleCounts: a grain-sizing tool for photo surveys of dynamic gravel-bed rivers. Earth Surf. Dynam., 7(3), 859-877. doi:10.5194/esurf-7-859-2019

Resop, J.P., Kozarek, J.L., Hession, W.C., 2012. Terrestrial Laser Scanning for Delineating In-stream Boulders and Quantifying Habitat Complexity Measures. Photogrammetric Engineering and Remote Sensing, 78(4), 363-371.

Schneider, J.M., Rickenmann, D., Turowski, J.M., Kirchner, J.W., 2015. Self-adjustment of stream bed roughness and flow velocity in a steep mountain channel. Water Resources Research, 51(10), 7838-7859. doi:10.1002/2015wr016934

Shao, G., Tang, L., Liao, J., 2019. Overselling overall map accuracy misinforms about research reliability. Landscape Ecology, 34(11), 2487-2492. doi:10.1007/s10980-019-00916-6

Shobe, C.M., Tucker, G.E., Anderson, R.S., 2016. Hillslope-derived blocks retard river incision. Geophysical Research Letters, 43(10), 5070-5078. doi:10.1002/2016gl069262

Sklar, L.S., Dietrich, W.E., 2004. A mechanistic model for river incision into bedrock by saltating bed load. Water Resources Research, 40(6). doi:10.1029/2003wr002496

Strom, M.A., Pasternack, G.B., Wyrick, J.R., 2016. Reenvisioning velocity reversal as a diversity of hydraulic patch behaviours. Hydrological Processes, 30(13), 2348-2365. doi:10.1002/hyp.10797

Tan, L., Curran, J.C., 2012. Comparison of Turbulent Flows over Clusters of Varying Density. Journal of Hydraulic Engineering, 138(12), 1031-1044. doi:10.1061/(ASCE)HY.1943-7900.0000635

Tomsett, C., Leyland, J., 2019. Remote sensing of river corridors: A review of current trends and future directions. River Research and Applications, 35(7), 779-803. doi:10.1002/rra.3479

Vallé, B., Pasternack, G.B., 2006. Field mapping and digital elevation modelling of submerged and unsubmerged hydraulic jump regions in a bedrock step-pool channel. Earth Surface Processes and Landforms, 31(6), 646-664. https://doi.org/10.1002/esp.1293

Warrick, J.A., Rubin, D.M., Ruggiero, P., Harney, J.N., Draut, A.E., Buscombe, D., 2009. Cobble cam: grain-size measurements of sand to boulder from digital photographs and autocorrelation analyses. Earth Surface Processes and Landforms, 34(13), 1811-1821. doi:10.1002/esp.1877

Weichert, R., 2006. Bed Morphology and Stability of Steep Open Channels. In Mitteilung 192, Zürich: Versuchsanstalt fürWasserbau, Hydrologie und Glaziologie (VAW), ETH. https://doi.org/10.3929/ethz-a-005135522

Wentworth, C., 1922. A Scale of Grade and Class Terms for Clastic Sediments. The Journal of Geology, 30(5), 377-392. http://www.jstor.org/stable/30063207

Whiting, P.J., Bradley, J.B., 1993. A process-based classification system for headwater streams. Earth Surface Processes and Landforms, 18(7), 603-612. doi:10.1002/esp.3290180704

Wiener, J., Pasternack, G.B., 2016a. Accretionary Flow Analysis- Yuba River from New Bullards Bar to Colgate Powerhouse. Prepared for Yuba County Water Agency. University of California, Davis, CA. http://pasternack.ucdavis.edu/research/projects/ncrs/mountain-river-eco-geo

Wiener, J., Pasternack, G.B., 2016b. 2014 Topographic Mapping Report- Yuba River from New Bullards Bar to Colgate Powerhouse. Prepared for Yuba County Water Agency. University of California, Davis, CA. http://pasternack.ucdavis.edu/research/projects/ncrs/mountain-river-eco-geo

Wiener, J.S., Pasternack, G.B., 2019. Diversity and organization of mountain river morphological units challenge conceptions of riffle-pool, step-pool, and cascade channel types. Abstract EP51E-2129 presented at 2019 Fall Meeting, AGU, San Francisco, CA, 9-13 Dec.

Williams, R.D., Reid, H.E., Brierley, G.J., 2019. Stuck at the Bar: Larger-Than-Average Grain Lag Deposits and the Spectrum of Particle Mobility. Journal of Geophysical Research: Earth Surface, 124(12), 2751-2756. doi:10.1029/2019jf005137

Wittenberg, L., Newson, M.D., 2005. Particle clusters in gravel-bed rivers: an experimental morphological approach to bed material transport and stability concepts. Earth Surface Processes and Landforms, 30(11), 1351-1368. doi:10.1002/esp.1184

Wohl, E., Merritt, D., 2008. Reach-scale channel geometry of mountain streams. Geomorphology, 93(3-4), 168-185. https://doi.org/10.1016/j.geomorph.2007.02.014

Yager, E.M., Kirchner, J.W., Dietrich, W.E., 2007. Calculating bed load transport in steep boulder bed channels. Water Resources Research, 43(7). doi:10.1029/2006wr005432

Yuba County Water Agency (YCWA), 2013. Technncal Memorandum 1-1. Channel Morphology Upstream of Englebright Reservoir. Yuba River Development Project FERC Project No. 2246. http://www.ycwa-relicensing.com/Technical%20Memoranda/Forms/AllItems.aspx

Zhang, K., Whitman, D., 2005. Comparison of Three Algorithms for Filtering Airborne Lidar Data. Photogrammetric Engineering and Remote Sensing, 71(3), 313-324. doi:10.14358/PERS.71.3.313

Supporting Information for
Scale dependent spatial structuring of mountain river large bed elements maximizes flow resistance

J.S. Wiener and G. B. Pasternack

Contents of this file

Text S1 to S6

Figures S1 to S13

Tables S1 to S13

This document provide supplemental materials that include information on the following topics:

- Details on topographic and bathymetric data collection, processing, and mapping (3.1);
- Details of large bed element (LBE) mapping procedure including performance metrics, extraction algorithms, post-extraction filtering, and geometric assessment (3.3);
- Details of two-dimensional hydrodynamic modeling including model selection, parametrization and calibration, model validation, and model sensitivity to roughness parameterization (3.4);
- Details of LBE spatial analysis including cross-section polygon creation and path-based approach for streamwise spacing calculations (3.5)
- Additional LBE mapping results (4.1);
- Additional LBE spacing analysis results (4.3);
- Additional hydrodynamic regime comparison analysis results and discussion (4.4 and 5.4); and
- References

The organization of this document uses the same outline and headings of the study to which this supplements. Subject headings followed by the word “none” indicate no supplemental information is provided for that section.

1. Introduction

Table S1. Summary of LBE influences on river channels and landscapes.

Topic	Summary	Selected references
Hydraulics and hydrodynamics	LBEs are a primary source of flow resistance in mountain rivers. Locally, LBEs generate complex wake and vortex structures that cause deviations from idealized logarithmic vertical velocity profiles. Collectively, LBEs act to influence flow patterns and the spatial distribution of hydraulic properties (depth, velocity, bed shear stress) that govern other fluvial processes such as sediment transport.	Morris, 1959; Bathurst, 1978, 1985, 1987; Gomez, 1993; Gippel et al., 1996; Baiamonte and Ferro, 1997; Ferro, 1999; Byrd et al., 2000; Lamarre and Roy, 2005; Canovaro et al., 2007; Lacey and Roy, 2008; Pagliara et al., 2008; Hardy et al., 2009; Schneider et al., 2015a, 2015b; Fang et al., 2017; Ferguson et al., 2017; Monsalve et al., 2017; Groom and Friedich, 2019
Sediment transport and retention dynamics	LBEs influence localized patterns of erosion and deposition. This in-turn effects the granular structure of the bed and the formation, stability, and sedimentological characteristics of sediment patches. The presence of LBEs can enhance bed stability through interlocking, imbrication, and hiding effects that therein influence the entrainment and transport of adjacent grains and patches. By extracting energy from the flow in the form of resistance and stabilizing the bed LBEs regulate the storage and export of sediments. So called LBE 'sticky spots' can even provide potential for long term storage (1000's of years) which contrasts with traditional views of mountain rivers as conveyor belts for sediment transport. Collectively, LBE interactions aggregate to exert primary control of sediment storage within and fluxes of sediment out of mountain rivers systems.	Billi, 1988; Kirchner et al., 1990; Paola et al., 1992; Reid and Hassan, 1992; Sear, 1992, 1995, 1996; Paola and Seal, 1995; Laronne et al., 2001; Lancaster et al., 2001; Shamloo et al., 2001; Thompson, 2001, 2008; Faustini and Jones, 2003; Yager et al., 2007, 2012; Nitsche et al., 2011; Ghilardi et al., 2014; Thompson et al., 2016; Papanicolaou and Tsakiris, 2017; Sutfin and Wohl, 2019
Channel stability and organization of fluvial landforms	LBEs comprise a key constituent of coarse-bedforms including stone clusters, transverse ribs, stone cells, and alluvial steps. These bedforms all tend to increase channel resistance which is hypothesized to directly correlate with conditions of maximum bed stability. LBEs specifically promote stability through interlocking and imbrication with surrounding substrates. Evidence suggests LBEs in natural rivers may organize in order to maximize flow resistance and promote channel stability.	Nowell and Church, 1979; Brayshaw, 1985; Grant et al., 1990; Hassan and Reid, 1990; Church et al., 1998; Madej, 2001; Zimmermann and Church, 2001; Buffington et al., 2002; Church and Zimmermann, 2007
Landscape evolution	LBEs are a product of landscape evolutions processes but also have direct autogenic feedbacks on channel and hillslope evolution due to their ability to mediate fluvial incision and shape channel morphology.	Benda and Dunne, 1997; Sklar and Dietrich, 2004; Johnson et al., 2009; Turowski et al., 2007, 2008; Attal et al., 2015; Shobe et al., 2016; Glade et al., 2019

Morphodynamic processes	Through their ability to steer the flow, influence hydraulics and sediment transport processes, regulate landscape evolution, and self-organize LBEs have first order control on the morphodynamic evolution of rivers channels.	Wittenberg and Newson, 2005; Piedra et al. 2012; Tan and Curran, 2012; MacKenzie and Eaton, 2017; Williams et al., 2019

Table S2. Existing definitions of LBEs.

Reference	LBE definition
Grant et al., 1990	Clasts with diameters on the same order as the depth of the bankfull channel; wood not included.
Grant et al., 1990	Clasts equaling or exceeding the 90th percentile of the bed material; wood not included.
Hassan et al., 2019	Clasts equaling or exceeding the 95th percentile of the bed material; wood not included.
Thompson, 2008; Ferguson et al., 2017	Clasts with b-axis equal to or greater than 0.256 m; wood not included.
Finnegan et al., 2019	Clasts with planform diameter equal to or greater than 0.3 m; wood not included.
Benda, 1990; Nitsche et al., 2011; Schneider et al., 2015a	Clasts with b-axis equal to or greater than 0.5 m; wood not included.
Shobe et al., 2016	Clasts with b-axis equal to or greater than 1 m; wood not included.
Grant and Swanson, 1995	Clasts that protrude from an otherwise relatively level surface by at least 1.5 m; wood not included.
Lisle, 1986; Thompson, 2001	Boulders or protrusions with the longest dimension larger than one-third bankfull width; wood included.
Weichert, 2006; (see also Bathurst, 1985; Shamloo et al., 2001)	Review of roughness length scale definitions where 'large-scale' features are generally defined as having relative submergence[a] values < 3; wood not included.
Fang et al., 2017; Monsalve et al., 2017; Papanicolaou and Tsakiris, 2017	Relative submergence threshold value of 3.5 used to define a 'low relative submergence regime' for replicating flows around LBE-like objects in flumes; wood not included.

[a]Relative submergence defined as ratio of flow depth to LBE diameter.

2. Study river segment

None.

3. Methods

3.1. Topo-bathymetric mapping

This was the first time a detailed topographic map has been produced of the Yuba River between New Bullards Bar Dam and Colgate Powerhouse (study site). Position of the aircraft performing ALS collection was measured twice per second (2 Hz) by an onboard differential GPS unit, and aircraft attitude was measured 200 times per second (200 Hz) as pitch, roll and yaw (heading) from an onboard inertial measurement unit (IMU). To allow for post-processing correction and calibration, aircraft and sensor position and attitude data are indexed by GPS time. The average overall ground classified density including bathymetric bottom was 3.96 points/m^2, while the bathymetric bottom return density alone was 2.30 points/m^2. Average discharge over this time period was estimated to be 1.19 m^3/s at the downstream study site boundary, which is hereafter referred to as the 'lidar baseline' flow condition.

Review of the initial bare-earth and sub-aqueous bathymetry lidar files (ground points) from Quantum Spatial indicated a significant number of true ground points associated with boulders, exposed bedrock, and other high variability terrain features had been erroneously rejected (i.e., Type I errors). Using a publically available ground classification algorithm (Isenburg, 2016) a procedure was developed to reclassify and reincorporate these Type I errors back into the ground point dataset (Wiener and Pasternack, 2016). The objective of this process was balancing proper classification of previous Type I errors without introducing new Type II errors (e.g. incorrectly classified ground points). Following processing, the revised lidar dataset was subjected to significant vetting through visualization methods and hand editing to remove lingering classification errors. The reclassification procedure increased average point density of the final ground point dataset from 9.0 to 13.9 pts/m^2 (Wiener and Pasternack, 2016).

In addition to (mis)classification issues, NIR and Green lidar have inherent coverage and water-depth penetration limitations. Despite overall excellent lidar penetration and coverage, the survey did not yield ground returns for ~ 40,873 m^2 of in-water areas representing ~ 22% of the open water area present at the time of the survey. Supplemental bathymetric observations at three locations within the study site were made between July 8 and 9, 2015 by kayak using a single-beam echosounder coupled to a real-time kinematic global positioning system (RTK GPS) covering an area of ~13,530 m^2 (~ 33% of area missing data).

Limited access and rugged terrain within the river canyon largely prevented kayak and foot access to much of the remaining areas lacking bathymetric data. To fill these data gaps an approach developed by Legleiter et al. (2004) linking known water depths to an image-derived quantity 'X', defined as the natural logarithm of two multi-spectral imagery wavelengths, was used to predict water depths and derive additional bathymetric data (depth-derived data; Wiener and Pasternack, 2016). Source imagery for depth-to-X statistical models was obtained from the National Agricultural Inventory Program (NAIP). The source imagery, dated from 2014, was close to the date of lidar acquisition, and the 1-m resolution imagery included three spectral bands; green (460 nm, width 60 nm); red (635 nm, width 50 nm), and blue (560nm, width 50nm). Rasters of lidar intensity returns were used to georeference NAIP imagery with other topographic/bathymetric data to ensure proper alignment of depth-derived data.

Depth data for training depth-to-X statistical models was derived from water surface elevations (WSE) obtained during the lidar acquisition and final lidar ground points such that depths were approximated as: WSE minus ground surface elevation. Edge effects were minimized by only selecting points at least 2 meters from the georeferenced imagery's waters' edge. The training dataset consisted of 137,022 estimated depth points. For each depth point, underlying imagery band wavelength values were sampled and statistical relationships (linear and/or polynomial regression models) were created relating depth to all possible band ratio combinations (i.e., X values). Statistical models were evaluated based on goodness of fit criteria such as R^2 values. Models were also tested in a predictive mode against an independent depth dataset (i.e. the single-beam soundings) using three performance metrics: (i) lowest root mean square error (RMSE); (ii) linear regression slope between predicted depths and observed sounding depths closest to unity; and (iii) R^2 between predicted depths and observed sounding depths closest to unity.

The depth-to-X method has typically been applied to lowland, shallow, relatively clear flowing, gravel-bottom rivers with higher resolution imagery (Legleiter et al., 2004). Locations within the study site where the method was implemented were characterized by complex and heterogeneous terrain and substrates, varying water turbidity, and generally high depths. Due to differences in statistical model performance, the final mapping approach included a suite of depth-to-X predictive models spatially distributed along the river. Use of one model over another was based on an analysis of localized fit using the same metrics above (Wiener and Pasternack, 2016). A total of 168,965 depth-derived ground points covering an area of ~ 15,783 m^2 were predicted and included in the final topographic map (~ 39% of area missing data). To fill remaining locations lacking topographic data all available data sources were used to strategically place "augmented points". Ground elevations at these locations were assigned manually based on best professional judgement and neighboring points. A total of 2,182 augmented ground points, many analogous to ‘breaklines’, were manually input and included in the final topographic map. Merging all data sources resulted in a total of 69,784,144 topographic points. Of these 21,279,867 points at an average spacing of 0.25 m and average density of ~ 16 pts/m^2 were located within the river corridor.

Lidar accuracy was assessed independently based on estimates of absolute accuracy, the error of the lidar derived ground surface compared to a more accurate survey method. Absolute accuracy was computed by comparison of the lidar ground surface to 23 ground check points and 24 bathymetric check points from an RTK-GPS survey. The Fundamental Vertical Accuracy (FVA), a measure of error reported at the 95% confidence level (i.e. 1.96*RMSE), for ground points and bathymetric points were 0.037 m and 0.117 m, respectively. A full account of the mapping efforts, accuracy of mapping data, and post-processing of data is detailed in Wiener and Pasternack (2016).

A WSE point dataset was also provided by Quantum Spatial. Review of the WSE data indicated the presence of numerous erroneous points. Spuriously high and low water surface points were manually removed resulting in a final dataset of 147,644 points representing the lidar baseline flow condition water surface (Wiener and Pasternack, 2016). Triangular irregular network (TIN) based interpolation methods were used to generate a continuous surface from the verified WSE points where sufficient data was present.

3.2. Observed LBE dataset

None.

3.3. LBE mapping

3.3.1 Roughness surface model generation and testing question 1

This section presents additional details on the procedure for mapping LBEs from 3D topographic point clouds. In the procedure's first step, the "lasground_new.exe" ground classification algorithm of Isenburg (2016) was used to create a series of smoothed digital terrain models (DTMs) needed for creating roughness surface models (RSMs). As discussed in the main text the algorithm applies an adaptive TIN approach to iteratively classify ground points from an unclassified point cloud and requires input of a point cloud and six user-defined parameters. The approach for setting the algorithm's parameters is described below, focusing on the spike, offset, down-spike, and step parameters as these were found to disproportionally influence the algorithm's performance.

To constrain the range of ground classification algorithm parameter values an initial 'larger' parameter space was informed by several physically based metrics. For example, roughness length scales such as a representative grain size or a minimum LBE height were considered when setting the range for spike, offset, and down-spike parameter values. These parameters control if points are classified as ground or removed from the algorithm's iteratively generated ground surfaces. Summarily, the specified length scale(s) define thresholds for ground point classification based on how much points extend below or protrude above an otherwise smooth but variable bed surface. Previously reported estimates of the study site's D_{50} and D_{16} values (D is particle diameter and the subscript is the percent of particles finer) of 0.128-0.256 m and 0.032-0.64 m, respectively, and two representative LBE sizes, 0.256 m and 0.5 m, were used to define the range of parameters (Table S3). The latter two values correspond to the diameter of boulders in the Udden-Wentworth scale (Wentworth, 1922) and a common length used to define LBEs (Table S2), respectively.

The algorithm's 'step' parameter, which controls the size of the search window used to add points to the ground surface was also informed by physical considerations. Larger window sizes function to remove increasingly larger terrain features such that cohesive terrain features bigger than the window-size are often preserved in the final ground classification. However, larger window sizes can also modify the underlying terrain through non-ground classification, especially where steep slopes or rapidly undulating terrain features are present (Zhang and Whitman, 2005). For RSM generation and LBE mapping purposes, where the goal is creating a smoothed ground surface that retains the dominant topographic features of the original ground surface, a reasonable recommendation is for window sizes to be larger than the typical planform diameter of LBEs expected to be present or that are desired to be mapped but smaller than the expected/desired maximum LBE diameter or scale of dominate terrain features. For this study, step sizes ranged between 1.5 – 4.6 m (~3-9 DEM raster cell lengths).

Altogether, 14 unique parameter combinations were established and used to generate smoothed point clouds and associated DTMs (Table S3). The 14 smoothed DTMs were assessed qualitatively with *LAStools* 3D visualization software based on two visual criteria: i) removal of clearly discernable LBEs; and ii) retaining the dominant topographic character of the original ground surface (i.e., location of slope breaks, small-scale terrain undulations, meso-scale terrain features). As discussed in the main text, six DTMs were selected to create a series of unique RSMs and a binary threshold approach was used to map discrete sets of preliminary LBEs from each RSM. After assigning a random selection of 70% of the LBE_o data to a 'training' dataset the average RSM value of all raster cells located along the exterior boundary of each LBE_o polygon in the training set were calculated for each RSM, independently. The average of these values served as the vertical threshold for each RSM (Figure S1). While thresholds were unique for each RSM, they were obtained through a numerically consistent approach to avoid introduction of bias.

To identify the preferred ground classification algorithm parameter combination and associated RSM, preliminary LBEs mapped from each smoothed DTM were quantitatively compared to the remaining 30% of the LBE_o data using the study's four performance metrics. Prior to conducting this analysis LBE_o training and test data subsets were compared for similarity to provide confidence that training LBE data characteristics did not differ significantly from LBE test data, and thus not bias the mapping process. Metrics selected for this comparison were LBE planform area and max RSM raster value (D_c) of each LBE in the respective datasets. Comparison was performed using Welch's t-test and the Kolmogorov-Smirnov test. Testing concluded an inability to reject the null hypotheses that distributions of these metrics had equivalent means and came from the same family of distribution at the 95% confidence level ($p>>0.05$).

Quantitative assessment of predicted LBEs used four performance metrics. Details of each metric are described in the following paragraphs.

The first metric, Producers accuracy (PA), is the ratio of the number of predicted LBEs (N_p) spatially intersecting observed LBEs (N_o) to the number of observed LBEs:

$$PA = \frac{N_p \cap N_o}{N_o} \quad \text{(Eq. 1)}$$

PA is widely applied across disciplines (Labatut and Cherifi, 2011; Barsi et al., 2018; Shao et al., 2019) and in this context simply measures the hit-rate of predicted LBEs relative to observed LBEs. Since PA does not penalize for over-mapping the metric is entirely focused on accuracy without consideration of precision or commission errors.

The next metric, Producers overlap (PO), is the ratio of the area of predicted LBEs (A_p) spatially overlapping the area of observed LBEs (A_o) to the area of observed LBEs from the set of observed LBEs that spatially intersect predicted LBEs:

$$PO = \frac{A_p \cap A_o}{A_o \in N_o \cap N_p} \quad \text{(Eq. 2)}$$

This metric is simply the relative percent of total observed LBE area that is correctly predicted for the subset of observed LBEs that overlap with a predicted LBE. By constraining the denominator to only intersecting observed and predicted LBEs this metric focuses on the accuracy of how well those LBEs were predicted. Albeit similar to other metrics this formulation is believed to be unique.

Both PA and PO metrics range from 0-1 with higher values indicating better precision and accuracy, respectively. One caveat is that both metrics benefit from more area being predicted as LBE and lack a penalty for commission errors. For example a rectangle covering the entire domain of observed LBEs would result in the max value of unity for both metrics. PO also does not penalize for omission errors and thus should be used in consideration with other metrics that do, such as PA.

Two other metrics, modified Jaccard similarity index (MJI) and missed-to-excess ratio (MER), penalize commission errors while being less sensitive to omission errors. The Jaccard similarity index is a common metric for comparing polygons that penalizes both omission and commission (Labatut and Cherifi, 2011). However, since the full set of observed LBEs was unknown the metric has been modified and is calculated as the ratio of the area of intersect between predicted LBEs and observed LBEs to the area of union between predicted LBEs and observed LBEs from the set of observed LBEs that spatially intersect predicted LBEs and the set of predicted LBEs that spatially intersect observed LBEs:

$$MJI = \frac{A_p \cap A_o}{A_p \cup A_o} \in (N_o \cap N_p \text{ and } N_p \cap N_o) \qquad \text{(Eq. 3)}$$

The metric assumes that excess LBEs predicted in the vicinity of an observed LBE should be penalized. The MJI metric ranges from 0-1 with a value of unity indicating perfect mapping for the set of LBEs considered.

Lastly, MER is defined as the ratio of the area of observed LBEs less the area of intersection between observed and predicted LBEs (e.g., area of missed observed LBE mapping) to the area of predicted LBEs less the area of intersection between predicted and observed LBEs (e.g., area of excess predicted LBE mapping):

$$MER = \frac{A_o - A_p \cap A_o}{A_p - A_o \cap A_p} \qquad \text{(Eq. 4)}$$

Here it is assumed that a greater extent of predicted LBE mapping should yield a high probability of overlap with observed LBEs and penalizes the amount of observed LBE area that is missed scaled by excess predicted LBE mapping. The MER metric ranges from 0 - ∞. Larger MER values are presumed better for several reasons. First, it is more ideal for only small areas of observed LBEs to be missed resulting is less variation in the numerator between predictions. Second, preliminary analysis suggests excess LBE prediction tends to be much greater than missed area (denominator >> numerator) across predictions and excess area is more variable between predictions. Thus higher MER values are associated with less missed mapping per unit excess mapping and functionally MER values do not exceed unity under the above described circumstances. Though similar to miss rate we are not aware of other studies using the MER metric.

Table S3. Parameters and qualitative assessment of 14 smoothed DTMs. Selected DTMs marked with *.

ID	Step (m)	Bulge (m)	Spike (m)	Down spike (m)	Offset (m)	Intensity	Qualitative finding (LBE removal; Terrain modification)[ab]
P-LBE-1*	3.05	0.03	0.15	0.30	0.15	extra	Excellent; Moderate
P-LBE-2	1.52	0.03	0.15	0.30	0.15	extra	Moderate; Moderate
P-LBE-3*	4.57	0.03	0.15	0.30	0.15	extra	Excellent; Moderate
P-LBE-4	3.05	0.03	0.15	0.0	0.15	extra	Poor; Moderate
P-LBE-5	3.05	0.30	0.15	0.30	0.15	extra	Moderate; Moderate
P-LBE-6	3.05	0.03	0.15	0.30	0.15	hyper	Moderate; Moderate
P-LBE-7	3.05	0.03	0.50	0.25	0.50	extra	Poor; Excellent
P-LBE-8	3.05	0.03	0.25	0.25	0.25	extra	Poor; Excellent
P-LBE-9	3.05	0.03	0.13	0.50	0.13	extra	Moderate; Moderate
P-LBE-10*	3.05	0.03	0.13	0.25	0.13	extra	Excellent; Moderate
P-LBE-11*	3.05	0.03	0.03	0.13	0.03	extra	Excellent; Moderate
P-LBE-12*	3.05	0.03	0.06	0.13	0.06	extra	Excellent; Moderate
P-LBE-13*	4.57	0.03	0.06	0.13	0.06	extra	Excellent; Poor
P-LBE-14	4.57	0.03	0.13	0.25	0.13	extra	Excellent; Poor

[a]LBE removal performance increases from: poor to moderate to excellent.
[b]Terrain modification performance increases from: poor to moderate to excellent.

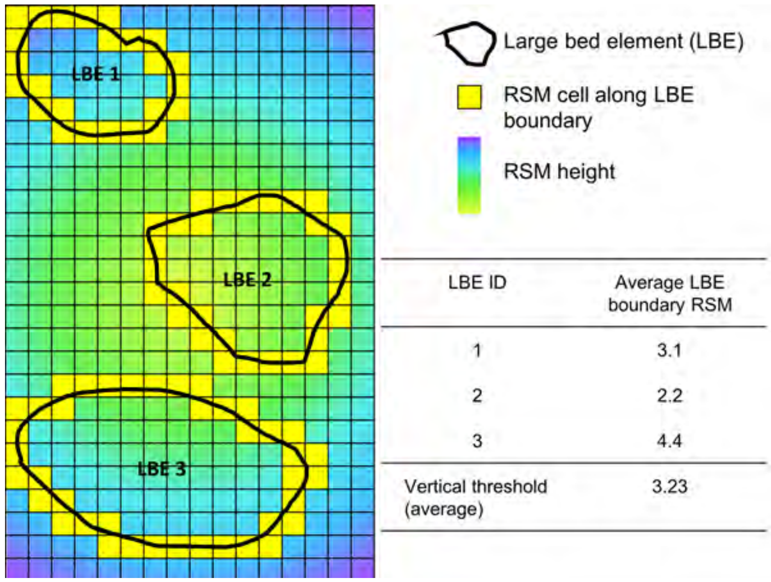

Figure S1. Conceptual depiction of how vertical threshold were calculated from LBE_o training data. The training data was constant but RSM heights would vary between smoothed DTMs.

3.3.2 LBE extraction and accuracy testing for question 1

Approaches for LBE extraction tested in this study were informed by methods for mapping tree-crowns from remotely-sensed imagery and/or topographic data. Tree-crown mapping methods can be broadly classified into those that apply mathematical morphology (Andersen et al., 2001; Koukoulas and Blackburn, 2005), object-based image analysis (Sullivan et al., 2009; Jakubowski et al., 2013), edge-detection, local-maxima filtering and detection (Popescu and Wynne, 2004; Argamosa et al., 2016), clustering (Culvenor, 2002; Morsdorf et al., 2004), valley-following (Leckie et al., 2003), region-growing (Barnes et al., 2017; Dalponte et al., 2019), watershed segmentation (Chen et al., 2006; Koch et al., 2006; Kwak et al., 2007), and graph based (Strîmbu and Strîmbu, 2015) approaches. Nearly all approaches use a canopy height model (CHM) as a starting point. Smoothing CHMs with low-pass mean or Gaussian filters prior to crown mapping is also typical (Chen et al., 2006; Kwak et al., 2007). Crown mapping approaches differ in their computational expense, number of parameters, and public availability. Given the goal of mapping LBEs at the river segment scale, computational efficiency was a necessary consideration when testing approaches. Reproducibility using open-source software was also favored. Details on the five LBE extraction approaches used in this study are provided in the following paragraphs.

The simplest and most computationally efficient strategies, (i) RSM with vertical threshold and (ii) Gaussian filtered RSM with vertical threshold, involved applying a vertical threshold to the RSM or filtered RSM. Areas above the threshold were considered LBE and those below were masked out as non LBE. This is similar to Otsu's (1979) binary threshold approach, the only difference being how thresholds were specified. Conceptually, vertical thresholds could be data-driven based on LBE training data, optimized through comparison with LBE testing data using the study's performance metrics, based on representative length scales, be statistical (e.g. Otsu, 1979), or set qualitatively. For approach (i) 12 thresholds were tested (Table S4). Eleven values between 0.1524-0.4572 m set in increments of 0.03048 m were tested as these covered a wide range of reasonable LBE length scales. The final threshold value of 0.283 m was derived from averaging the set of averaged RSM values for cells along the boundary of each observed LBE polygon (Figure S1).

For approach (ii) three parameters were needed: two for the Gaussian filter (standard deviation of kernel [σ] and window-size) and the vertical threshold. A total of six parameter combinations were tested using three different sigma values (0.152, 0.305, and 1.524 m), two different window sizes (3 cells and 5 cells), and vertical thresholds calculated as the average of all averaged Gaussian filtered RSM values for cells along the boundary of each observed LBE polygon (Table S4). When applying a Gaussian filter to CHMs, Dralle and Rudemo (1996) found tree-crown mapping to be insensitive to the sigma parameter but that window-size did influence performance due to the effect on the smoothed CHMs. For tree-crown mapping they recommended window sizes should be less than the crown size of the smallest tree of interest. Gaussian filtering was done in R code using the 'spatialEco' package (Evans, 2019). Raster masking using the vertical thresholds for approach (i) and (ii) were done with the ArcGIS spatial analyst extension tool suite and converted to polygons using the raster to polygon tool.

Marker-controlled watershed segmentation (MCWS) approaches: (iii) RSM with MCWS and constant window-size; (iv) RSM with MCWS and variable window-size; and (v) Gaussian filtered RSM with MCWS and constant window-size, were slightly more complex and computationally intensive. All MCWS approaches involved two steps: first, markers or "LBE tops" were detected from the RSM; and second, markers were used to delineate distinct LBEs from the RSM. The number of parameters for each approach varied and are listed in Table S4.

Markers were retrieved from the RSM using a variable-window local-maxima filter algorithm (e.g. Popescu and Wynne, 2004) implemented in R code using the 'ForestTools' package (Plowright and Roussel, 2020). The algorithm requires input of an RSM, a parameter controlling the minimum RSM value for a pixel to be considered a marker, and a search window size. The window-size in the algorithm can be set as a constant or vary as a function of RSM pixel value. Both constant and variable window sizes were tested. Functions to define window-size can be based on observed data and/or assumptions of idealized relationships between feature height and area (Popescu and Wynne, 2004; Chen et al., 2006). Comparing the relationship between D_c and planform area for the observed LBE data with several functions for ideal spheroid objects found over 98% of LBEs to geometrically reside in-between models for an oblate (wide) spheroid and a prolate (tall) spheroid, in the domain of spherical objects (section 3.3.2.2). Therefore, a spherical model where window-size was set equal to the pixel RSM value divided by two was used to define the variable window-size (e.g., window size was set equal to the planform radius of each potential LBE based on RSM value). In order to control for very small window sizes that would add to computational time and also be inefficient at mapping LBEs (Chen et al., 2006), a constraint was placed requiring a minimum window-size. Two minimum sizes were tested, 3 and 5 m, respectively which equated to windows with radii of ~3 and ~5 raster cells.

In order to constrain the parameter spaces of approaches (iii-v) only data-driven parameterization methods were used when specifying other input parameters. Values for the minimum RSM value for a pixel to be considered a marker were based on five calculations from the observed LBE data using different approximations for the minimum height observed features protruded above the smoothed DTM raster:

- (1) the median of the set of averaged RSM values for cells within each observed LBE polygon;
- (2) the average of the set of averaged RSM values for cells within each observed LBE polygon;
- (3) the average of the set of maximum RSM values for cells within each observed LBE polygon;
- (4) the median of the set of averaged RSM values for points generated every 0.31 m along a border line located one raster cell inward of each observed LBE polygon's border; and

- (5) the average of the set of averaged RSM values for raster cells along each observed LBE polygon's border.

Following marker identification, LBE polygons were created using a watershed segmentation function (e.g. Beucher and Meyer, 1993) implemented in R code using the 'ForestTools' package (Plowright and Roussel, 2020). The segmentation algorithm requires input of markers, a RSM raster, and a parameter that controls the minimum RSM value for a pixel to be included in the segmentation. Values for the minimum RSM parameter were based on six calculations using the observed LBE data to approximate the minimum value that the edge of observed features protruded above the smoothed DTM raster:

- (1) the median of the set of median values of RSM values for points generated every 0.31 m along each observed LBE polygon's border;
- (2) the median of the set of averaged RSM values for points generated every 0.31 m along each observed LBE polygon's border;
- (3) the average of the set of averaged RSM values for points generated every 0.31 m along each observed LBE polygon's border;
- (4) the median of all RSM values for points generated every 0.31 m along each observed LBE polygon's border;
- (5) the average of the set of minimum RSM values for cells along each observed LBE polygon's border; and
- (6) the average of the set of minimum RSM values for cells within each observed LBE polygon.

Ultimately, 10 parameter combinations were tested for approach (iii), two combinations for approach (iv), and 14 combinations for approach (v) (Table S4).

Table S4. Parameters for 44 predicted LBE datasets.

ID	Parameters		
(i) RSM with vertical threshold: One parameter - vertical threshold (m)			
V-1	0.152		
V-2	0.183		
V-3	0.213		
V-4	0.244		
V-5	0.274		
V-6	0.305		
V-7	0.335		
V-8	0.366		
V-9	0.396		
V-10	0.427		
V-11	0.457		
V-12	0.283		
(ii) Gaussian filtered RSM with vertical threshold: Three parameters - vertical threshold (m); σ (m); window size (# of cells)			
GV-1	0.031	0.152	3
GV-2	0.031	0.305	3
GV-3	0.031	1.524	3
GV-4	0.011	0.152	5
GV-5	0.011	0.305	5
GV-6	0.011	1.524	5
(iii) RSM with MCWS algorithm and constant window size: Three parameter - minimum marker height (m); minimum crown height (m); window size (m)[a]			
MCWS-C-1	0.283 (5)	0.033 (5)	3
MCWS-C-2	0.297 (1)	0.118 (1)	3
MCWS-C-3	0.297 (1)	0.169 (4)	3
MCWS-C-4	0.423 (2)	0.07 (6)	3

ID	Parameters				
MCWS-C-5	0.423 (2)	0.169 (4)	3		
MCWS-C-6	0.423 (2)	0.272 (3)	3		
MCWS-C-7	0.312 (4)	0.192 (2)	3		
MCWS-C-8	0.312 (4)	0.272 (3)	3		
MCWS-C-9	0.283 (5)	0.033 (5)	6		
MCWS-C-10	0.423 (2)	0.07 (6)	6		
(iv) RSM with MCWS algorithm and variable window size: Three parameter - minimum marker height (m); minimum crown height (m); window size function[a]					
MCWS-V-1	0.312 (4)	0.272 (3)	{3 if (RSM/2) <3; else (RSM/2)}		
MCWS-V-2	0.312 (4)	0.272 (3)	{5 if (RSM/2) <5; else (RSM/2)}		
(v) Gaussian filtered RSM with MCWS and constant window size: Five parameter - σ (m); window size (# of cells); minimum marker height (m); minimum crown height (m); window size (m)[a]					
GV-MCWS-C-1	0.152	3	0.031 (1)	0.016 (1)	0.914
GV-MCWS-C-2	0.305	3	0.027 (1)	0.019 (1)	0.914
GV-MCWS-C-3	0.305	3	0.027 (1)	0.024 (4)	0.914
GV-MCWS-C-4	0.305	3	0.043 (2)	0.024 (4)	0.914
GV-MCWS-C-5	0.914	3	0.026 (1)	0.025 (4)	0.914
GV-MCWS-C-6	0.914	3	0.042 (2)	0.025 (4)	0.914
GV-MCWS-C-7	1.524	3	0.026 (1)	0.019 (1)	0.914
GV-MCWS-C-8	0.152	5	0.011 (1)	0.006 (1)	0.914
GV-MCWS-C-9	0.305	5	0.009 (1)	0.007 (1)	0.914
GV-MCWS-C-10	0.914	5	0.008 (1)	0.007 (1)	0.914
GV-MCWS-C-11	0.914	5	0.013 (2)	0.009 (4)	0.914
GV-MCWS-C-12	0.914	5	0.02 (3)	0.009 (4)	0.914
GV-MCWS-C-13	1.524	5	0.013 (2)	0.01 (4)	0.914
GV-MCWS-C-14	1.524	5	0.008 (1)	0.007 (1)	0.914

[a]Number in parenthesis next to minimum marker height and minimum crown height parameters corresponds to calculation method listed on pages 19-20 of supplement.

3.3.2.1 Filtering

As discussed in the main text, two steps were taken to address uncertainty and filter the preferred predicted LBE dataset (LBE_p). Topographic sources such as imagery-derived bathymetric estimates and augmented points were considered to have greater uncertainty than lidar. Therefore, a convex hull was generated surrounding areas where topographic information was derived from these data. Predicted LBE polygons with >50% of their area overlapping this area were removed. Remaining portions of LBE_p polygons overlapping the area of uncertain source topography were erased using the convex hull polygon. The resulting set of LBE polygons is referenced herein as LBE_{p-1}.

A second filtering process was used to remove additional LBE_{p-1} polygons in areas with low topographic point densities and low standard deviation in elevations. The belief that these factors would results in poor LBE predictions was supported by comparing metrics from polygons in the LBE_o dataset that were completely missed in the preferred LBE_p dataset versus those that were at-least partially mapped. To do this, each LBE_o polygon was defined as being matched or missed based on spatial intersection with the preferred LBE_p polygons. Lidar point densities (points/m^2) and the mean standard deviation of gridded elevations ($\overline{\sigma_z}$) were calculated for each LBE_o where local standard deviation (σ_z) was calculated individually for each raster cell using the bare-earth point cloud. Point densities and $\overline{\sigma_z}$ for LBE_o polygons matched by the predicted LBEs were generally greater than those for missed LBE_o polygons. Further, comparison of point density and $\overline{\sigma_z}$ from matched and missed LBE_o polygons using Welch's t-test and the Kolmogorov-Smirnov test concluded that the null hypotheses that distributions had equivalent means and came from the same family of distribution could both be rejected above the 95% confidence level ($p<<0.05$). Thresholds for point density and $\overline{\sigma_z}$ to filter the LBE_{p-1} data were generated by maximizing the difference in relative frequency within the first break of histograms of missed and matched LBE_o polygons by iteratively adjusting histogram break values with the two constraints that matched and missed histograms had the same break values, and that frequencies of the first three breaks had a monotonic trend. The break values maximizing the difference in point density and $\overline{\sigma_z}$ were 2.9 points/m^2 and 0.03 m, respectively. These values were used to filter the LBE_{p-1} data by removing polygons with either point densities or $\overline{\sigma_z}$ values below the respective thresholds.

3.3.2.2 Geometry

Geometric analysis included comparing the D_c-to-LBE planform area relationship for each LBE in the final LBE dataset to that of several idealized spheroidal geometries (Figure S2). For example, the top (planform) area of perfect sphere is $\pi 0.5 {D_c}^2$. Relations for oblate and prolate spheroids are shown in Figure S2.

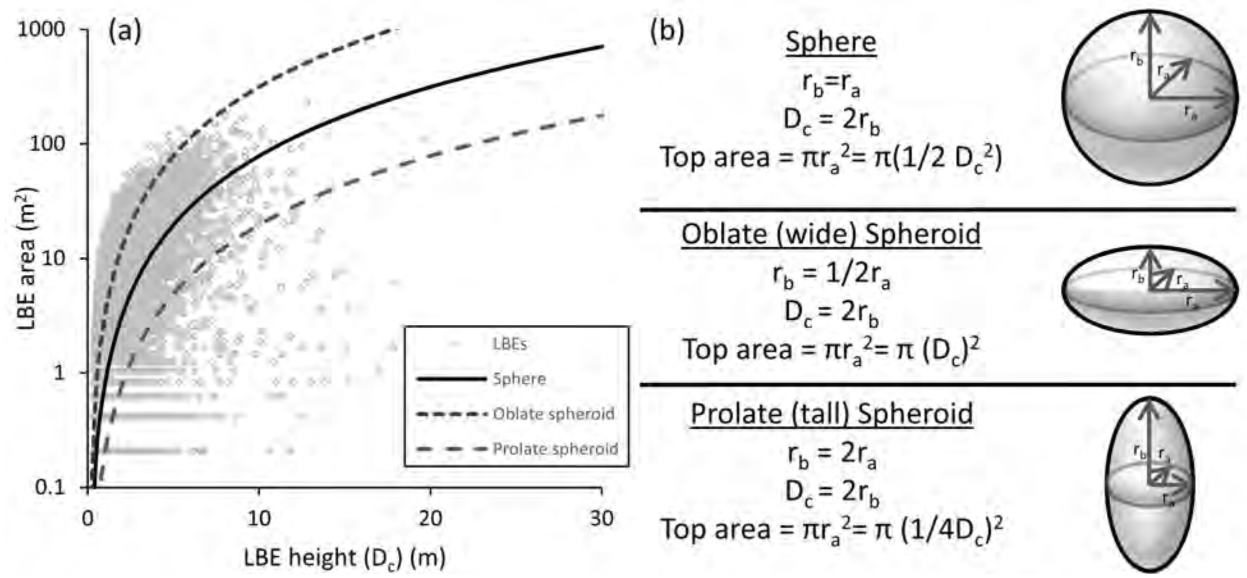

Figure S2. (a) LBE planform area versus LBE height (D_c) overlain with relations for several idealized spheroidal geometries and (b) visual examples of idealized spheroids.

3.4. Two-dimensional hydrodynamic modeling

For this study, the 2D model known as Sedimentation and River Hydraulics—Two-Dimensional model (SRH-2D) v. 2.2 was used to predict hydrodynamics. The Surface-water Modeling System (SMS) v. 11.2 graphical user interface (Aquaveo, Inc.) was used for pre- and post-processing model inputs, parameters, and outputs. SRH-2D v. 2.2 solves the 2D dynamic wave equations (i.e. the depth-averaged St. Venant equations) (Lai, 2008). The model uses a finite volume numerical scheme that can handle subcritical and supercritical flow. The model also incorporates seamless wetting-drying algorithms that results in fewer tuning parameters needed to generate solutions. Model outputs include WSE (m), water depth (h) (m), depth-averaged velocity components (longitudinal, U, and lateral, V) (m/s), depth-averaged water speed ($\overline{U}$) (m/s), Froude number, and shear stress (τ) (N/m^2). SRH-2D was developed by the U.S. Bureau of Reclamation and is freely available to the public. For more information, see https://www.usbr.gov/tsc/techreferences/computer%20software/models/srh2d/index.html. Model development followed the Pasternack (2011) textbook.

The model's finite-volume numerical solver requires input of a computational mesh. Three computational meshes with ~ 1 m internodal spacing were made to cover the extent of inundation associated with flows spanning two orders of magnitude (e.g. approximately 1.2–343.6 m^3/s) (Figure S3). SMS software was used to build the final suite of meshes based on the approach described by Pasternack (2011).

The two primary model parameters in SRH-2D include bed roughness as approximated using variable Manning's n and isotropic kinematic eddy viscosity (E). For model development, unresolved roughness (e.g. not represented in the bare-earth topography) was initially estimated using a constant Manning's coefficient (n) of 0.1 (Pasternack and Senter, 2011). After simulating the lidar baseline flow condition for the whole river, predicted WSEs were compared to the 147,644 collocated WSE measurements from the lidar data. Initial WSE assessment showed the model systematically over-predicted water depth. As a result, additional simulations were conducted with constant roughness coefficients values of 0.07, 0.08, and 0.09, respectively. Computational time limited the assignment and calibration of spatially based roughness values for this study. Testing found a uniform value of 0.09 worked best as this value minimized mean square error between measured and predicted WSE values, and observed and predicted velocity magnitudes. This calibrated value, which is physically realistic for the setting (Yochum et al., 2014), was used in all subsequent flow simulations. Sensitivity to large (> 0.01) variations in n values have been observed in 2D models and it is important to address this level of uncertainty (Pasternack, 2011). Sensitivity analysis testing the model's response to such incremental variations in n values found differences in predicted depths and velocities to be relatively minimal (section 3.4.2).

The bed roughness parameter in a 2D model can vary spatially to account for variable bed sediment facies and several methods exist to estimate roughness (Pasternack, 2011). However, use of a constant roughness value is common in 2D modeling and has been shown to both perform well (MacWilliams et al., 2006; L'Hommedieu et al., 2020**;** Reid et al., 2020; Pasternack and Senter, 2011) and produce results similar to models with spatially varied roughness (Lisle et al., 2000). Further, 2D model hydraulic predictions are equally if not more sensitive to topographic inaccuracies than to typical model calibration parameters such as roughness (Pasternack et al., 2006; Pasternack, 2011; McKean et al., 2014). Available methods to estimate spatially varying roughness are generally qualitative (Yochum et al., 2014), empirical (Lisle et al., 2000; Cienciala and Hassan, 2013), or based on iterative numerical simulation (Pasternack, 2011). In addition to varying spatially, roughness may change with discharge. Numerical analysis, flume experiments, and observations in natural rivers suggest that roughness values decrease rapidly with increasing discharge, especially at flows exceeding a channel's banks, prior to stabilizing (Richardson and Carling, 2006; Yang et al., 2007; Ferguson et al., 2017). Contrary to these findings, several 2D modeling studies in gravel-bed rivers have found that roughness does not decrease with increasing stage (Brown and Pasternack, 2008; Pasternack, 2008; Sawyer et al., 2010; Strom et al., 2017). In these studies, contact with new types of roughness elements such as boulder clusters, bedrock outcrops, vegetation, and valley width variations maintain high roughness values as discharge increases. Ferguson et al. (2017) also found resistance to increase at high discharges due to macro-roughness elements of rock walls in a bedrock confined river. It is also possible that selective transport and continued armoring of the bed during increasing discharge could result in near constant bed roughness over a wide range of discharges (Gomez, 1993). Abu-Aly et al. (2014) in applying a methodology to account for spatially distributed effects of riparian vegetation found overall roughness to increase with increasing discharge for a 28.3-km segment of a meandering gravel-bed river. Much like the rivers in these studies the study site was characterized by multiple scales of landform heterogeneity whereby increasing stage continuously encountered new forms of resistance, supporting that a decrease in roughness with increasing discharge was unwarranted. Undeniably, if the model roughness parameter had been allowed to vary spatially, the submergence of macro-roughness features in the low-flow channel with increasing stage would likely have been associated with a localized decrease in roughness. However, for the reasons previously described roughness was held spatially constant.

SRH-2D requires the user to select a turbulence closure scheme and the input of an eddy viscosity coefficient. These inputs are used in calculating the turbulent eddy viscosity term in the turbulent stress forces portion of the equation of motion and influence the degree of turbulent mixing incorporated into the solution process (Lai, 2008). 2D models are particularly sensitive to the eddy viscosity parameterization used to cope with turbulence (Nelson et al., 2016). In the model used in this study, eddy viscosity (E) was a variable in the system of model equations, computed using the following standard equations developed from many studies of turbulence in rivers:

$$E = e^{*}h \cdot u_{*} \qquad \text{(Eq. 5)}$$

$$u_{*} = \overline{U}\sqrt{C_d} \qquad \text{(Eq. 6)}$$

$$C_d = \mathrm{g}\left(\frac{\mathrm{n}^2}{h^{1/3}}\right) \quad \text{(Eq. 7)}$$

where e* is the non-dimensional eddy viscosity coefficient, u* is shear velocity, $\overline{U}$ is depth-averaged water velocity at a point, C_d is a drag coefficient, and g is the gravitational acceleration constant. Equation 5 is a parabolic turbulent eddy model (Zero-Equation) common in hydraulic applications and has been shown to perform well within a variety of riverine settings compared to observed conditions and other turbulence models (Lai, 2008; Nelson et al., 2016). These equations allow E to vary throughout the model domain, yielding more accurate transverse velocity gradients. However, a comparison of 2D and 3D models for a shallow gravel-bed river demonstrated that, even with spatial variation in E, rapid lateral variations in velocity are not simulated to the degree that occur in natural channels, presenting a fundamental limitation of 2D models like SRH-2D (MacWilliams et al., 2006).

The eddy viscosity coefficient term is channel-geometry-dependent, typically varying between 0.3 and 1.0 in larger rivers. Two-dimensional modeling of carefully controlled shallow flumes found that an eddy viscosity coefficient value of 0.075-0.1 is better in shallow gravel/cobble settings (Pasternack and MacVicar, 2013). Subsequent application of a value of 0.1 in the Yuba River did well at capturing the relative size, shape, and flow direction of eddies, with this lower value also helping to decrease over-prediction of low velocities (Pasternack and Senter, 2011; Brown and Pasternack, 2012). An eddy viscosity coefficient of 0.1 was used for all simulations in this study.

To run the 2D model, boundary conditions must be input at all inflow and outflow locations. For inflow locations, discharge must be specified across the face of all upstream boundaries as well as any additional tributary inflow junctions. A corresponding water surface elevation (WSE) must also be defined at the downstream boundary. The study site had two primary upstream inflow boundaries; flows originating from NBB dam into Reach 1 and inflow from the Middle Yuba; and one downstream boundary (Figure S3). Several highly ephemeral tributaries also drain into the study site contributing appreciable flow during climate driven high flow events. In this study, model simulations were grouped into two classes based on input conditions, the methods used to specify model inputs, and reason for conducting the simulation. Specifically, these are (1) *calibration and validation flows*, and (2) *geomorphic synthetic flows*. These simulation classes are described next.

The first class, *calibration and validation flow simulations*, involved attempting to replicate hydraulic and hydrologic conditions in the study site associated with specific periods of data collection. These simulations were used to calibrate model parameters and assess performance of the calibrated model. For these simulations, boundary conditions were assigned to match gauged and/or estimated flow conditions during the associated period of data collection. Discharges at the upstream input boundary were based on USGS gaging station 11413517 or data provided by Yuba Water Agency (YWA). Discharges at the Middle Yuba River were based on USGS gaging stations 11408880 and 11409400 or data provided by YWA as well as estimated accretionary flow. WSEs at the downstream boundary were estimated from a site specific rating-curve or from field measured conditions using RTK-GPS.

The second class of simulation, *geomorphic synthetic flow simulations*, involved modeling a range of hypothetical flow conditions of relevance to understanding the hydraulic mechanisms governing the channel's LBE patterns. Using the calibrated model parameters, a series of four discharges were simulated spanning a range of hydrologic conditions. The four selected discharges represent flows of potential geomorphic importance and are all referenced to the bankfull discharge (10.73 m^3/s) for non-dimensional scaling considerations. The *geomorphic synthetic flows* simulated include a representative baseflow condition of 0.14x bankfull flow, bankfull flow, and two multiples (7.7x and 32x) of the estimated bankfull flow. The 32x bankfull flow simulation corresponded to the peak value for which boundary conditions were available (i.e., availability of downstream stage measurement). The four selected discharges have estimated yearly recurrence intervals of 1.00, 1.06, 1.59, and 3.46, respectively.

Ultimately, simulated flows included two *calibration and validation flow simulations* and four *geomorphic synthetic flow simulations*. The complete array of all specific discharge inputs and downstream WSE values for every 2D model simulation are given in Table S5. Model input locations including tributary locations are depicted in Figure S3. For all simulations, SRH-2D outputs raw hydraulic variable values computed at computational mesh nodes. For each model simulation, a number of steps were taken to process data for later analyses with certain calculations made using the raw (nodal) results and others using post-processed results (e.g. rasterized data). ArcGIS software (ESRI, Redlands, CA) was used to process and analyze 2D model outputs. Initially, wetted area polygons were created for each flow simulation using interpolated depths greater than zero as the minimum threshold (Pasternack, 2011). These wetted area polygons were then used as the interpolation boundaries for each respective flow simulation in the creation of hydraulic variable rasters. All rasters were derived from TIN-based surface models re-sampled to 0.46 m resolution grids to provide an equal-area basis for analysis.

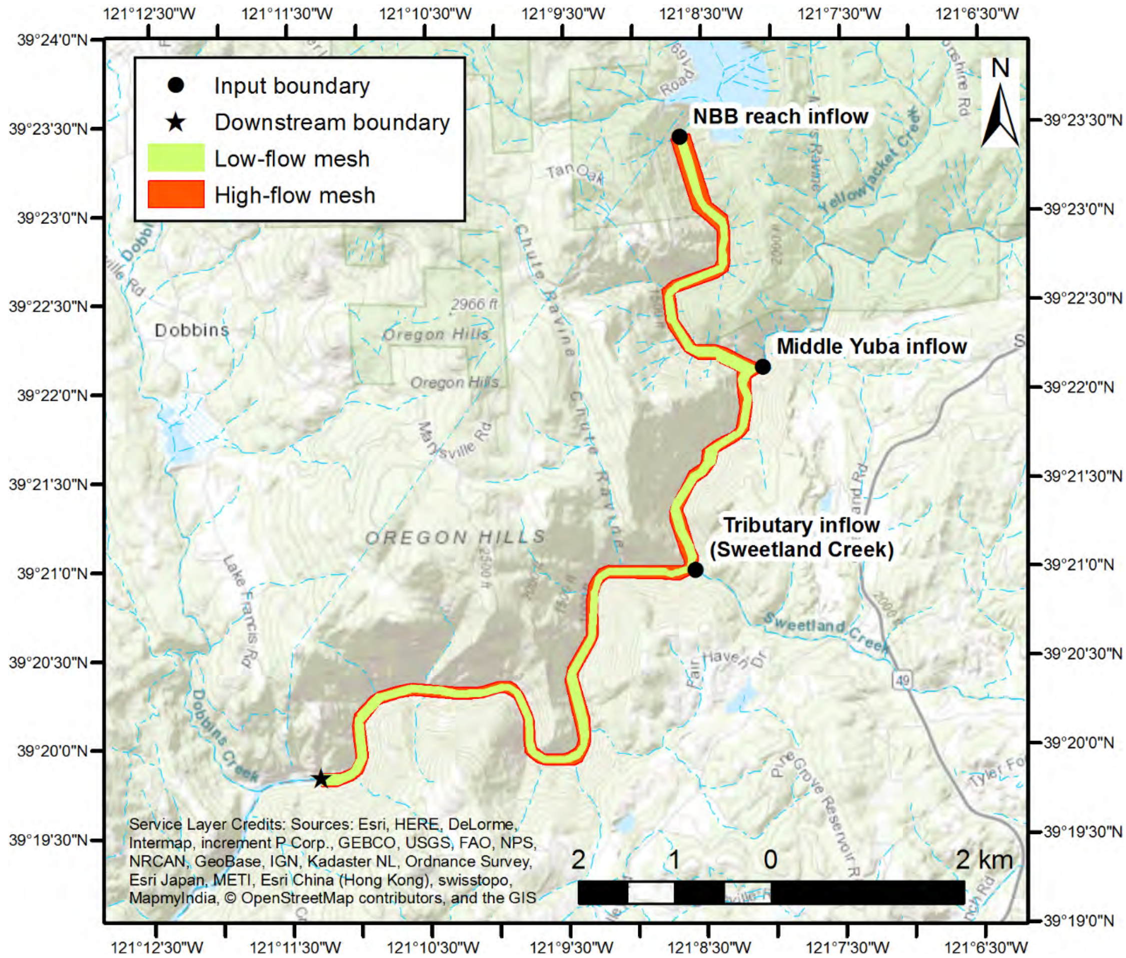

Figure S3. Extent of 2D model low-flow and high-flow computational meshes and location of inflow/outflow boundaries.

Table S5. 2D Model input and parameter values

Total discharge (m^3/s)	Reach 1 input (m^3/s)	Middle Yuba input (m^3/s)	Number of tributary inputs (-)	Total tributary inputs (m^3/s)	Downstream WSE[a] (m)
Calibration and validation simulations					
1.19	0.16	1.02	1	0.01	169.60
3.51	n/a[b]	n/a[b]	1	0.19	169.61
Geomorphic synthetic flow simulation					
1.54	1.40	0.14	0	0	169.51
10.73	10.59	0.14	0	0	169.91
82.12	81.98	0.14	0	0	170.94
343.60	343.45	0.14	0	0	172.06

[a] Elevations referenced to North American Vertical Datum of 1988

[b] Simulation of lower 4.2 km of study site. Only required input of total discharge and tributary input.

3.4.1 2D model assessment

Two-dimensional hydrodynamic models have inherent strengths and weaknesses, thus there is need to assess a model's representation of reality and understand and accept uncertainty in the results. SRH-2D is a proven tool capable of simulating hydraulic conditions in natural rivers (Lai, 2008; Pasternack and Senter, 2011; Brown and Pasternack, 2014). However, there is still a risk of poor model performance. The scope of model assessment is outlined below. Table S6 provides a summary of model assessment testing.

A suite of tests typical of those carried out in the peer-reviewed journal literature for the assessment of 2D models were performed to characterize model performance and uncertainty (Pasternack, 2011). Tests included mass conservation checks, lidar baseline WSE assessment, and fixed-point depth and velocity assessment (Table S6). For the lidar baseline WSE and fixed-point depth and velocity assessment some tests were done using raw (i.e., signed) or absolute (i.e., unsigned) deviations between observed and predicted values, and some on the signed or unsigned percent errors. WSE was analyzed in terms of deviations, not percent error (Brown and Pasternack, 2012). In contrast, percent error of depth and velocity are meaningful because deviations may be a substantial fraction of the observed values. Often percent error for low values of depth or velocity are not evaluated due to low values having inflated numerical errors. Regression and correlation analyses as well as the standard error of the regression slope (SES) and standard error of the regression intercept (SEI) between predicted vs. observed values were computed to add further statistical rigor. Descriptive statistics of model deviations and percent errors and the results of the regression analysis were all used to evaluate model performance. In addition to these metrics commonly used by the 2D hydrodynamic modeling community, three metrics: Nash-Sutcliffe efficiency (NSE), percent bias (PBIAS), and the root mean square error-observations standard deviation ratio (RSR), commonly used in the hydrological modeling community to assess performance of discharge prediction (Moriasi et al., 2007) were also computed.

Table S6. Summary of 2D model assessment testing

Total discharge (m^3/s)	Mass conservation	WSE	Fixed-point velocity magnitude	Fixed-point depth	Manning's n sensitivity
Calibration and validation simulations					
1.19	X	X			X
3.51	X		X	X	X
Geomorphic synthetic flow simulation					
1.54	X				X
10.73	X				X
82.12	X				X
343.60	X				

Mass conservation

The first key model performance criteria, mass conservation, was evaluated by computing the percent difference between specified inflow and model-predicted outflow. Computationally, mass conservation losses increase in the downstream direction as error accumulates, therefore good mass conservation should show little difference in discharge at the downstream model boundary from the total input discharge. Mass conservation error in a 2D model can be anywhere in the 0.01‑2% range (Pasternack, 2011) with errors greater than ~ 2-3% a potential sign of poor model performance (Pasternack and Senter, 2011). This range is typically smaller than uncertainty associated with stream gauges and other discharge measurement methods such as flumes and weirs or stream stage-gauge relations that may be off by upwards of ~ 5-10% of actual values. Mass conservation losses at the downstream model boundary were all less than 1%, well within what is considered acceptable (Table S7).

Table S7. 2D model mass conservation performance summary

Total discharge (m^3/s)	Total outflow (m^3/s)	Percent error (%)
Calibration and validation simulations		
1.19	1.18	-0.60
3.51	3.50	-0.17
Geomorphic synthetic flow simulation		
1.54	1.54	-0.41
10.73	10.67	-0.60
82.12	82.11	-0.01
343.60	342.69	-0.27

WSE evaluation

The next key test was ability of the 2D model lidar baseline simulation to match lidar-measured WSEs as this is a proxy for matching wetted area. Even though lidar-measured WSE values were used to calibrate Manning's n for this simulation, the final deviations between observed and predicted values were non-zero. Thus, deviations between observed and final calibrated WSE predictions were used to characterize uncertainty in water depth after calibration. Longitudinal profiles of observed and predicted WSEs were used to evaluate the spatial distribution of error in WSE deviations. Profiles were generated by discretizing points along the lidar baseline thalweg at 0.91 m intervals. At each point, model predicted WSE and observed WSE were interpolated. The distribution of signed deviations between these values should be centered about zero as this demonstrates no bias in model predictions.

There are no formal standards for evaluating WSE deviations to indicate when a model is invalid, but the greater the deviation from zero the more unreliable the model. Topographic error is a dominant factor explaining 2D model depth prediction errors that warrants consideration in model evaluation. It is presumptuous to expect model prediction to be more accurate than topographic deviations, as such, best practices suggest that depth or WSE deviations should not exceed uncertainty in the topographic data (Pasternack, 2011; Pasternack and Senter, 2011; Brown and Pasternack, 2012). The FVA for ground points and bathymetric lidar points in this study were 0.037 m and 0.117 m, respectively (section 3.1), but high topographic variability is likely to yield larger uncertainties. Generally, WSE deviations falling within the range of bathymetric lidar uncertainty were considered suitable for this study. The performance standards reported by Moriasi et al. (2007) for the additional discharge prediction metrics are NSE > 0.5, PBIAS within 25%, and RSR < 0.7, however the exact interpretation of these thresholds in this study remains unclear due to limited use of these metrics in 2D model assessment.

Comparison of lidar based WSEs to 2D model predictions consisted of 147,644 paired data points distributed throughout the 13.2 km study domain, a considerably larger sample size than studies relying solely on field measured WSEs. All deviation statistics were calculated as observed (lidar measured) minus predicted (2D model), meaning that positive deviations represent model WSE and depth under-prediction and negative deviations model WSE and depth over-prediction. Mean signed WSE deviation error (ME) was -0.077 m and mean absolute error (MAE) was 0.162 m. Water surface deviations displayed a near equal balance of over-versus under-predictions with a slight tendency toward 2D model over-prediction, as reflected by the negative ME value (Figure S4a). A majority (53%) of the raw WSE point deviations had less absolute error than the 0.117 m FVA of the bathymetric lidar and 81.6% of the data within 0.25 m, which is close to two times the FVA of the bathymetric lidar (Table S8). Additional metrics from the regression and correlation assessment analysis as well as NSE, PBIAS, and RSR were all within the standards of satisfactory model performance (Table S9).

Locations with the largest WSE over-prediction were dispersed throughout the model domain, but were often clustered upstream of hydraulic controls, specifically in areas of relatively deep water immediately upstream of narrow channel constrictions. Comparison of the complete topographic surface with 2D model computational mesh surfaces revealed a smoothing effect present at many of these constrictions due to the resampling procedure used to create the up-scaled mesh surfaces. This smoothing resulted in reduced channel conveyance and artificially high bed elevations that, when modeled created a backwater effect over-elevating upstream conditions. These simulated backwater conditions help explain the WSE over-prediction in these settings. A qualitative review of the spatial distribution of WSE deviations also revealed that areas of large over-prediction (e.g. model predicted depths were too high) tended to be in locations with low WSE point densities, thus questioning the accuracy of the observed values and making quantitative review of these large errors more difficult.

Review of WSE deviations identified at least 15 locations displaying the physical conditions described above. These locations included 7,743 points with WSE over-prediction deviations greater than 0.1 m and represent ~ 5% of the total WSE comparison dataset. Removal of these points from the WSE assessment dataset ('selected WSE dataset') and re-assessment of WSE deviations improved model predicted WSE descriptive statistics. The ME and MAE for the selected WSE dataset were -0.042 m and 0.132 m, respectively. Similar improvements were observed in the percentage of data meeting several deviation thresholds (Table S8) and other performance metrics (Table S9).

WSE deviations varied longitudinally, illustrating the spatially varying nature of water surface errors (Figure S5). Black points in Figure S5 represent locations of poor model prediction described above. These points coincide with nearly all regions of large model over-prediction and it is likely other areas of over-prediction have similar unidentified topographic controls. Visually, locations of both over- and under- prediction appear to be located in distinct spatially cohesive patches. This grouping of errors as well as the lack of systematic error in WSE deviations may in-part reflect the decision to use a constant roughness coefficient value rather than spatially varied roughness.

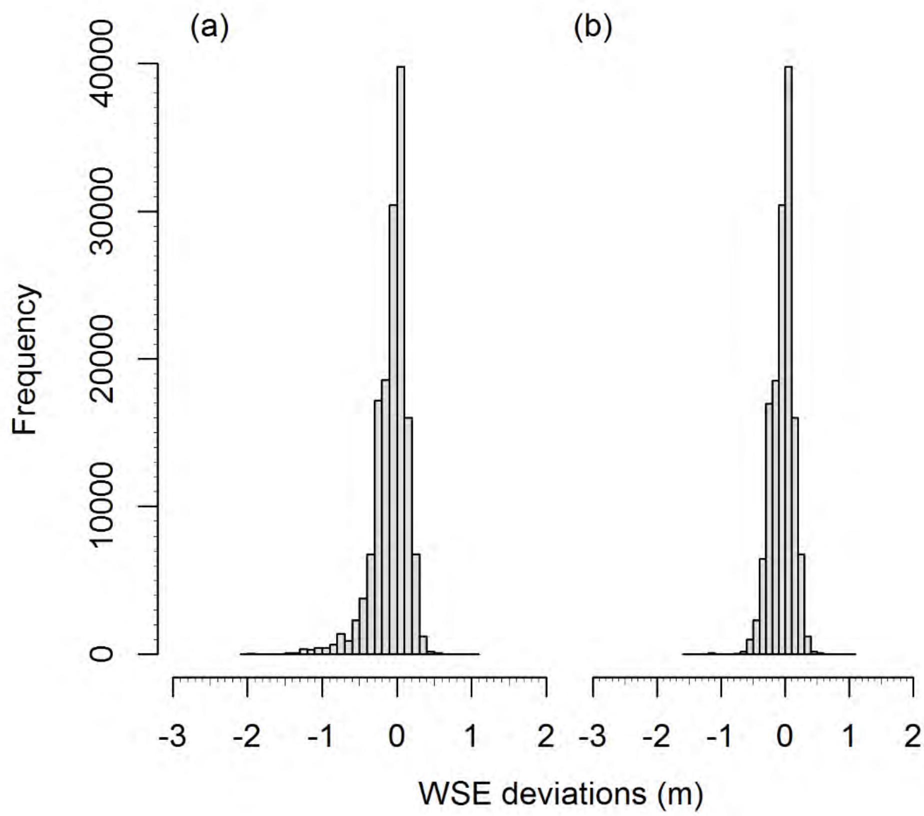

Figure S4. Histograms of 2D model WSE deviations for the (a) entire WSE dataset and (b) selected WSE dataset.

Table S8. Non-exceedance probabilities of WSE deviations meeting different thresholds of performance for entire WSE dataset and selected WSE dataset.

All WSE dataset		Selected WSE dataset	
Absolute WSE deviation (m)	Non-exceedance probability (%)	Absolute WSE deviation (m)	Non-exceedance probability (%)
0.025	13.8	0.025	14.5
0.05	26.6	0.05	28.1
0.1	47.6	0.1	50.2
0.117[a]	52.7	0.117[a]	55.6
0.155[b]	61.7	0.155[b]	65.1
0.25	81.6	0.25	86.0
0.5	95.3	0.5	99.0

[a]Lidar bathymetric FVA

[b]Combined bathymetric and terrestrial lidar FVA

Table S9. Regression and hydrologic metrics for entire WSE dataset and selected WSE dataset assessment.

Test Statistic	All WSE dataset	Selected WSE dataset
n	147644	139901
Regression Slope	1.00	1.00
Regression Intercept	0.06	-0.03
R^2	1.00	1.00
SES	9.9E-06	7.4E-06
SEI	0.00	0.00
ME (m)	-0.08	-0.04
MAE (m)	0.16	0.13
PBIAS	0	0
RSR	3.8E-03	2.8E-03
NSE	1.00	1.00

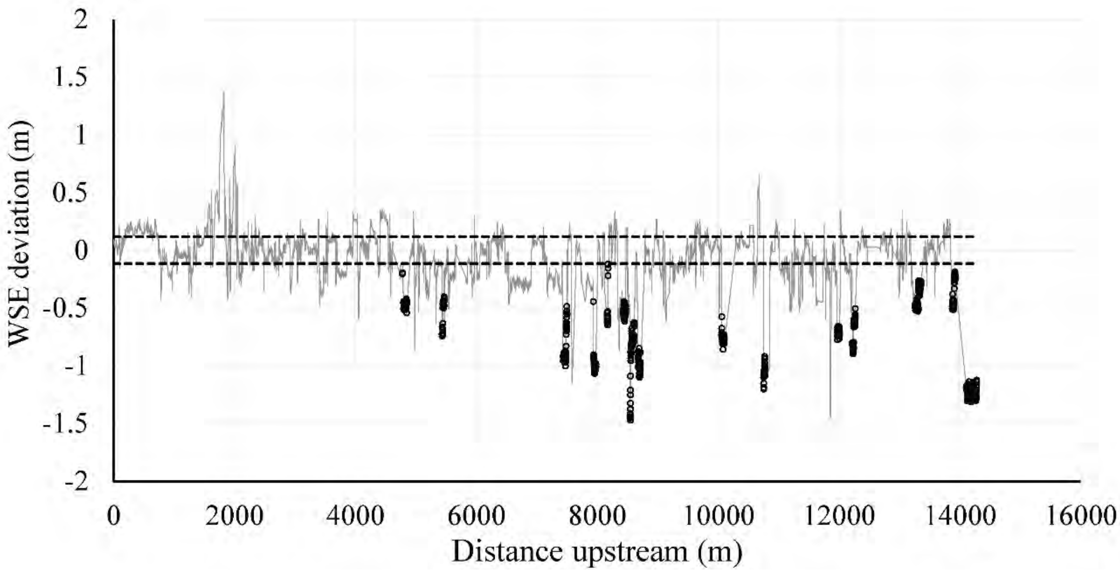

Figure S5. Longitudinal profile of deviation between observed and predicted WSE. Positive deviation corresponds to model under-prediction and negative deviation to model over-prediction. Black dots are areas of poor performance potentially due to topographic uncertainty. Horizontal dashed lines are bathymetric lidar FVA (± 0.117m).

Fixed-point Depth and Velocity

The next test was assessment of the model for fixed-point depth and velocity performance. This test is less relevant toward the study purpose of accurately mapping wetted areas for the simulated discharges, but nonetheless provides a relevant check of model performance. Depth and velocity data were collected on April 8, 2016 at 61 independent locations in the downstream portion of the study site in a location with complex, shallow hydraulics. The discharge corresponding to the period of measurement was estimated as 3.51 m^3/s, herein referred to as the 'velocity assessment' discharge simulation. The data collection strategy used focused on sampling the range of velocities present in the river at this discharge opposed to more traditional cross-section based sampling strategies. This design allows quantitative testing of a model's ability to predict over a range of velocities (Pasternack and

Senter, 2011). Measurements were made with no *a priori* knowledge of the spatial pattern of velocity and prior to model simulation to ensure no sampling bias. Velocity measurements were made in wadable areas using a SonTek FlowTracker Handheld Acoustic Doppler Velocimeter (ADV) mounted to a depth setting wading rod. Depth measurement errors were ±1 cm. Velocity measurement error reported by the manufacturer is ±1% of measured velocity + 0.25 cm/s. Depth-averaged velocities were estimated by sampling velocity at 10 Hz averaged over 20 s at 0.6·depth from the water surface (Pasternack, 2011). The position of each measurement were simultaneously surveyed using RTK-GPS.

Correlation and regression analyses between predicted vs. observed depth and velocity values yielded several variables for evaluation. The coefficient of determination (R^2) metric describes variance about the best fit slope, an indicator of model precision. R^2 values of ~ 0.6 for water speed are common for 2D models with values in the ~ 0.7-0.85 range considered very good (Brown and Pasternack, 2012). R^2 values for depth are typically higher (~ 0.7-0.8) than those for velocity (~0.5-0.8) and values in these ranges are recommended as a minimum standard for model performance (Pasternack, 2011). The accuracy of model predictions is better described by the slope term in the regression equation than R^2 values. A value of unity represents no bias in the model predictions. The y-intercept of the regression equation also indicates potential model bias. Over prediction of low velocities and under prediction of high velocities have been reported in previous 2D modeling studies (Brown and Pasternack, 2012). Based on recommendations by Pasternack (2011) standards for demonstrating model suitability using comparison of predicted vs observed velocity data are a slope term >0.8 and a y-intercept <10% of the maximum observed velocity.

Model accuracy was also evaluated from statistical analysis of unsigned depth and velocity percent error. Mean and/or median velocity errors >50% suggest poor model performance whereas mean and median error values of ~ 10-15% for depth and ~ 15-30% for velocity are considered reasonable (Pasternack, 2011). Percent error for low values often exceed 200% due to the strong influence of even small deviations. To address this issue separate velocity tests for low and high values may be performed with a threshold value between 0.3 m/s to 0.9 m/s used to differentiate velocities (Pasternack, 2011; Brown and Pasternack, 2012; Strom et al., 2016). Depth measurement with a depth setting wading rod as well as RTK-GPS topographic data have much greater point accuracy and probability of being measured directly from the river bed than lidar point data collection. Comparison of lidar derived vs. field observed elevations at the fixed-point depth observation sites were reviewed to address systematic differences that might influence depth measurement uncertainty.

Comparison of model predicted hydraulics (depth and depth-averaged velocity) with field measured estimates showed predicted values closely approximated observed conditions (Table S10). Coefficient of determination (R^2) values between predicted and observed hydraulics were 0.80 for depth and 0.84 for velocity ($p<0.001$ for both tests). Linear regression between predicted and observed values yielded regression slopes of 0.87 for both depth and velocity ($p<0.001$ for both tests) and y-intercepts of 0.04 ($p<0.001$) and 0.03 ($p=0.28$), respectively (Figure S6 and Figure S7). These y-intercept values scale to 2.9% and 2.4% of the maximum observed depth and depth-averaged velocity, consistent with acceptable performance standards.

Regression slopes and intercepts all indicate slight bias toward the model over-predicting depths and velocities. This precludes errors being associated with the selected roughness coefficient, as adjusting this value to improve prediction of one metric would have been at the detriment of the other. Residuals between predicted and observed velocity suggest over-prediction was somewhat more prevalent in slow flowing than faster areas (i.e., 63% of points with velocities less than 0.3 m/s were over-predicted versus only 45% of points with velocities greater than 0.3 m/s), a common occurrence in 2D model performance. Velocity residuals had slight heteroscedasticity further suggesting error dependence on the magnitude of velocity, whereas depth residuals were relatively trendless (Figure S7).

Descriptive statistics comparing observed and predicted values corroborated the findings described above including the tendency to over-predict slow velocities and slightly under-predict fast velocities. The mean percent error (MPE) of all velocity observations regardless of magnitude was -25% (median percent error of -5%), with the negative sign connoting model over-prediction. Velocity points were stratified into bins above and below 0.3 m/s. Low velocity points had a MPE of -48% (median percent error of -17%) and high velocity points a MPE of -1% (median percent error of 4%). Mean absolute percent velocity error (MAPE) for velocities below 0.3 m/s, velocities above 0.3 m/s, and all data were 64%, 20% and 43%, respectively. Median absolute percent error for these same subsets of data were 30%, 19% and 24%, respectively. With the exception of observations in the low velocity bin (i.e., fixed-point velocities < 0.3 m/s) nearly all metrics were within the 20–30% benchmark for this study. In addition to descriptive statistics comparing observed and predicted hydraulics and metrics from the regression and correlation analysis NSE, PBIAS, and RSR values were also all within the standards of satisfactory model performance (Table S10).

Table S10. Regression and hydrologic metrics for fixed-point depth and velocity assessment.

Test Statistic	Fixed-point depth	Fixed-point velocity
n	60	61
Regression Slope	0.87	0.87
Regression Intercept	0.04	0.03
R^2	0.80	0.84
SES	0.06	0.05
SEI	0.05	0.02
MPE (%)	-6.0	-25.4
MAPE (%)	9.0	43.1
PBIAS	8.8	6.1
RSR	0.54	0.43
NSE	0.70	0.82

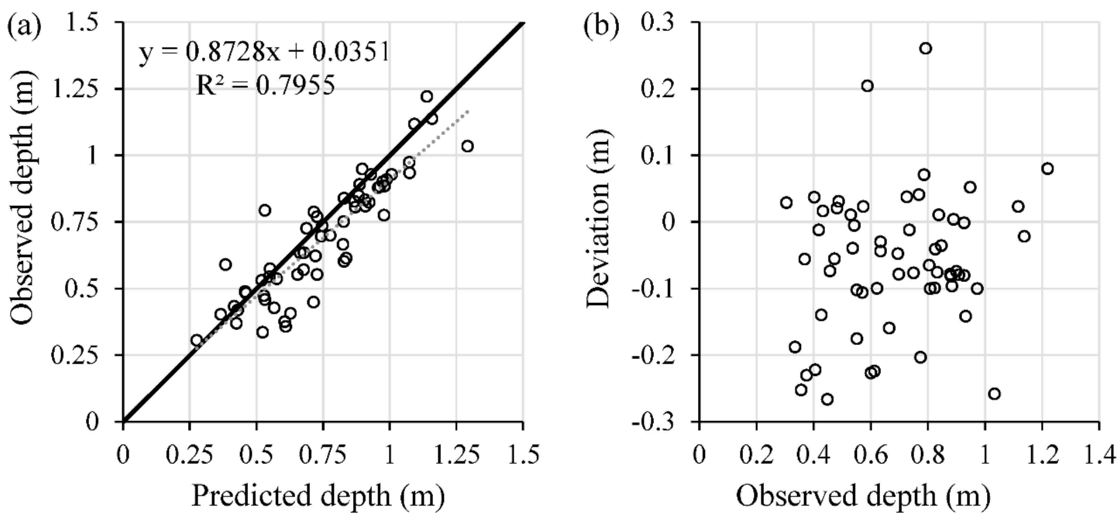

Figure S6. (a) Scatter plot of observed versus 2D model predicted depth with 1:1 line (dark black line), line of best fit (gray dashed line) as well as equation of best fit line and coefficient of determination and (b) deviations between observed and predicted depth versus observed depth.

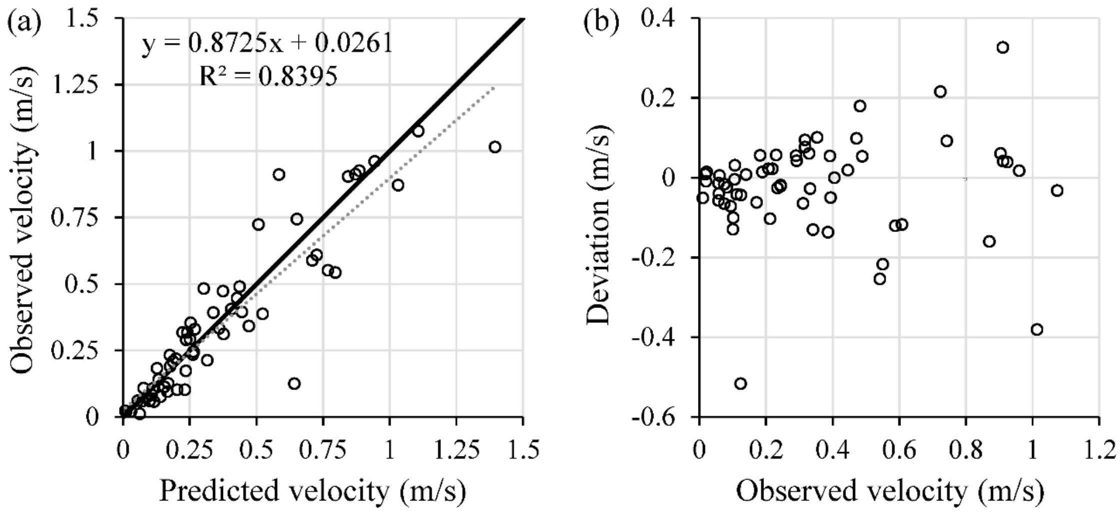

Figure S7. (a) Scatter plot of observed versus 2D model predicted velocity with 1:1 line (dark black line), line of best fit (gray dashed line) as well as equation of best fit line and coefficient of determination and (b) deviations between observed and predicted depth versus observed depth.

3.4.2 2D model roughness sensitivity

The scale of model sensitivity to large (> 0.01) variations in n values was tested through studying changes of model predicted depths and velocities. Lidar baseline flow simulation results were compared using variable roughness coefficient values of 0.07, 0.08, 0.09, and 0.10, respectively. For each pair of simulations (e.g. a simulation with n=0.07 was compared to simulations with n=0.08, n=0.09, and n=0.10), differences in predicted depths at all nodes that were wet in both simulations were computed. The same was done for velocity. Average deviations for both variables were computed for each simulation pairing and trends were assessed. This analysis was repeated for the velocity assessment discharge simulation and a more limited analysis comparing n values of 0.09 and 0.10 was performed for a wider range of discharges (those listed in Table S6 and 2.68, 32.20, and 160.98 m^3/s).

Average sensitivity of predicted depth and velocity at the lidar baseline discharge to the range of tested roughness values were well described by a linear model fit using least squares (R^2 values of 1.0 and 0.98, respectively, $p<0.10$). Similar linear scaling was also observed for the velocity assessment discharge simulation of 3.51 m^3/s (R^2 values of 1.0 and 0.98 for depth and velocity sensitivity, respectively, $p<0.10$). While these results are based on a small number of samples (six data points), the findings encourage the assumption that average model sensitivity to changes in Manning's n scaled linearly regardless of discharge (i.e., there was a constant magnitude change in average predicted depth and velocity per 0.01 unit change in Manning's n for each discharge). Average sensitivity of model predicted depths and velocities to increase in Manning's n of 0.01 (e.g. average change in hydraulics going from 0.08 to 0.09 or 0.09 to 0.1) for the range of simulated discharges are depicted in Figure S8. Sensitivities are generally small and represent only a small portion of average hydraulic conditions. For example, although model sensitivity is greater at higher discharges, average depth and velocity conditions also increase with discharge and the ratio of sensitivity to predicted depths and velocities was between 2-3% of average conditions for all discharges. In essence it would take large changes in roughness values to markedly change bulk predicted hydraulics, though large local affects are certainly possible that were not captured by this limited analysis.

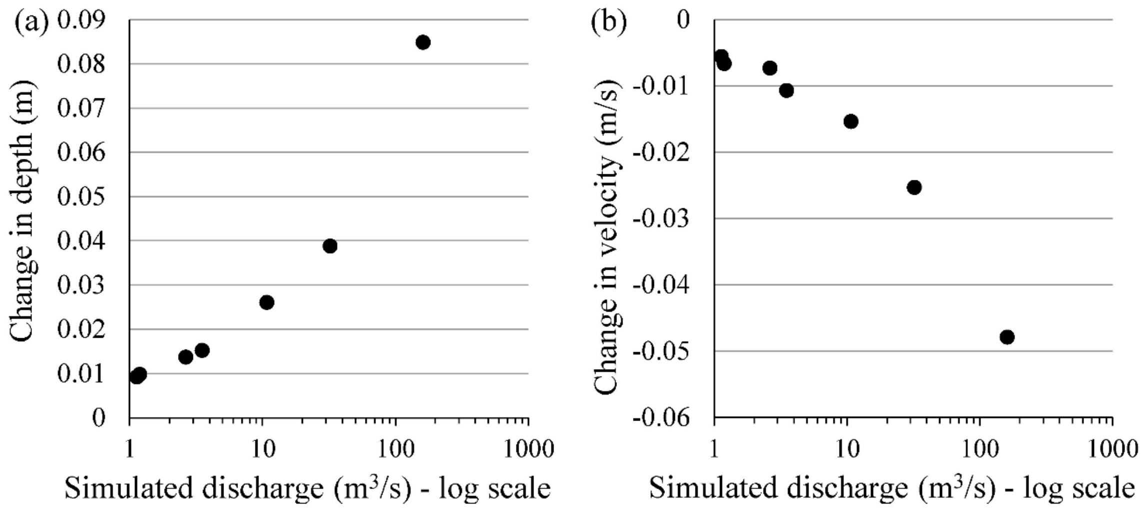

Figure S8. Semi-log plot of 2D Model average (a) depth and (b) velocity sensitivity to an increase in Manning's n of 0.01 over various simulated discharges.

3.5. LBE spatial analysis

The heterogeneous and hierarchical nature of the study site, like essentially all rivers, required implementation of a disaggregation and aggregation procedure (Alber and Piegay, 2011) to allow longitudinal analysis of river characteristics at appropriate scales. Spatial disaggregation and aggregation was accomplished using a box counting procedure described by Wyrick and Pasternack (2012). Simplistically, the procedure involves generating points longitudinally along a river centerline, creating station-lines perpendicular to these points, and buffering the station lines into individual polygons that are then clipped to the wetted area or other boundary of interest.

The disaggregation and aggregation process is sensitive to the location and tortuosity of the alignment used to generate the longitudinal series of points. An overly tortuous path results in highly overlapping sections and polygons that also miss covering portions of the wetted area, while an overly simple alignment such as using a valley centerline for interpretation of all flows may result in clipped polygons that are not perpendicular to the main direction of flow, particularly at lower flows. To address this issue two longitudinal alignments were generated based on the centerlines of the bankfull (10.73 m^3/s) and max flood flow (343.6 m^3/s) simulations. Centerlines were delineated using the Polygon Centerline Tool™ (https://www.beachbumgis.com/). The bankfull alignment was used to generate cross-sectional polygons for all simulated flows below bankfull (10.7 m^3/s) and the max flood flow alignment was used for all remaining flows. Prior to applying the box counting procedure the bankfull and flood flow centerlines were simplified using the ArcGIS simplify line (point remove algorithm with 4.6 m offset) and smooth line (Bezier interpolation) tools. Points were spaced along the revised alignments every 3 m, yielding a series of 3-m cross-sectional polygons distributed down the river for each simulated discharge. Notably there was some overlap or underlap of rectangles at locations of high channel curvature. These areas were determined to balance out and no manual adjustment of the polygons occurred.

As discussed in the main text, a path-based approach was developed for the LBE-to-LBE spacing analysis to estimate longitudinal distances (λ^l) between each LBE and downstream LBEs. In the first step, the unique centerline for each simulated wetted area was repeatedly offset by 1.5 m on each side until the entire wetted area of each discharge was covered with paths (e.g. a new offset would be completely outside the wetted area), thus creating a set of longitudinal paths parallel to the bulk flow direction for each flow simulation. Paths were clipped to each wetted area and vertices were added along paths to densify vertex spacing to a maximum of 0.25 m. Each vertex was assigned its projected coordinates (x,y) and a binary code if it fell within a

LBE (1) or not (0). Distances along paths between each upstream LBE and all downstream LBEs where a contiguous path was present were computed. If no downstream LBE was encountered the calculation was left blank for that LBE. Other factors considered in the calculations included that an LBE could be downstream of itself and that multiple paths and associated spacing values could exist from an upstream LBE to one or more downstream LBEs. These were considered to accurately reflect field conditions and not conflict with the goals of the analysis. Zero spacing values were not supported by the calculation. Instead, abutting LBEs were assigned the distance between sequential vertices resulting in a maximum error equal to the maximum spacing interval (0.25 m). The maximum error in λ^l values for non-abutting LBEs was twice the maximum vertex spacing (0.5 m). Both these errors were unlikely worst-case scenarios given vertex densities were often less than the maximum spacing. Very long spacings were also rare given that most paths either encountered an LBE or terminated at a channel margin.

4. Results

4.1. Question 1 results (LBE mapping)

As stated in the main text, qualitative assessment of the 14 smoothed ground surfaces determined certain parameter sets performed better than others. Generally, larger step sizes (~3 and 4.5 m), smaller spike and offset values (0.128 m [D_{50}] and 0.064 m [D_{16}] verses 0.5 m), and intermediate down-spike values (0.128 m, 0.256 m, and 0.15 m) in the ground classification algorithm were best at filtering-out LBEs while maintaining character of the overall terrain (Table S3).

Results of the quantitative assessment of preliminary LBEs mapped from the best six smoothed surfaces are depicted in Table S11. Based on the global performance metric, P-LBE-10 was found to perform best, making the associated RSM the study's preferred RSM. Performance metrics of all 44 LBE_p datasets from the five LBE extraction approaches are presented in Table S12.

Table S11. Performance metrics of predicted LBEs for six selected parameter combinations. Maximum values for each metric highlighted in light-gray and bolded and minimum values are italicized. Preferred dataset in red font.

ID	Minimum vertical threshold (m)	PA	PO	MJI	MER	Normalized mean
P-LBE-1	0.23	*0.794*	*0.680*	**0.212**	**0.017**	0.500
P-LBE-3	0.28	0.822	0.690	0.161	0.011	*0.349*
P-LBE-10	0.28	0.836	0.696	0.183	0.014	**0.552**
P-LBE-11	0.41	**0.864**	**0.737**	*0.107*	*0.009*	0.500
P-LBE-12	0.32	0.833	0.707	0.153	0.010	0.401
P-LBE-13	0.32	0.830	0.706	0.149	0.010	0.372

Table S12. Performance metrics of all 44 predicted LBE datasets. Maximum values for each metric for each approach are highlighted in light-gray and bolded while minimum values are italicized. Global maximum values for each metric are highlighted in dark-gray, bolded and underlined while global minimums are italicized and underlined. Preferred dataset in red font.

ID	PA	PO	MJI	MER	Normalized mean
(i) RSM with vertical threshold					
V-1	**0.894**	**0.774**	*0.269*	*0.030*	*0.445*
V-2	0.876	0.759	0.284	0.034	0.451
V-3	0.856	0.747	0.311	0.038	0.474
V-4	0.839	0.735	0.339	0.043	0.500
V-5	0.822	0.722	0.347	0.048	0.505
V-6	0.802	0.709	0.352	0.054	0.505
V-7	0.785	0.696	0.358	0.059	0.509
V-8	0.755	0.687	0.361	0.065	0.509
V-9	0.732	0.675	0.365	0.072	0.513
V-10	0.703	0.665	0.369	0.079	0.516
V-11	*0.669*	*0.659*	**0.371**	**0.086**	**0.521**
V-12	0.816	0.718	0.351	0.050	0.507
(ii) Gaussian filtered RSM with vertical threshold					
GV-1	**0.760**	*0.705*	**0.333**	0.054	**0.458**
GV-2	0.642	0.762	0.298	0.051	0.409
GV-3	0.611	0.779	*0.246*	0.051	*0.352*
GV-4	0.757	0.706	0.332	**0.054**	0.457
GV-5	0.600	0.789	0.309	0.049	0.423
GV-6	*0.514*	**0.842**	0.315	*0.045*	0.426
(iii) RSM with MCWS algorithm and constant window size					
MCWS-C-1	**0.901**	0.837	0.422	*0.018*	0.647
MCWS-C-2	0.760	0.789	0.445	0.046	0.645
MCWS-C-3	0.828	0.763	0.453	0.050	0.676
MCWS-C-4	0.825	0.827	0.432	0.025	0.630
MCWS-C-5	0.772	0.774	0.455	0.061	0.700
MCWS-C-6	*0.742*	0.727	**0.469**	**0.087**	**0.740**
MCWS-C-7	0.819	0.752	0.456	0.063	0.708
MCWS-C-8	0.798	*0.715*	0.464	0.083	0.738
MCWS-C-9	0.879	**0.838**	*0.374*	0.019	0.586
MCWS-C-10	0.809	0.828	0.392	0.025	*0.581*
(iv) RSM with MCWS algorithm and variable window size					
MCWS-V-1	**0.760**	*0.715*	**0.460**	*0.083*	*0.714*
MCWS-V-2	*0.756*	**0.720**	*0.450*	**0.086**	**0.718**

ID	PA	PO	MJI	MER	Normalized mean
(v) Gaussian filtered RSM with MCWS and constant window size					
GV-MCWS-C-1	0.886	0.854	0.402	0.017	0.629
GV-MCWS-C-2	0.847	0.858	0.384	0.019	0.600
GV-MCWS-C-3	0.712	*0.810*	0.436	0.057	**0.674**
GV-MCWS-C-4	0.608	0.838	**0.440**	0.063	0.673
GV-MCWS-C-5	0.691	0.815	0.431	0.058	0.665
GV-MCWS-C-6	0.593	0.842	0.433	0.063	0.663
GV-MCWS-C-7	0.840	0.859	0.379	0.019	0.594
GV-MCWS-C-8	**0.893**	0.863	0.393	*0.015*	0.627
GV-MCWS-C-9	0.829	0.870	0.358	0.018	0.570
GV-MCWS-C-10	0.657	**0.894**	0.361	0.035	0.572
GV-MCWS-C-11	0.501	0.870	0.399	0.065	0.614
GV-MCWS-C-12	*0.416*	0.887	0.393	**0.075**	0.617
GV-MCWS-C-13	0.479	0.860	0.403	0.074	0.627
GV-MCWS-C-14	0.780	0.874	*0.339*	0.020	*0.535*

4.2. LBE concentrations

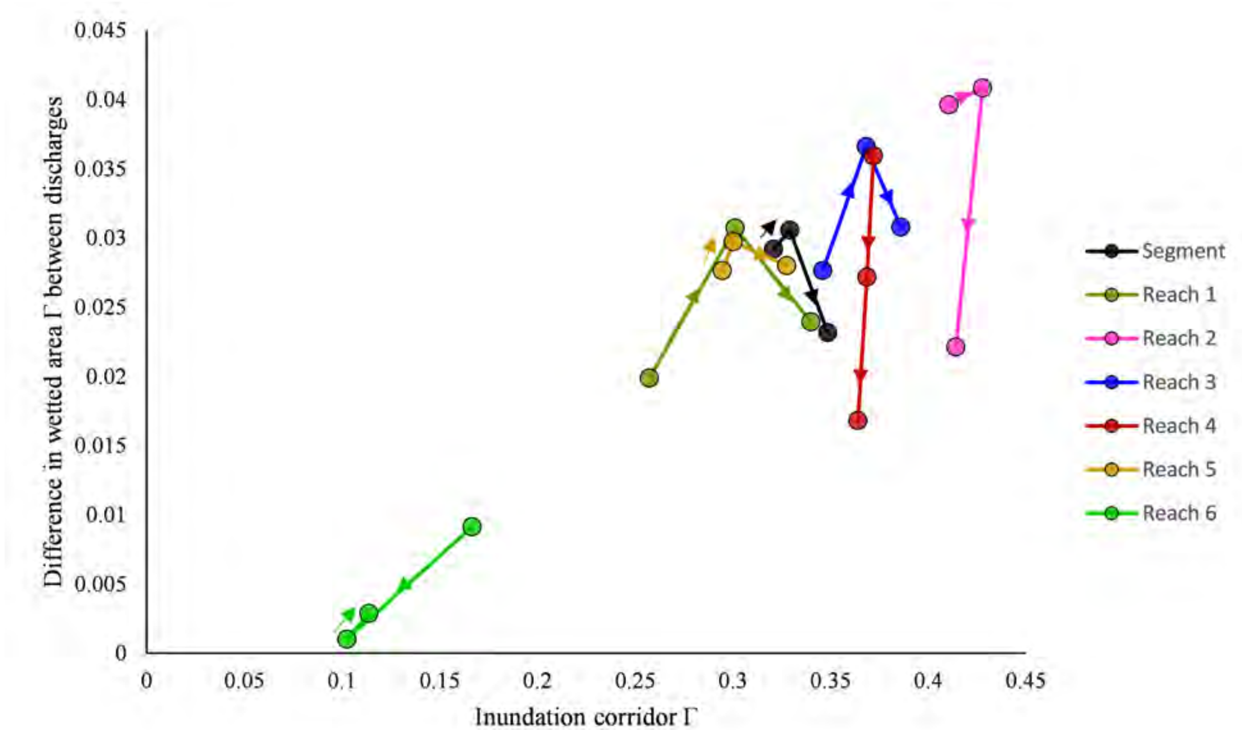

Figure S9. Difference in wetted area Γ between discharges versus inundation corridor Γ. Data are colored by reach. Lines with arrows between points indicate direction of increasing discharges from data points associated with 10.73 to 82.12 to 343.6 m^3/s. Some arrows have been offset for visual purposes.

4.3. LBE spacings

As stated in the main text, distributions of discharge-dependent streamwise spacing metrics were positively skewed and indicated a strong tendency for closely spaced LBEs. Histograms of λ^l, λ_*^l, and $\widehat{\lambda_*^l}$ distributions are depicted in **Figure S10**.

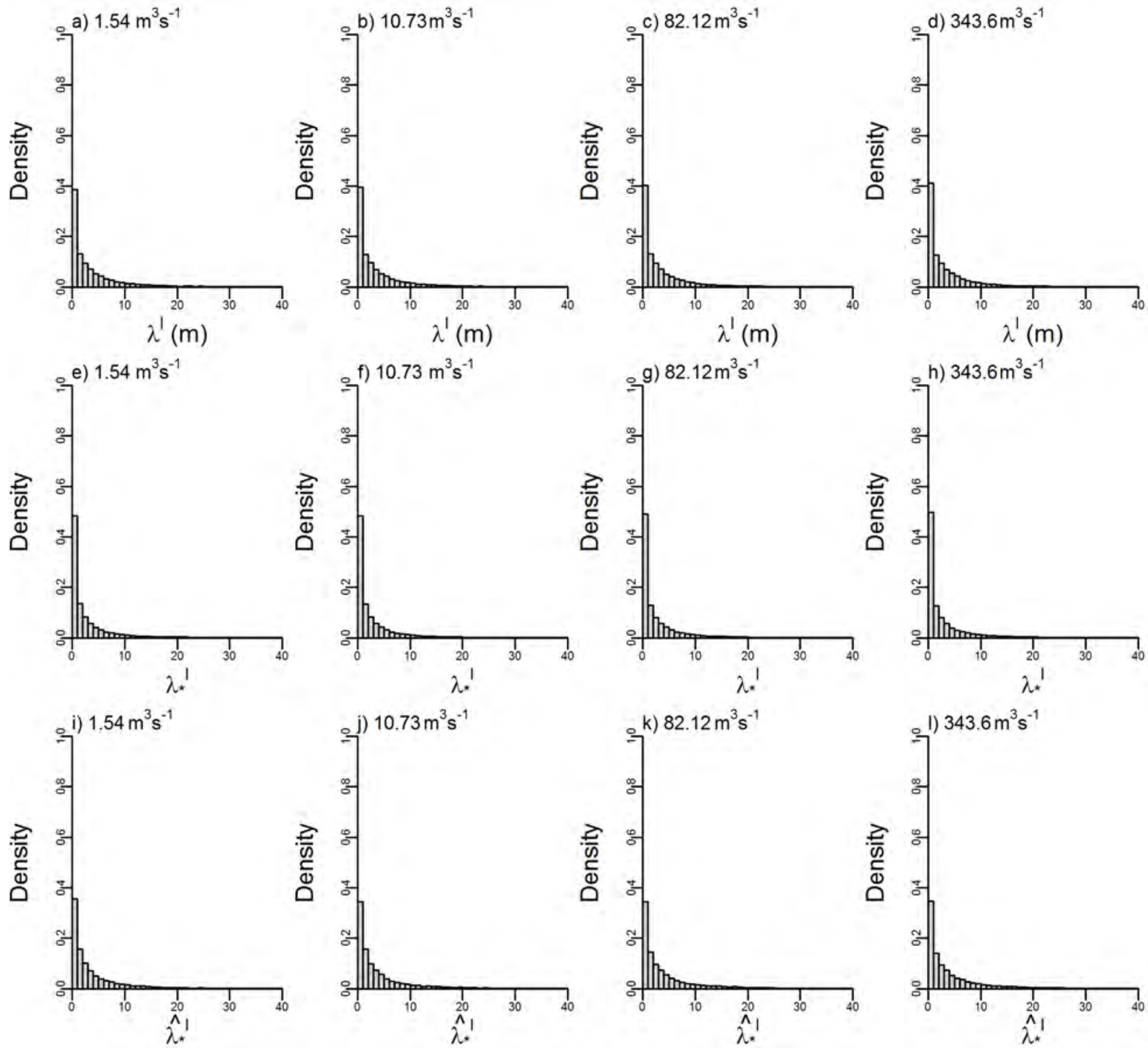

Figure S10. Histograms of streamwise spacing metrics (a-d) $\boldsymbol{\lambda^l}$, (e-h) $\boldsymbol{\lambda^l_*}$, and (i-l) $\widehat{\boldsymbol{\lambda^l_*}}$ for discharge-dependent LBEs. For visual purposes X-axis values have been truncated to a maximum value of 40 despite higher values occurring.

4.4. Question 2 results (maximum resistance)

None.

4.5. Comparing hydrodynamic regimes from concentration and spacing metrics

As stated in the main text, comparison of cross-sections classified into Morris's (1959) hydrodynamic regimes using $\overline{\lambda_*^l}$ and Γ found only 44% sections were classified the same by each method. Table S13 depicts a complete confusion matrix of how cross-sections were classified according to each metric for each discharge-dependent LBE dataset.

Visualizing distributions of cross-sectional LBE counts found data were more distinct between hydrodynamic regimes classified by Γ compared to regimes classified by $\overline{\lambda_*^l}$, the former showing clear stepwise increases in the number of LBEs per cross-section when going from isolated flow to wake interference to skimming flow, whereas the latter had more uniform counts across regimes (Figure S11). Similar, albeit more muted patterns, were observed comparing distributions of cross-sectional median LBE areas (Figure S12).

Comparing LBE count and median LBE area distributions of similarly classified cross-sections with those having the three most common classification discrepancies (i.e., Γ-based wake interference sections classified as isolated roughness and skimming flow regimes according to $\overline{\lambda_*^l}$, and Γ-based skimming flow sections classified as wake interference according to $\overline{\lambda_*^l}$), several patterns emerged. Firstly, LBE counts of sections classified as wake interference by Γ but as isolated roughness or skimming flow by $\overline{\lambda_*^l}$ were lower than for similarly classified sections (i.e. both in wake interference regime) (Figure S13). Median LBE areas were also lower for $\overline{\lambda_*^l}$-based isolated roughness sections and higher for $\overline{\lambda_*^l}$-based skimming flow sections compared to similarly classified sections (Figure S14). This result is what would be expected, but together with LBE count data suggests $\overline{\lambda_*^l}$-based isolated roughness classification discrepancies might have been driven by lower numbers of smaller LBEs with longer downstream spacings compared to similarly classified sections, and that $\overline{\lambda_*^l}$-based skimming flow classification discrepancies might have been driven by lower numbers of larger LBEs with shorter downstream spacings.

Comparing Γ-based skimming flow sections classified as wake interference by $\overline{\lambda_*^l}$ found LBE counts to be higher and LBE medians areas to be lower than sections classified the same by both metrics (i.e. both in skimming flow regime) (Figure S13 and Figure S14). This suggests larger numbers of smaller LBEs were present in dissimilar sections relative to similar sections, which does not point to clear reasons for the discrepancies. Notably these sections had higher LBE counts and median areas than sections classified in the wake regime by both metrics, which supports the Γ-based skimming flow classification and again suggests there may be uncertainty with the $\overline{\lambda_*^l}$ metric.

Table S13. Confusion matrix of the number of cross-sections classified into each of Morris's (1959) hydrodynamic regimes using $\boldsymbol{\overline{\lambda_*^l}}$ (columns) and Γ (rows) values for each discharge-dependent LBE dataset. Numbers along diagonals were classified the same by both metrics. Abbreviations are such that: IF – isolated roughness; WI – wake interference; and SF – skimming flow.

(a) 1.54 m³/s		$\widehat{\lambda_*^l}$		
		IF	WI	SF
Γ	IF	509	165	182
	WI	780	743	619
	SF	203	381	654

(b) 10.79 m³/s		$\widehat{\lambda_*^l}$		
		IF	WI	SF
Γ	IF	397	134	129
	WI	796	806	569
	SF	197	512	696

(c) 82.12 m³/s		$\widehat{\lambda_*^l}$		
		IF	WI	SF
Γ	IF	279	83	48
	WI	891	875	468

(d) 343.6 m³/s		$\widehat{\lambda_*^l}$		
		IF	WI	SF
Γ	IF	179	53	28
	WI	944	896	341

	SF	216	661	668

	SF	250	790	708

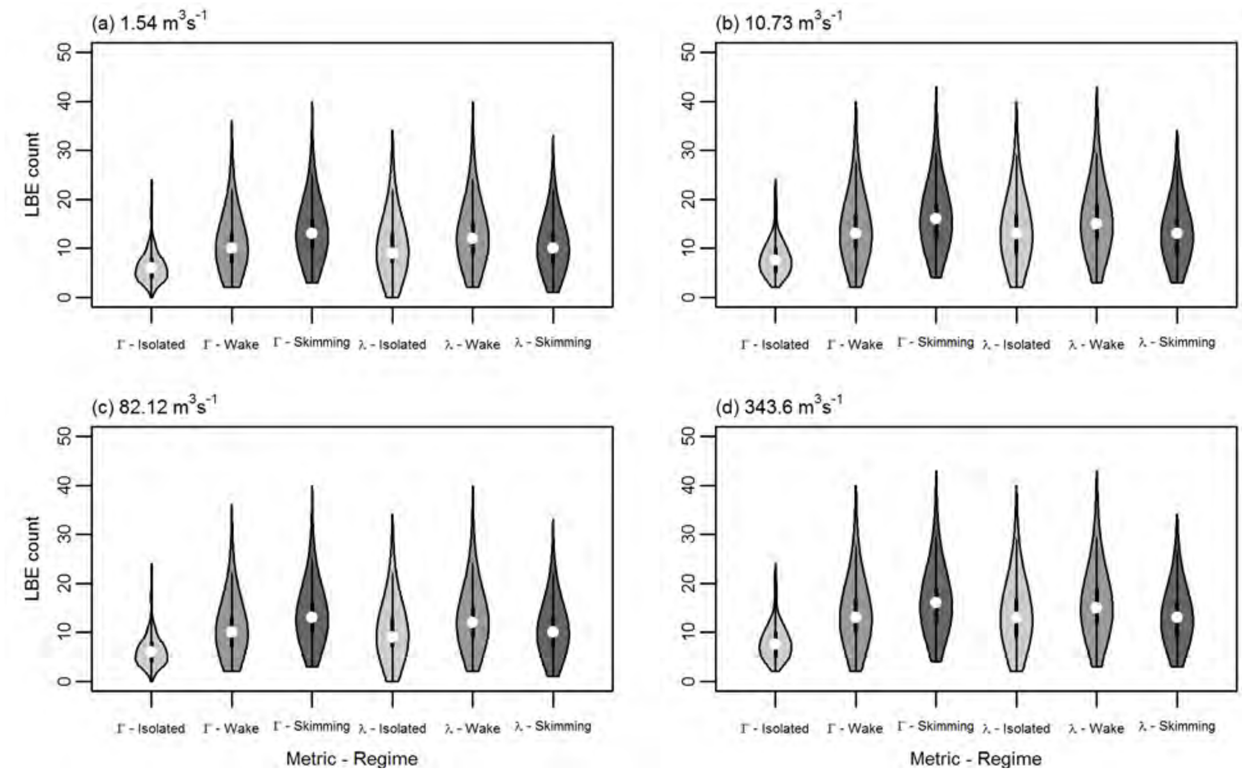

Figure S11. Violin plots of LBE count distributions for cross-sections classified into each of the three hydrodynamic regimes using Γ and $\overline{\boldsymbol{\lambda}_*^{l}}$ values for each discharge-dependent LBE dataset.

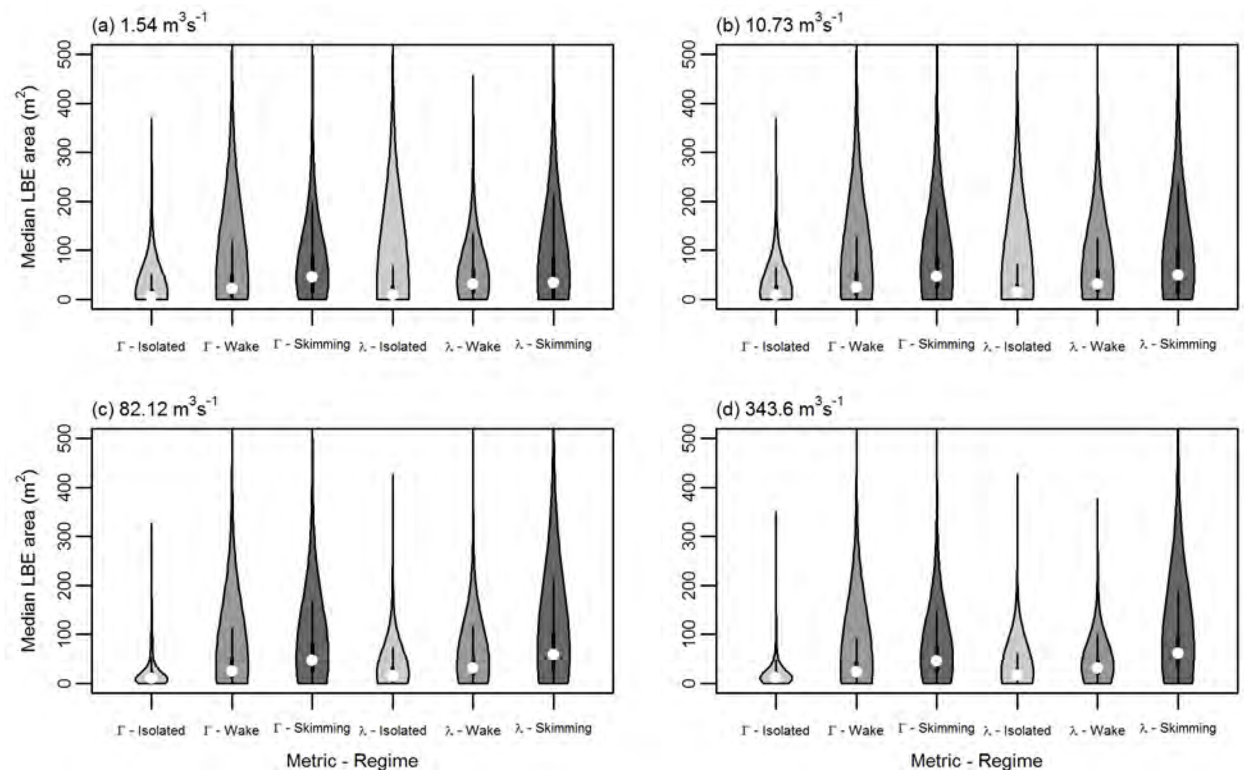

Figure S12. Violin plots of median LBE area distributions for cross-sections classified into each of the three hydrodynamic regimes using Γ and $\overline{\boldsymbol{\lambda}_*^l}$ values for each discharge-dependent LBE dataset.

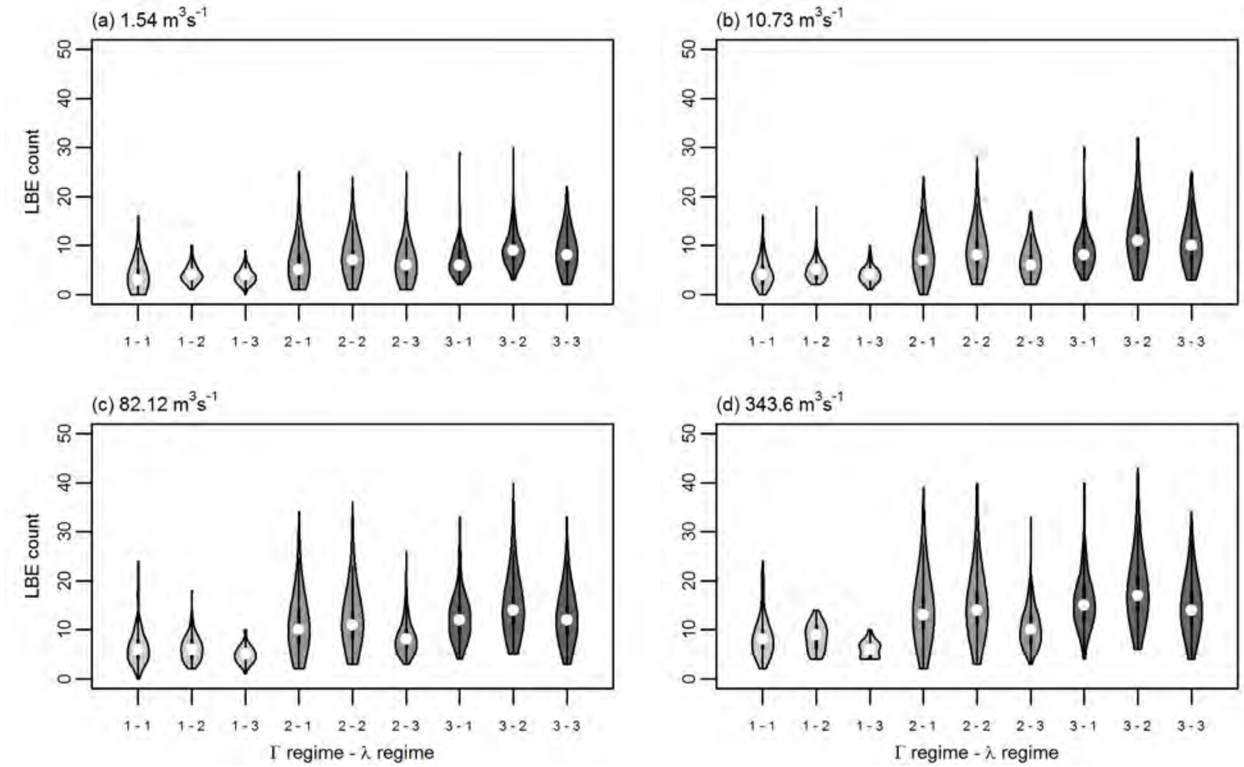

Figure S13. Violin plots of cross-sectional LBE count distributions for each discharge-dependent LBE dataset stratified by how sections were classified into hydrodynamic regimes by both Γ and $\overline{\boldsymbol{\lambda}_*^{l}}$ values. X-axis values are unique codes for all possible regime classification combinations. The first number corresponds to the Γ-based regime classification and the second number to the $\overline{\boldsymbol{\lambda}_*^{l}}$-based regime classification. Values are coded as follows: 1 – isolated roughness; 2 – wake interference; and 3 – skimming flow.

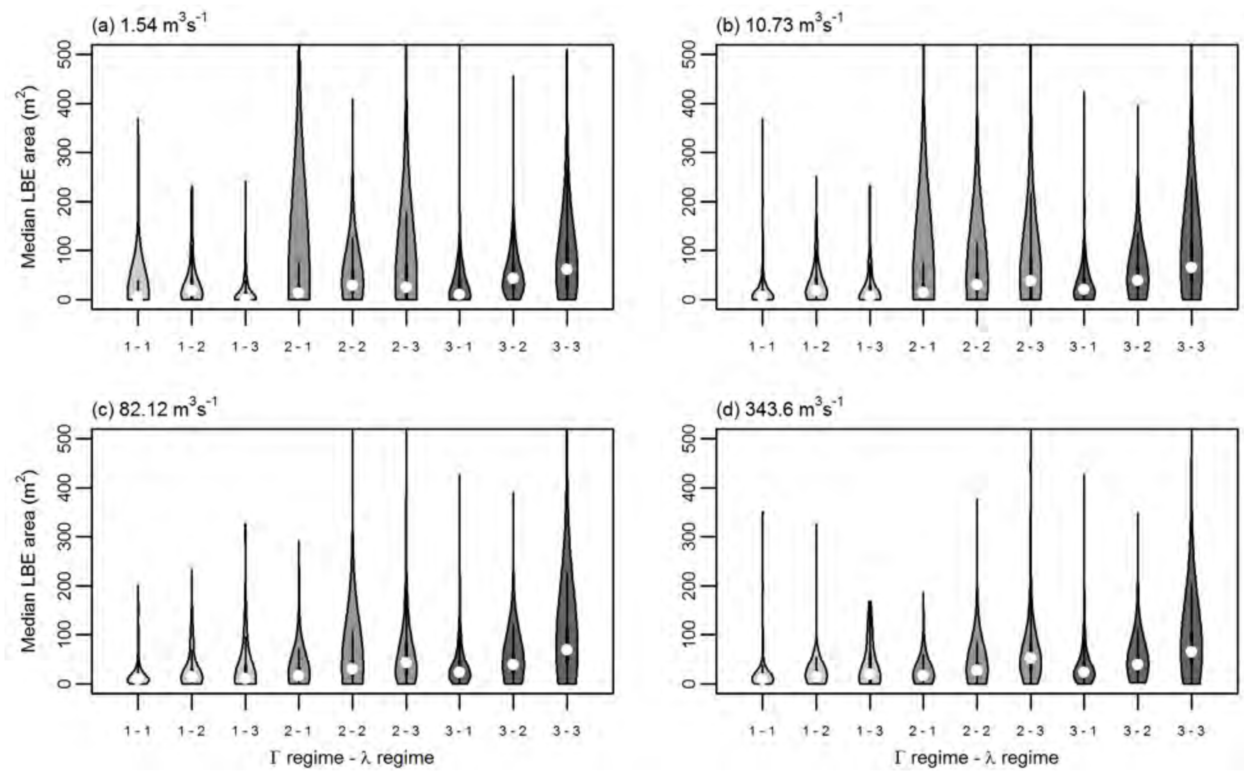

Figure S14. Violin plots of cross sectional LBE median area distributions for each discharge-dependent LBE dataset stratified by how sections were classified into hydrodynamic regimes by both Γ and $\overline{\boldsymbol{\lambda}_*^l}$ values. X-axis values are unique codes for all possible regime classification combinations. The first number corresponds to the Γ-based regime classification and the second number to the $\overline{\boldsymbol{\lambda}_*^l}$-based regime classification. Values are coded as follows: 1 – isolated roughness; 2 – wake interference; and 3 – skimming flow.

4.6. Question 3 results (LBE lateral structure)

None.

5. Discussion

5.1. Mapping LBEs in a mountain river

None.

5.2. LBE lateral spatial structure and resistance

None.

5.3. Segment and reach resistance maximization

None.

5.4. Cross-section resistance maximization

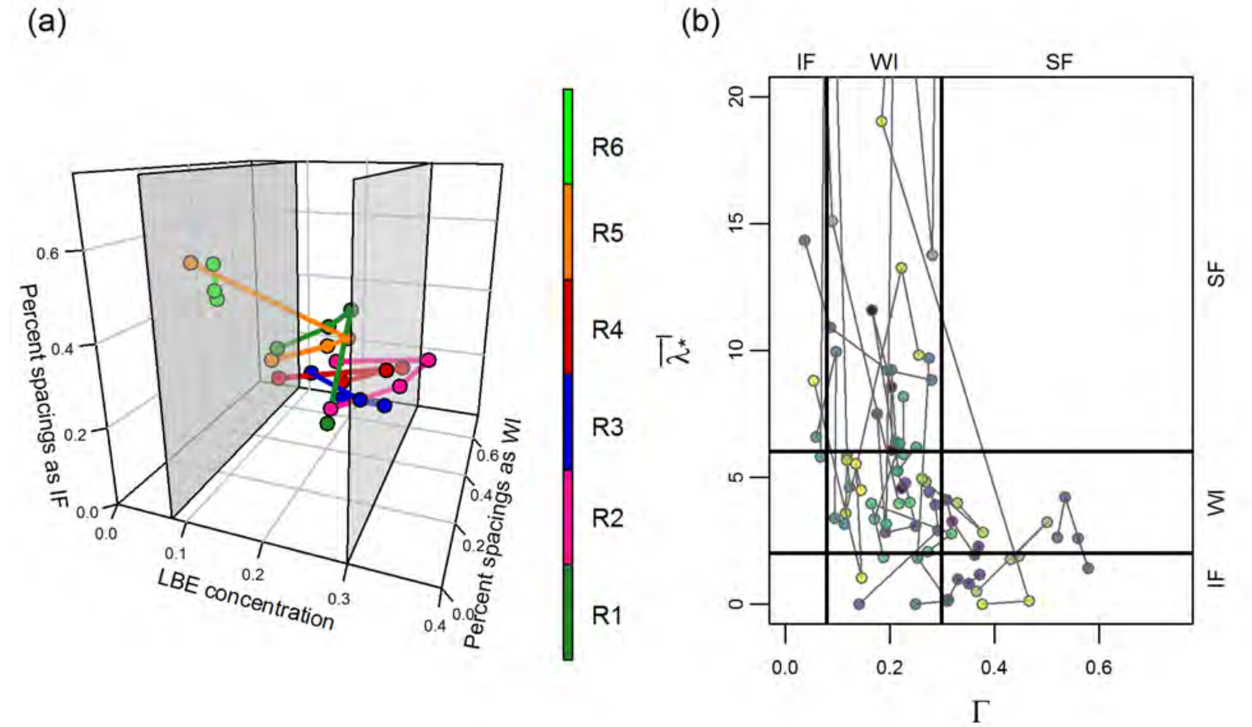

Figure S15. (a) 3D phase-space showing reach-scale Γ (x-axis) and percentage of $\widehat{\lambda}_*^l$ values classified as WI (y-axis) and IF (z-axis). Vertical gray planes are Γ thresholds for Morris's hydrodynamic regimes. Regime thresholds for spacing were not able to be shown on this phase-phase, but can be inferred from the two spacing dimensions. (b) 2D phase-space showing cross-section scale Γ and $\overline{\lambda}_*^l$ values for 20 randomly selected cross-sections. Vertical and horizontal bold dark lines are thresholds for Morris's hydrodynamic regimes. Abbreviations are such that: R – Reach; IF – isolated roughness; WI – wake interference; and SF – skimming flow.

5.5. Resistance maximization as an attractor state

None.

6. Conclusions

None.

7. References

Abu-Aly, T.R., Pasternack, G.B., Wyrick, J.R., Barker, R., Massa, D., Johnson, T., 2014. Effects of LiDAR-derived, spatially distributed vegetation roughness on two-dimensional hydraulics in a gravel-cobble river at flows of 0.2 to 20 times bankfull. Geomorphology, 206, 468-482. http://dx.doi.org/10.1016/j.geomorph.2013.10.017

Alber, A., Piégay, H., 2011. Spatial disaggregation and aggregation procedures for characterizing fluvial features at the network-scale: Application to the Rhône basin (France). Geomorphology, 125(3), 343-360. https://doi.org/10.1016/j.geomorph.2010.09.009

Andersen, H.E., Reutebuch, S.E., Schreuder, G.F., 2001. Automated individual tree measurement through morphological analysis of a lidar-based canopy surface model. Proceedings of the First International Precision Forestry Symposium, 11–22. June 17–20, 2001, Seattle, WA.

Argamosa, R.J.L., Paringit, E.C., Quinton, K.R., Tandoc, F.A.M., Faelga, R.A.G., Ibañez, C.A.G., . . . Zaragosa, G.P., 2016. Fully automated GIS-based individual tree crown delineation based on curvature values from a LIDAR derived canopy height model in a coniferous plantation. Int. Arch. Photogramm. Remote Sens. Spatial Inf. Sci., XLI-B8, 563-569. doi:10.5194/isprs-archives-XLI-B8-563-2016

Attal, M., Mudd, S.M., Hurst, M.D., Weinman, B., Yoo, K., Naylor, M., 2015. Impact of change in erosion rate and landscape steepness on hillslope and fluvial sediments grain size in the

Feather River basin (Sierra Nevada, California). Earth Surf. Dynam., 3(1), 201-222. doi:10.5194/esurf-3-201-2015

Baiamonte, G., Ferro, V., 1997. The influence of roughness geometry and Shields parameter on flow resistance in gravel-bed channels. Earth Surface Processes and Landforms, 22(8), 759-772. doi:10.1002/(sici)1096-9837(199708)22:8<759::aid-esp779>3.0.co;2-m

Barnes, C., Balzter, H., Barrett, K., Eddy, J., Milner, S., Suárez, J.C., 2017. Individual Tree Crown Delineation from Airborne Laser Scanning for Diseased Larch Forest Stands. Remote Sens. 9, 231. https://doi.org/10.3390/rs9030231

Barsi, Á., Kugler, Z., László, I., Szabó, G., Abdulmutalib, H.M., 2018. Accuracy Dimensions in Remote Sensing. International Archives of the Photogrammetry, Remote Sensing and Spatial Information Sciences, 42.3, 61. doi:10.5194/isprs-archives-XLII-3-61-2018

Bathurst, J.C., 1978. Flow resistance of large-scale roughness. J. Hydraul. Div. ASCE 104 (12), 1587–1603. https://doi.org/10.1061/JYCEAJ.0005114

Bathurst, J.C., 1985. Flow Resistance Estimation in Mountain Rivers. Journal of Hydraulic Engineering, 111(4), 625-643. doi:10.1061/(ASCE)0733-9429(1985)111:4(625)

Bathurst, J.C., Graf, W.H., Cao, H.H., 1987. Bed load discharge equations for steep mountain rivers, in: Thorne, C.R., Bathurst, J.C., Hey, R.D. (Eds), Sediment Transport in Gravel-bed Rivers, Wiley, New York, pp. 453–477.

Benda, L., 1990. The influence of debris flows on channels and valley floors in the Oregon Coast Range, U.S.A. Earth Surface Processes and Landforms, 15(5), 457-466. doi:10.1002/esp.3290150508

Benda, L., Dunne, T., 1997. Stochastic forcing of sediment routing and storage in channel networks. Water Resources Research, 33(12), 2865-2880. doi:10.1029/97wr02387

Beucher, S., Meyer, F., 1993. The morphological approach to segmentation: the watershed transformation, in: Dougherty, E., Thompson, B.J. (Eds), Mathematical morphology in image processing, CRC Press, Florida, 433-481.

Billi, P., 1988. A note on cluster bedform behaviour in a gravel-bed river. CATENA, 15(5), 473-481.https://doi.org/10.1016/0341-8162(88)90065-3

Brayshaw, A.C., 1985. Bed microtopography and entrainment thresholds in gravel-bed rivers. GSA Bulletin, 96(2), 218-223. doi:10.1130/0016-7606(1985)96<218:bmaeti>2.0.co;2

Brown, R.A., Pasternack, G.B., 2008. Engineered channel controls limiting spawning habitat rehabilitation success on regulated gravel-bed rivers. Geomorphology, 97(3-4), 631-654. doi:10.1016/j.geomorph.2007.09.012

Brown, R.A., Pasternack, G.B., 2012. Monitoring and assessment of the 2010-2011 gravel/cobble augmentation in the Englebright Dam Reach of the lower Yuba River, CA. Prepared for the U.S. Army Corps of Engineers, Sacramento District. University of

California at Davis, Davis, CA. http://pasternack.ucdavis.edu/files/5313/7692/9028/EDRreport_20121215_FINAL.pdf

Brown, R.A., Pasternack, G.B., 2014. Hydrologic and topographic variability modulate channel change in mountain rivers. Journal of Hydrology, 510(Supplement C), 551-564. https://doi.org/10.1016/j.jhydrol.2013.12.048

Buffington, J.M., Lisle, T.E., Woodsmith, R.D., Hilton, S., 2002. Controls on the size and occurrence of pools in coarse-grained forest rivers. River Res. Applic., 18: 507-531. doi:10.1002/rra.693

Byrd, T.C., Furbish, D.J., Warburton, J., 2000. Estimating depth-averaged velocities in rough - channels. Earth Surf. Process. Landforms, 25: 167-173. doi:10.1002/(SICI)1096-9837(200002)25:2<167::AID-ESP66>3.0.CO;2-G

Canovaro, F., Paris, E., Solari, L., 2007. Effects of macro-scale bed roughness geometry on flow resistance. Water Resources Research, 43(10). doi:10.1029/2006wr005727

Chen, Q., Baldocchi, D., Gong, P., Kelly, M., 2006. Isolating individual trees in a savanna woodland using small footprint lidar data. Photogrammetric Engineering and Remote Sensing, 72, 923-932. https://doi.org/10.14358/PERS.72.8.923

Church, M., Hassan, M.A., Wolcott, J.F., 1998. Stabilizing self-organized structures in gravel-bed stream channels: Field and experimental observations. Water Resources Research, 34(11), 3169-3179. doi:10.1029/98wr00484

Church, M., Zimmermann, A., 2007. Form and stability of step-pool channels: Research progress. Water Resources Research, 43(3). doi:10.1029/2006WR005037

Cienciala, P., Hassan, M.A., 2013. Linking spatial patterns of bed surface texture, bed mobility, and channel hydraulics in a mountain stream to potential spawning substrate for small resident trout. Geomorphology, 197(Supplement C), 96-107. https://doi.org/10.1016/j.geomorph.2013.04.041

Culvenor, D. S., 2002. TIDA: an algorithm for the delineation of tree crowns in high spatial resolution remotely sensed imagery. Computers and Geosciences, 28(1), 33-44. https://doi.org/10.1016/S0098-3004(00)00110-2

Dalponte, M., Frizzera, L., Gianelle, D., 2019. Individual tree crown delineation and tree species classification with hyperspectral and LiDAR data. PeerJ, 6:e6227. doi:10.7717/peerj.6227.

Dralle, K., Rudemo, M., 1996. Stem number estimation by kernel smoothing of aerial photos. Canadian Journal of Forest Research, 26(7), 1228-1236. doi:10.1139/x26-137

Evans, J.S., 2020. spatialEco. R package version 1.3-1, https://github.com/jeffreyevans/spatialEco.

Fang, H.W., Liu, Y., Stoesser, T., 2017. Influence of Boulder Concentration on Turbulence and Sediment Transport in Open-Channel Flow Over Submerged Boulders. Journal of Geophysical Research: Earth Surface, 122(12), 2392-2410. doi:10.1002/2017jf004221

Faustini, J.M., Jones, J.A., 2003. Influence of large woody debris on channel morphology and dynamics in steep, boulder-rich mountain streams, western Cascades, Oregon. Geomorphology, 51(1), 187-205. https://doi.org/10.1016/S0169-555X(02)00336-7

Ferguson, R.I., Sharma, B.P., Hardy, R.J., Hodge, R.A., Warburton, J., 2017. Flow resistance and hydraulic geometry in contrasting reaches of a bedrock channel. Water Resources Research, 53(3), 2278-2293. doi:10.1002/2016WR020233.

Ferro, V., 1999. Friction Factor for Gravel-Bed Channel with High Boulder Concentration. Journal of Hydraulic Engineering, 125(7), 771-778. doi:10.1061/(ASCE)0733-9429(1999)125:7(771)

Finnegan, N.J., Broudy, K.N., Nereson, A.L., Roering, J.J., Handwerger, A.L., Bennett, G., 2019. River channel width controls blocking by slow-moving landslides in California's Franciscan mélange. Earth Surf. Dynam., 7(3), 879-894. doi:10.5194/esurf-7-879-2019

Ghilardi, T., Franca, M.J., Schleiss, A.J., 2014. Bed load fluctuations in a steep channel. Water Resources Research, 50(8), 6557-6576. doi:10.1002/2013wr014449

Gippel, C.J., O'neill, I.C., Finlayson, B.L., Schnatz, I., 1996. Hydraulic guidelins for the re-inroduction and management of large woody debris in lowland rivers. Regulated Rivers: Research and Management, 12(2-3), 223-236. doi:10.1002/(sici)1099-1646(199603)12:2/3<223::aid-rrr391>3.0.co;2-#

Glade, R.C., Shobe, C.M., Anderson, R.S., Tucker, G.E., 2019. Canyon shape and erosion dynamics governed by channel-hillslope feedbacks. Geology, 47(7), 650-654. doi:10.1130/g46219.1

Gomez, B., 1993. Roughness of stable, armored gravel beds. Water Resources Research, 29(11), 3631-3642. doi:10.1029/93wr01490

Grant, G.E., Swanson, F.J., 1995. Morphology and Processes of Valley Floors in Mountain Streams, Western Cascades, Oregon, in: Costa, E., Miller, A.J., Potter, K.W., Wilcock, P.R. (Eds.), Natural and Anthropogenic Influences in Fluvial Geomorphology, Volume 89, American Geophysical Union, pp. 83–101. https://doi.org/10.1029/GM089p0083

Grant, G.E., Swanson, F.J., Wolman, M.G., 1990. Pattern and origin of stepped-bed morphology in high-gradient streams, Western Cascades, Oregon. GSA Bulletin, 102(3), 340-352. doi:10.1130/0016-7606(1990)102<0340:PAOOSB>2.3.CO;2

Groom, J., Friedrich, H., 2019. Spatial structure of near-bed flow properties at the grain scale. Geomorphology, 327, 14-27.https://doi.org/10.1016/j.geomorph.2018.10.013

Hardy, R.J., Best, J.L., Lane, S.N., Carbonneau, P.E., 2009. Coherent flow structures in a depth-limited flow over a gravel surface: The role of near-bed turbulence and influence of Reynolds number. Journal of Geophysical Research: Earth Surface, 114(F1). doi:10.1029/2007jf000970

Hassan, M.A., Bird, S., Reid, D., Ferrer-Boix, C., Hogan, D., Brardinoni, F., Chartrand, S., 2019. Variable hillslope-channel coupling and channel characteristics of forested mountain streams in glaciated landscapes. Earth Surface Processes and Landforms, 44(3), 736-751. doi:10.1002/esp.4527

Hassan, M.A., Reid, I., 1990. The influence of microform bed roughness elements on flow and sediment transport in gravel bed rivers. Earth Surface Processes and Landforms, 15(8), 739-750. doi:10.1002/esp.3290150807

Isenburg, M., 2016. LAStools - efficient LiDAR processing software (version 160730, unlicensed). http://rapidlasso.com/LAStools

Jakubowski, M.K., Li, W., Guo, Q., Kelly, M., 2013. Delineating Individual Trees from Lidar Data: A Comparison of Vector- and Raster-based Segmentation Approaches. Remote Sens. 4163-4186. https://doi.org/10.3390/rs5094163

Johnson, J. P. L., Whipple, K. X., Sklar, L. S., Hanks, T. C., 2009. Transport slopes, sediment cover, and bedrock channel incision in the Henry Mountains, Utah. Journal of Geophysical Research: Earth Surface, 114(F2). doi:10.1029/2007jf000862

Kirchner, J.W., Dietrich, W.E., Iseya, F., Ikeda, H., 1990. The variability of critical shear stress, friction angle, and grain protrusion in water-worked sediments. Sedimentology, 37(4), 647-672. doi:10.1111/j.1365-3091.1990.tb00627.x

Koch, B., Heyder, U., Weinacker, H., 2006. Detection of individual tree crowns in airborne lidar data. Photogramm. Eng. Remote Sens, 72, 357–363. https://doi.org/10.14358/PERS.72.4.357

Koukoulas, S., Blackburn, G.A., 2005. Mapping individual tree location, height and species in broadleaved deciduous forest using airborne LIDAR and multi-spectral remotely sensed data. International Journal of Remote Sensing, 26(3), 431-455. doi:10.1080/0143116042000298289

Kwak, D.A., Lee, W.K., Lee, J.H., Biging, G.S., Gong, P., 2007. Detection of individual trees and estimation of tree height using LiDAR data. Journal of Forest Research, 12(6), 425-434. doi:10.1007/s10310-007-0041-9

L'Hommedieu, W., Tullos, D., Jones, J., 2020. Effects of an engineered log jam on spatial variability of the flow field across submergence depths. River Res Applic, 36: 383– 397. https://doi.org/10.1002/rra.3555

Labatut, V., Cherifi, H., 2011. Accuracy Measures for the Comparison of Classifiers. Paper presented at the The 5th International Conference on Information Technology, amman, Jordan. https://doi.org/10.48550/arXiv.1207.3790

Lacey, R.W.J., Roy, A.G., 2008. The spatial characterization of turbulence around large roughness elements in a gravel-bed river. Geomorphology, 102(3), 542-553. https://doi.org/10.1016/j.geomorph.2008.05.045

Lai, Y. G., 2008. SRH-2D version 2: Theory and User's Manual Sedimentation and River Hydraulics – Two-Dimensional River Flow Modeling. U.S. Department of the Interior, Bureau of Reclamation, Technical Service Center, Sedimentation and River Hydraulics Group, Colorado. https://www.usbr.gov/tsc/techreferences/computer%20software/models/srh2d/index.html

Lamarre, H., Roy, A.G., 2005. Reach scale variability of turbulent flow characteristics in a gravel-bed river. Geomorphology, 68(1), 95-113. https://doi.org/10.1016/j.geomorph.2004.09.033

Landcaster, S.T., Hayes, S.K., Grant, G.E., 2001. Modeling Sediment and Wood Storage and Dynamics in Small Mountainous Watersheds, in: Dorava, J.M, Montgomery, D.R. Palcsak, B.B, Fitzpatrick, F.A. (Eds), Geomorphic Processes and Riverine Habitat, American Geophysical Union, pp. 85-102.

Laronne, J.B., Garcia, C., Reid, I., 2001. Mobility of patch sediment in gravel-bed streasm: Patch character and its implications for bedload, in: Mosley, M.P. (Ed), Gravel Bed Rivers V, New Zealand Hydrological Society, Wellington, NZ, pp. 249–289.

Leckie, D., Gougeon, F., Hill, D., Quinn, R., Armstrong, L., Shreenan, R., 2003. Combined high-density lidar and multispectral imagery for individual tree crown analysis. Canadian Journal of Remote Sensing, 29(5), 633-649. doi:10.5589/m03-024

Legleiter, C.J., Roberts, D.A., Marcus, W.A., Fonstad, M.A., 2004. Passive optical remote sensing of river channel morphology and in-stream habitat; physical basis and feasibility.

Remote Sensing of Environment, 93(4), 493-510. http://dx.doi.org/10.1016/j.rse.2004.07.019

Lisle, T.E., 1986. Stabilization of a gravel channel by large streamside obstructions and bedrock bends, Jacoby Creek, northwestern California. GSA Bulletin, 97(8), 999-1011. doi:10.1130/0016-7606(1986)97<999:soagcb>2.0.co;2

Lisle, T.E., Nelson, J.M., Pitlick, J., Madej, M.A., Barkett, B.L., 2000. Variability of bed mobility in natural, gravel-bed channels and adjustments to sediment load at local and reach scales. Water Resources Research, 36(12), 3743-3755. doi:10.1029/2000wr900238

MacKenzie, L.G., Eaton, B.C., 2017. Large grains matter: contrasting bed stability and morphodynamics during two nearly identical experiments. Earth Surf. Process. Landforms, 42: 1287– 1295. doi:10.1002/esp.4122.

MacWilliams, M.L., Wheaton, J.M., Pasternack, G.B., Street, R.L., Kitanidis, P.K., 2006. Flow convergence routing hypothesis for pool-riffle maintenance in alluvial rivers. Water Resour. Res., 42, W10427. doi:10.1029/2005WR004391

Madej, M.A., 2001. Development of channel organization and roughness following sediment pulses in single-thread, gravel bed rivers. Water Resources Research, 37(8), 2259-2272. doi:10.1029/2001wr000229

McKean, J., Tonina, D., Bohn, C., Wright, C.W., 2014. Effects of bathymetric lidar errors on flow properties predicted with a multi-dimensional hydraulic model. Journal of Geophysical Research-Earth Surface, 119(3), 644-664. doi:10.1002/2013jf002897

Monsalve, A., Yager, E.M., Schmeeckle, M.W., 2017. Effects of bed forms and large protruding grains on near-bed flow hydraulics in low relative submergence conditions. Journal of Geophysical Research: Earth Surface, 122, 1845– 1866. https://doi.org/10.1002/2016JF004152

Moriasi, D.N., Arnold, J.G., Van Liew, M.W., Bingner, R.L., Harmel, R.D., Veith, T.L., 2007. Model Evaluation Guidelines for Systematic Quantification of Accuracy in Watershed Simulations. Transactions of the ASABE, 50(3), 885. https://doi.org/10.13031/2013.23153

Morris, H., 1959. Design methods for flow in rough channels. Proc. ASCE, Journal of Hydraulics Division, 85(HY7), 43-62. https://doi.org/10.1061/JYCEAJ.0000324

Morsdorf, F., Meier, E., Kötz, B., Itten, K.I., Dobbertin, M., Allgöwer, B., 2004. LIDAR-based geometric reconstruction of boreal type forest stands at single tree level for forest and wildland fire management. Remote Sensing of Environment, 92(3), 353-362. https://doi.org/10.1016/j.rse.2004.05.013

Nelson, J.M., Shimizu, Y., Abe, T., Asahi, K., Gamou, M., Inoue, T., Iwasaki, T., Kakinuma, T., Kawamura, S., Kimura, I., Kyuka, T., McDonald, R.R., Nabi, M., Nakatsugawa, M., Simões, F.R., Takebayashi, H., Watanabe, Y., 2016. The international river interface cooperative: Public domain flow and morphodynamics software for education and applications. Advances in Water Resources 93: 62–74. https://doi.org/10.1016/j.advwatres.2015.09.017

Nitsche, M., Rickenmann, D., Turowski, J.M., Badoux, A., Kirchner, J.W., 2011. Evaluation of bedload transport predictions using flow resistance equations to account for macro-roughness in steep mountain streams. Water Resources Research, 47(8). doi:10.1029/2011wr010645

Nowell, A.R.M., Church, M., 1979. Turbulent flow in a depth-limited boundary layer. Journal of Geophysical Research: Oceans, 84(C8), 4816-4824. doi:10.1029/JC084iC08p04816

Otsu, N., 1979. A Threshold Selection Method from Gray-Level Histograms, in: IEEE Transactions on Systems, Man, and Cybernetics, vol. 9(1), pp. 62-66. doi:10.1109/TSMC.1979.4310076.

Pagliara, S., Das, R., Carnacina, I., 2008. Flow resistance in large-scale roughness condition. Canadian Journal of Civil Engineering, 35(11), 1285-1293. doi:10.1139/L08-068

Paola, C., Seal, R., 1995. Grain Size Patchiness as a Cause of Selective Deposition and Downstream Fining, Water Resour. Res., 31(5), 1395-1407. doi:10.1029/94WR02975

Paola, C., Heller, P., Angevine, C., 1992. The large-scale dynamics of grain-size variation in alluvial basins, 1: Theory, Basin Res., 4, 73–90. https://doi.org/10.1111/j.1365-2117.1992.tb00145.x

Papanicolaou, A.N., Tsakiris, A.G., 2017. Boulder Effects on Turbulence and Bedload Transport in: Tsutumi, D., Laronne, J.B., (Eds.), Gravel-Bed Rivers: Processes and Disasters, Wiley, Chichester, pp. 33–72.

Pasternack, G.B., 2008. Spawning Habitat Rehabilitation: Advances in Analysis Tools, in: Sear, D. A., DeVries, P. (Eds.), Salmonid Spawning Habitat in Rivers: Physical Controls, Biological Responses, and Approaches to Remediation (Vol. 65). Amer. Fisheries Soc., Bethesda, pp. 321-348.

Pasternack, G.B., 2011. 2D Modeling and Ecohydraulic Analysis. Seatle, WA: Createspace.

Pasternack, G.B., Ellis, C R., Leier, K.A., Vallé, B.L., Marr, J.D., 2006. Convergent hydraulics at horseshoe steps in bedrock rivers. Geomorphology, 82(1), 126-145. https://doi.org/10.1016/j.geomorph.2005.08.022

Pasternack, G.B., MacVicar, B.J., 2013. Gold-standard performance for 2D hydrodynamic modeling. Abstract EP51B-0708. Paper presented at the 2013 Fall Meeting, AGU, San Francisco, Calif., 9-13 Dec.

Pasternack, G.B., Senter, A.E., 2011. 21st Century instream flow assessment framework for mountain streams. California Energy Commission, PIER. CEC-500-2013-059. https://www.energy.ca.gov/2013publications/CEC-500-2013-059/CEC-500-2013-059.pdf

Piedra, M.M., Haynes, H., Hoey, T.B., 2012. The spatial distribution of coarse surface grains and the stability of gravel river beds. Sedimentology, 59(3), 1014-1029. doi:10.1111/j.1365-3091.2011.01290.x

Plowright, A., Roussel, J., 2020. ForestTools: Analyzing Remotely Sensed Forest Data. R package version 0.2.1. https://CRAN.R-project.org/package=ForestTools

Popescu, S.C., Wynne, R.H., 2004. Seeing the Trees in the Forest. Photogrammetric Engineering and Remote Sensing, 70(5), 589-604. doi:10.14358/PERS.70.5.589

Reid, I. Hassan, M.A., 1992. The influence of microform bed roughness elements on flow and sediment transport in gravel bed rivers: A reply. Earth Surf. Process. Landforms, 17: 535-538. doi:10.1002/esp.3290170512

Reid, D.A., Hassan, M.A., Bird, S., Pike, R., Tschaplinski, P., 2020. Does variable channel morphology lead to dynamic salmon habitat? Earth Surf. Process. Landforms, 45, 295-311. https://doi.org/10.1002/esp.4726.

Richardson, K., Carling, P.A., 2006. The hydraulics of a straight bedrock channel: Insights from solute dispersion studies. Geomorphology, 82(1), 98-125. https://doi.org/10.1016/j.geomorph.2005.09.022

Sawyer, A.M., Pasternack, G.B., Moir, H.J., Fulton, A.A., 2010. Riffle-pool maintenance and flow convergence routing observed on a large gravel-bed river. Geomorphology, 114(3), 143-160. doi:10.1016/j.geomorph.2009.06.021

Schneider, J.M., Rickenmann, D., Turowski, J.M., Kirchner, J.W., 2015a. Self-adjustment of stream bed roughness and flow velocity in a steep mountain channel. Water Resources Research, 51(10), 7838-7859. doi:10.1002/2015wr016934

Schneider, J.M., Rickenmann, D., Turowski, J.M., Bunte, K., Kirchner, J.W., 2015b. Applicability of bed load transport models for mixed-size sediments in steep streams considering macro-roughness. Water Resources Research, 51(7), 5260-5283. doi:10.1002/2014wr016417

Sear, D.A., 1992. Impact of hydroelectric power release on sediment transport processes in pool-riffle sequences, in: Billi, P., Hey, R.D., Thorne, C.R., Tacconi, P. (Eds), Dynamics of Gravel Bed Rivers, Wiley, Chichester, pp: 629–650.

Sear, D.A., 1995. The effect of 10 years river regulation for hydropower on the morphology and sedimentology of a gravel-bed river. Regulated Rivers, 10, 247–264.

Sear, D.A., 1996. Sediment transport in riffle-pool sequences. Earth Surface Processes and Landforms, 21, 241-262. https://doi.org/10.1002/(SICI)1096-9837(199603)21:3<241::AID-ESP623>3.0.CO;2-1

Shamloo, H., Rajaratnam, N., Katopodis, C., 2001. Hydraulics of simple habitat structures. Journal of Hydraulic Research, 39(4), 351-366. doi:10.1080/00221680109499840

Shao, G., Tang, L., Liao, J., 2019. Overselling overall map accuracy misinforms about research reliability. Landscape Ecology, 34(11), 2487-2492. doi:10.1007/s10980-019-00916-6

Shobe, C.M., Tucker, G.E., Anderson, R.S., 2016. Hillslope-derived blocks retard river incision. Geophysical Research Letters, 43(10), 5070-5078. doi:10.1002/2016gl069262

Sklar, L.S., Dietrich, W.E., 2004. A mechanistic model for river incision into bedrock by saltating bed load. Water Resources Research, 40(6). doi:10.1029/2003wr002496

Strîmbu, V.F., Strîmbu, B.M., 2015. A graph-based segmentation algorithm for tree crown extraction using airborne LiDAR data. Journal of Photogrammetry and Remote Sensing, 104, 30-43. https://doi.org/10.1016/j.isprsjprs.2015.01.018

Strom, M.A., Pasternack, G.B., Burman, S.G., Dahlke, H.E., Sandoval-Solis, S., 2017. Hydraulic hazard exposure of humans swept away in a whitewater river. Natural Hazards, 88(1), 473-502. doi:10.1007/s11069-017-2875-6

Strom, M.A., Pasternack, G.B., Wyrick, J.R., 2016. Reenvisioning velocity reversal as a diversity of hydraulic patch behaviours. Hydrological Processes, 30(13), 2348-2365. doi:10.1002/hyp.10797

Sullivan, A.A., McGaughey, R.J., Andersen, H.E., Schiess, P., 2009. Object-Oriented Classification of Forest Structure from Light Detection and Ranging Data for Stand Mapping. Western Journal of Applied Forestry, 24(4), 198-204. doi:10.1093/wjaf/24.4.198

Sutfin, N.A., Wohl, E., 2019. Elevational differences in hydrogeomorphic disturbance regime influence sediment residence times within mountain river corridors. Nature Communications, 10(1), 2221. doi:10.1038/s41467-019-09864-w

Tan, L., Curran, J.C., 2012. Comparison of Turbulent Flows over Clusters of Varying Density. Journal of Hydraulic Engineering, 138(12), 1031-1044. doi:10.1061/(ASCE)HY.1943-7900.0000635

Thompson, C.J., Fryirs, K., Croke, J., 2016. The Disconnected Sediment Conveyor Belt: Patterns of Longitudinal and Lateral Erosion and Deposition During a Catastrophic Flood in the Lockyer Valley, South East Queensland, Australia. River Research and Applications, 32(4), 540-551. doi:10.1002/rra.2897

Thompson, D.M., 2001. Random controls on semi-rhythmic spacing of pools and riffles in constriction-dominated rivers. Earth Surface Processes and Landforms, 26(11), 1195-1212. doi:10.1002/esp.265

Thompson, D.M., 2008. The influence of lee sediment behind large bed elements on bedload transport rates in supply-limited channels. Geomorphology, 99(1), 420-432. https://doi.org/10.1016/j.geomorph.2007.12.004

Turowski, J.M., Lague, D., Hovius, N., 2007. Cover effect in bedrock abrasion: A new derivation and its implications for the modeling of bedrock channel morphology. J. Geophys. Res., 112, F04006. doi:10.1029/2006JF000697.

Turowski, J.M., Hovius, N., Meng-Long, H., Lague, D., Men-Chiang, C., 2008. Distribution of erosion across bedrock channels. Earth Surf. Process. Landforms, 33, 353-363. doi:10.1002/esp.1559

Weichert, R., 2006. Bed Morphology and Stability of Steep Open Channels. In Mitteilung 192, Zürich: Versuchsanstalt fürWasserbau, Hydrologie und Glaziologie (VAW), ETH. https://doi.org/10.3929/ethz-a-005135522

Wentworth, C., 1922. A Scale of Grade and Class Terms for Clastic Sediments. The Journal of Geology, 30(5), 377-392. http://www.jstor.org/stable/30063207

Wiener, J., Pasternack, G.B., 2016. 2014 Topographic Mapping Report- Yuba River from New Bullards Bar to Colgate Powerhouse. Prepared for Yuba County Water Agency. University of California, Davis, CA. http://pasternack.ucdavis.edu/index.php?cID=429

Williams, R.D., Reid, H.E., Brierley, G.J., 2019. Stuck at the Bar: Larger-Than-Average Grain Lag Deposits and the Spectrum of Particle Mobility. Journal of Geophysical Research: Earth Surface, 124(12), 2751-2756. doi:10.1029/2019jf005137

Wittenberg, L., Newson, M.D., 2005. Particle clusters in gravel-bed rivers: an experimental morphological approach to bed material transport and stability concepts. Earth Surface Processes and Landforms, 30(11), 1351-1368. doi:10.1002/esp.1184

Wyrick, J.R., Pasternack, G.B., 2012. Specific sampling protocols for delineating morphological units and mesohabitats: methodology for classifying channel landforms. Prepared for the Lower Yuba River Accord, River Management Team. June 2011. 30p.

Yager, E.M., Dietrich, W.E., Kirchner, J.W., McArdell, B.W., 2012. Prediction of sediment transport in step-pool channels. Water Resources Research, 48(1). doi:10.1029/2011wr010829

Yager, E.M., Kirchner, J.W., Dietrich, W.E., 2007. Calculating bed load transport in steep boulder bed channels. Water Resources Research, 43(7). doi:10.1029/2006wr005432

Yang, K., Cao, S., Liu, X., 2007. Flow resistance and its prediction methods in compound channels. Acta Mechanica Sinica, 23(1), 23-31. doi:10.1007/s10409-006-0043-4

Yochum, S.E., Comiti, F., Wohl, E., David, G.C.L., Mao, L., 2014. Photographic guidance for selecting flow resistance coefficients in high-gradient channels. https://www.fs.usda.gov/treesearch/pubs/46250

Zhang, K., Whitman, D., 2005. Comparison of Three Algorithms for Filtering Airborne Lidar Data. Photogrammetric Engineering and Remote Sensing, 71(3), 313-324. doi:10.14358/PERS.71.3.313

Zimmermann, A., Church, M., 2001. Channel morphology, gradient profiles and bed stresses during flood in a step–pool channel. Geomorphology, 40(3), 311-327. https://doi.org/10.1016/S0169-555X(01)00057-5